Journal of Materials Chemistry A

ROYAL SOCIETY OF CHEMISTRY

REVIEW

View Article Online
View Journal | View Issue

Cite this: J. Mater. Chem. A, 2023, 11, 12559

A comparative overview of MXenes and metal oxides as cocatalysts in clean energy production through photocatalysis

Mahesh M. Nair,[a] Alexandra C. Iacoban,[ab] Florentina Neaţu, [a] Mihaela Florea *[a] and Ştefan Neaţu*[a]

Photocatalytic conversion of H_2O, CO_2 and N_2 represents one promising approach to harvest and store solar energy, for which efficient visible light responsive semiconductors are inevitable. Often, the presence of a small amount of an additional component called a "cocatalyst", is required to synergistically enhance the performance of the photocatalyst. Tremendous efforts were made in the past to identify inexpensive materials to be used as cocatalysts, for which metal oxides (MOs) are one of the traditional choices. Among alternative categories of materials investigated, the recently discovered MXenes display enormous potential owing to their unique 2D layered structure, tuneable composition, abundant surface functionalities and superior electronic conductivity. Specifically, MOs and MXenes encompass a variety of distinct as well as analogous characteristics that allows them to be tailored to different extents. Unfortunately, a comprehensive overview covering the synthetic, structural and photocatalytic aspects of MOs and MXenes is not available as of now. Herein, we intend to summarize the progress achieved so far in these two families of materials to be used as cocatalysts for the photoconversion of H_2O, CO_2 and N_2. Followed by a general introduction, we briefly outline the fundamental principles and the role of cocatalysts in photocatalytic reactions. A discussion regarding the use of MOs and MXenes as cocatalysts for the conversion of H_2O, CO_2 and N_2 is then provided in separate sections. Critical assessment regarding structure and morphology control, surface properties and stability concerns can not only help to recognize the challenges that limit further advancement, but can also highlight the future research directions of these materials for the effective transformation of H_2O, CO_2 and N_2.

Received 17th November 2022
Accepted 12th January 2023

DOI: 10.1039/d2ta08983a

rsc.li/materials-a

10th anniversary statement

J. Mater. Chem. A is dedicated to publish original contributions to research at the interface of materials science and chemistry. To celebrate the 10th anniversary of *J. Mater. Chem. A*, we devoted a special review discussing, what else than materials, new developed materials such as MXenes and old, but still unfashionable materials such as metal oxides. As you will be able to see while reading this review, the use of the two types of materials as cocatalysts leads to obtaining truly extraordinary hybrid composites with applicability in various photocatalytic reactions. Speaking about photocatalysis in general, and in particular about finding new materials with direct applications in the photocatalysis field, *J. Mater. Chem. A* was, is and it will be a landm ark for both specialized and non-specialized readers passionate about novelty. Therefore, what binds us to the *J. Mater. Chem. A* is this very passion for novelty in the field of materials chemistry. Now reaching its 10th anniversary, we wish *J. Mater. Chem. A* to continue to surround us with the joy of reading outstanding papers that arouse our attention and appetite for new discoveries. Happy Anniversary, *J. Mater. Chem. A*!

1. Introduction

Being the major contributor to global warming, the emission of large quantities of CO_2 by the burning of fossil fuels demands immediate attention. The harmful effects arising from the increasing concentration of atmospheric CO_2, coupled with the progressive depletion of the fossil fuel reserves drives the quest for alternative energy sources. Therefore, energy harvesting in a clean and sustainable manner remains the most crucial challenge the world is currently facing. Solar energy is promising in this regard and represents a readily available and exploitable substitute to fossil fuels.[1–3] Solar energy needs to be captured and converted into useful forms, especially considering the intermittency (day/night, seasons, *etc.*). One such existing and established technology is electricity generation using solar cells.[4,5] Solar electricity needs to be converted into chemical fuels, since these are the primary energy feedstock for

[a]National Institute of Materials Physics, 405A Atomistilor Street, 077125 Magurele, Romania. E-mail: mihaela.florea@infim.ro; stefan.neatu@infim.ro
[b]Interdisciplinary School of Doctoral Studies, University of Bucharest, Mihai Kogalniceanu Street 36-46, 050067 Bucharest, Romania

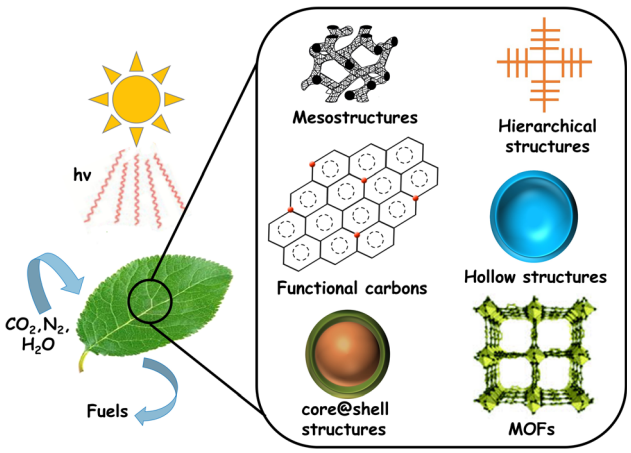

Fig. 1 Schematic representation of solar fuel production from CO_2, H_2O and N_2, along with the photocatalytic structural variants commonly studied.

industrial and transportation sectors. However, such transitions are difficult, demand additional costs and are time consuming. Moreover, there are technological challenges involving storage and transportation in a cost-effective and convenient manner. Therefore, direct production of fuels and chemicals using solar energy is considered a more attractive option.

Inspired by the natural process of photosynthesis, efforts were made in the recent past to create solar fuels using semiconductor photocatalysts, called 'artificial leaves', as shown in Fig. 1. In this case, photon energy from the sun is used to generate electron–hole pairs to drive redox reactions.[6–10]

Most of the initial studies focused on the production of H_2 by splitting H_2O using photocatalysts.[11,12] Apart from being an energy carrier itself, H_2 can be used to generate hydrocarbons by photoreduction of CO_2, thereby creating a significant environmental impact by converting a greenhouse gas into a useful commodity or for N_2 photofixation toward a better solar-to-chemical energy conversion.

In short, the production and development of a technology that utilizes sunlight to efficiently convert H_2O and CO_2 into H_2, hydrocarbons, or syngas (CO + H_2) can revolutionize the concept of fuel production. Here, functional materials that encompass desired photocatalytic properties such as enhanced solar light absorption, high charge separation, appropriate band gaps, *etc.*, form a major requirement.[13–16] Compositional optimization of these materials was the earliest and most straightforward approach followed to achieve this. A variety of oxides, oxynitrides, metal organic frameworks (MOFs), carbonaceous materials, *etc.*, were studied to identify the best candidates for producing solar fuels from H_2O and CO_2.[17–22] Unfortunately, materials that satisfy all the practical requirements have not yet been found. On the bright side, several of these studies confirmed the dependence of photocatalytic properties on the structural features and morphology of the materials.[13,15,17]

One proven strategy to enhance the photoactivity of a semiconductor is to integrate a small amount of a secondary component. This secondary component called a "cocatalyst" facilitates the separation of charge carriers by forming an interface with the photocatalyst. Also, it can serve as the active site for the surface reaction to take place.[23–26] Preliminary studies on the use of noble metals (*i.e.*, Pt, Pd, Ag, and Au) as cocatalysts were promising, however, with limited commercial applicability owing to their high costs.[27–29] Numerous non-noble metal alternatives were therefore investigated as cost-effective photocatalysts. So far, transition metal-based materials including oxides, hydroxides, sulfides, *etc.*, have been widely explored.[30–34] More recently, the introduction of 2D transition metal carbides, called MXenes, as cocatalysts was found to significantly promote photocatalytic H_2O splitting and CO_2 reduction.[35–40]

In general, performance optimization primarily relies on structural and compositional aspects of the materials employed. Metal oxides (MOs) can accommodate a large number of cationic components in varying amounts in their structure, thereby allowing the long-range tailoring of their physicochemical properties. In conjugation, the noteworthy progress achieved so far in inorganic synthesis makes it possible to prepare these materials in a variety of nanostructures and morphologies. Similarly, MXenes, regardless of their short period of evolution, exhibited significant potential to host a number of metallic components in varying proportions in their structure.[41–44] Several recent reports also claim the possibility of preparing morphological variants of these materials.[38] An additional advantage exclusive to MXenes is the

*Integrated in the Catalytic Material and Catalysis group, the research team is part of the National Institute of Materials Physics, Romania (NIMP) (**infim.ro**). Back row, left to right: Dr Ştefan Neaţu (senior researcher), Dr Mahesh Nair (Postdoc), and Dr Florentina Neaţu (senior researcher) and lower row, left to right: Dr Mihaela Florea (senior researcher) and Alexandra Iacoban (PhD student). The design, characterisation, and investigation of the physical properties of novel materials are the main goals of the NIMP team's research. Their primary areas of applications implies heterogeneous catalysis, energy conversion, electrochemistry, fuel cells, and materials surface science.*

presence of inherent surface functionalities that can be useful for catalytic applications.

Several reviews exist regarding the synthesis and applications of MXenes, including photocatalysis.[35–45] Moreover, theoretical results and insights on how MXenes and/or MOs contribute to photocatalysis as cocatalysts exist already in the literature.[46–52] The present review summarizes the major milestones achieved regarding the use of MOs and MXenes as cocatalysts for hydrogen production through the water splitting reaction and photocatalytic CO_2 and N_2 reduction reactions. To maximize the synergistic interactions, it is crucial to maintain optimum contact between the semiconductor and cocatalyst, which depends primarily on the synthetic procedures and nanoscale structural arrangement. Therefore, we separately discuss the general advantages of nanostructures in photocatalysis, the progress so far on the development of synthetic approaches and the resultant structure evolution for MXenes and MOs. Furthermore, applications of these two categories of materials for photocatalytic H_2O, CO_2 and N_2 conversion will be summarized. Comparisons will be made highlighting the advantages and disadvantages, where appropriate. In addition, challenges and future directions for MOs and MXenes regarding the photocatalytic conversion of H_2O, CO_2 and N_2 will be provided from the perspective of the authors.

2. Fundamentals of photocatalysis and the relevance of nanostructures

In general, photocatalysis involves light absorption, charge separation (electrons and holes) and surface reactions initiated by these photogenerated charge carriers (see Fig. 2). Photon energy corresponding to the band gap of the semiconductor will be absorbed resulting in the generation of electrons (e^-) in the conduction band and holes (h^+) in the valence band. The reactants will be adsorbed at the active sites on the surface of the photocatalyst. The photogenerated charge carriers (e^- and h^+) can get trapped, recombine, or migrate towards the surface, to drive the desired transformation of the adsorbed reactant species. The products thus formed will then be desorbed from the surface.[53,54] During water splitting, the photogenerated holes will interact with H_2O, producing O_2 and H^+. The H^+ ions will consume the e^- residing at the conduction band forming H_2.

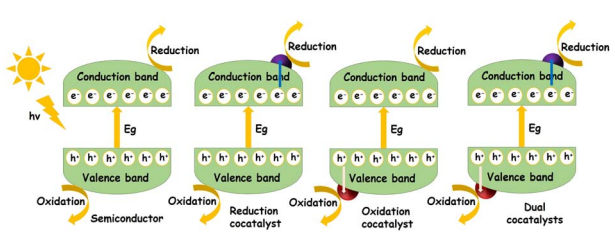

Fig. 2 Fundamental principles in photocatalysis including light absorption, charge separation, and surface reactions, along with the influence of cocatalysts.

On the other hand, photoreduction of CO_2 is more complex involving multiple electrons that can end up in a series of low molecular weight organic products. Therefore, in this later case, reaction selectivity is also a major concern.[55] The N_2 photofixation process involves the use of holes generated by light irradiation to oxidize the H_2O (as in the case of water splitting), while the e^- are used to reduce the N_2 to ammonia.[56] The photocatalytic water splitting, CO_2 reduction and N_2 photofixation reactions are shown in eqn (1)–(2), (3)–(7) and (8), respectively. It is to be noted here that apart from electrons and holes, other reactive intermediates are formed during photocatalysis. These reactive oxygen species are particularly useful for the photodegradation of organic pollutants and hence will not be discussed here.[57]

$$H_2O + 2h^+ \rightarrow \tfrac{1}{2}O_2 + 2H^+ \quad (1)$$

$$2H^+ + 2e^- \rightarrow H_2 \quad (2)$$

$$CO_2 + 2H^+ + 2e^- \rightarrow HCOOH \quad (3)$$

$$CO_2 + 2H^+ + 2e^- \rightarrow CO + H_2O \quad (4)$$

$$CO_2 + 4H^+ + 4e^- \rightarrow HCHO + H_2O \quad (5)$$

$$CO_2 + 6H^+ + 6e^- \rightarrow CH_3OH + H_2O \quad (6)$$

$$CO_2 + 8H^+ + 8e^- \rightarrow CH_4 + 2H_2O \quad (7)$$

$$N_2 + 6H^+ + 6e^- \rightarrow 2NH_3 \quad (8)$$

Thermodynamically, a reduction reaction will take place if the conduction band is located at a more negative potential and an oxidation reaction requires a more positive valence band than the oxidation potential. Unfortunately, this requirement is often satisfied by materials with much wider band gaps, prohibiting their functioning in the visible region, where the major portion of solar energy is distributed. In addition, prolonged charge separation is strongly desired to minimize the electron–hole recombination that can occur during their migration towards the surface.[53,54]

Systematic tailoring of the structure and morphology at the nanoscale can have a profound effect on the overall photocatalytic properties of materials.[13,15,58,59] Performance enhancement in nanostructures can be attributed to an increased surface area, reduced diffusion barriers and shortened charge transport pathways. Nanomaterials in general exhibit enhanced values of specific surface area. Since only surface atoms participate in photocatalytic reactions, a high surface area implies that more atoms are available as adsorption sites for the reactants. A high surface-to-volume ratio results in an abundant and uniform distribution of accessible active sites and often promotes charge transfer ac ross interfaces. Several studies considered nanostructuring as a way to improve the light harvesting efficiency of photocatalysts.[13,15,60,61] A few possible effects of nanostructures on photocatalysis are schematically shown in Fig. 3.

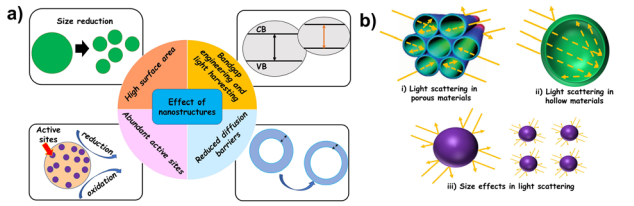

Fig. 3 (a) General influence of nanostructures in photocatalysis and (b) light scattering effects under confinement.

Nanostructures will provide an increased number of transport paths resulting in a prolonged interaction time of the photocatalyst with incoming light. This results in an enhanced surface distribution, thereby improving the light absorption effectiveness. For instance, light scattering effects observed in some nanostructures can influence the light harvesting efficiency of photocatalysts. In a conventional bulk material, surface reflection is predominant whereas in nanostructures, the incident light is scattered resulting in secondary absorptions, leading to enhanced light harvesting.[61–63]

The effect of secondary scattering can be more pronounced where a high degree of confined spaces is available (*e.g.*, nanoporous materials). Thin films or hollow nanostructures with thin walls could promote facile diffusion of charge carriers towards the surface adsorbed reactant species.[64] Nanoporous materials generally have particle size distribution in the micrometer regime and can prevent stability issues related to agglomeration prevalent in conventional nanosized particles. Apart from the enhancement of light absorption and transport kinetics, the quantum confinement effects inherent in nanostructures can often facilitate appropriate band gap engineering. Quantum size effects can modify the position of the valence and conduction bands in the photocatalyst. Also, confined nanoparticles can result in the generation of multiple e^-/h^+ pairs (excitons). Overall, the improved photocatalytic performance of nanostructured materials stems from a combination of their structural features, specific surface area and presence of accessible active sites.[65] In reality, photocatalytic conversion of H_2O, CO_2 and N_2 depends on the physicochemical and optical properties of the photocatalyst. Even though nanostructure optimization can improve some of these properties, it can be unfavourable to the others. Therefore, a rational approach for the design of nanostructured photocatalysts must take the disadvantages also into consideration. For instance, an increased surface energy inherent in nanomaterials can influence its thermodynamic stability. Also, high interfacial areas and short diffusion lengths in nanoscale materials can promote undesired and easy recombination of the charge carriers, influencing the reaction rates.

As mentioned above, the presence of a cocatalyst is necessary to improve the photocatalytic properties of semiconductors. In other words, the overall performance stems from the synergistic functioning of both these components in the form of a hybrid. Therefore, any discussion regarding the fundamental mechanism of photocatalysts cannot exclude the role of cocatalysts, improving a photocatalytic reaction by providing reaction sites and by promoting charge separation. Reduction cocatalysts are used to trap electrons whereas oxidation cocatalysts are used for trapping holes. The presence of a cocatalyst should not hinder the active sites from light absorption or accessibility of the reactants and should improve the corresponding half reaction whereas dual cocatalyst-semiconductor photocatalytic systems contribute towards the advancement of the overall redox reaction.[23–26]

3. MXenes

3.1. Short overview

The presence of a cocatalyst synergistically modifies the performance of a semiconductor photocatalyst and to maximize such interactions, it is important to maintain optimum contact. Therefore, several approaches have been developed to integrate the cocatalyst with the semiconductor. This includes the synthesis of the cocatalyst separately and then combining it with the semiconductor in a post-synthetic manner, or synthesizing the cocatalyst and the semiconductor in one pot. For instance, the synthetic procedure for MXenes is not compatible with routinely used semiconductor photocatalysts. Moreover, the thermal stability of MXenes is limited under oxidizing conditions. Therefore, post-synthetic approaches are always necessary for integrating MXenes as a cocatalyst.

3.2. Synthesis and structure evolution

Naguib *et al.*,[66] in 2011, reported a transition metal containing graphene analogue ($Ti_3C_2T_x$), called MXene, obtained by selectively extracting Al from the parent MAX phase (Ti_3AlC_2) using HF.[66] In the strategies developed so far, the synthesis of MXenes involves the selective etching of an A-layer from the MAX phase, by exploiting the differences between the metal–metal (M–A) and metal–carbon (M–X) bond strengths.[40–42,66] The use of aqueous HF as the etchant resulted in the formation of a multilayered material with abundant –F, –O and –OH surface terminations (see Fig. 4).[67] These materials are represented by the general formula $M_{n+1}X_nT_x$, where *M* denotes early transition

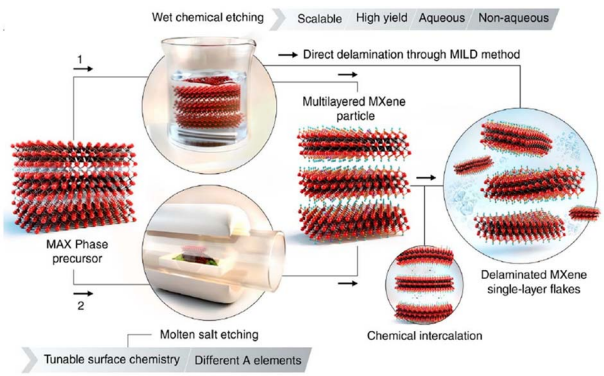

Fig. 4 Schematic representation of two etching strategies to remove the A layers from MAX phases to produce multi-layered MXenes and delaminated single layer flakes. Reproduced with permission from ref. 67, Copyright 2021 Science.

metals, X can be carbon or nitrogen, T indicates the surface functionalities such as hydroxyl groups, halides, *etc.* and n determines the number of layers, usually between 1 and 4. Recently, MXenes with $n = 5$ were discovered.[68] It is to be noted here that the etching conditions were influenced by the variations in M–Al bond strength and hence, minor disparities in etching conditions are inevitable. The presence of surface functionalities enables the post-synthetic modifications through intercalation or grafting, thereby tailoring the physicochemical properties of these materials as desired.[69,70] With regard to the safety issues in handling HF, LiF/HCl mixture, ammonium bifluoride (NH_4HF_2), *etc.* were also found to be useful as alternatives.[71,72] Other approaches such as electrochemical etching in HCl, hydrothermal treatment (HTT) in NaOH, iodine dissolved in anhydrous acetonitrile, molten salt such as $ZnCl_2$ or $CuCl_2$ at enhanced temperatures were also reported.[73–77] However, in some cases, issues such as incomplete etching and the presence of impurities, could not be avoided.[74]

In short, the composition of MXenes primarily depends on the parent MAX phase while the structure and surface properties are influenced by the etching protocols. The simplest version of MXenes or conventional MXenes incorporates an early transition metal attached to carbon.[66] Afterwards, more complex structural and compositional variants were discovered.[78–83] For this, MAX phases with more than one transition metal were used as precursors. *o*-MXenes consist of multiple transition metal components with an inner layer formed by one component and the outer layer by the other. On the other hand, non-stoichiometric *i*-MXenes display an ordered array of vacancies in the metal in-plane layer.

Tremendous progress has been achieved so far in controlling the synthesis parameters to obtain 2D MXene layers. Liquid phase exfoliation of the accordion structure resulted in the expansion of interlayer space, which weakens interlayer interactions, resulting in nanosized sheets. Usually, the concept of etching was used to remove the A layer from the precursor MAX phase.

Interestingly, Ren *et al.*[85] extended this etching concept for the synthesis of porous 2D $Ti_3C_2T_x$ open structures with large surface area.[85] Delaminated colloidal solutions were partially oxidized with O_2 dissolved in the water, in the presence of Cu^{2+} as a catalyst. Selectively removal of TiO_2 nanoparticles thus formed resulted in porous $Ti_3C_2T_x$ flakes. Stacking of 2D MXene sheets can limit their applicability and hence strategies are to be developed to hinder their aggregation.

Zhao *et al.*[84] proposed a hard templating method to derive hollow spheres and 3D architectures of MXene flakes and the corresponding images are provided in Fig. 5. Hollow spheres and 3D microporous films were made by using polymethyl methacrylate (PMMA) spheres as the template.[86] In a similar manner, Xiu *et al.*[87] used an ultrasound assisted aerosol spray drying method, to overcome the possible aggregation of MXene nanosheets.[87] These authors successfully assembled $Ti_3C_2T_x$ into hierarchical 3D architectures by evaporating aerosol droplets produced by ultrasonication, exhibiting geometry-based resistance to aggregation. It was also shown that by introducing polyvinyl pyrrolidine into the MXene colloidal

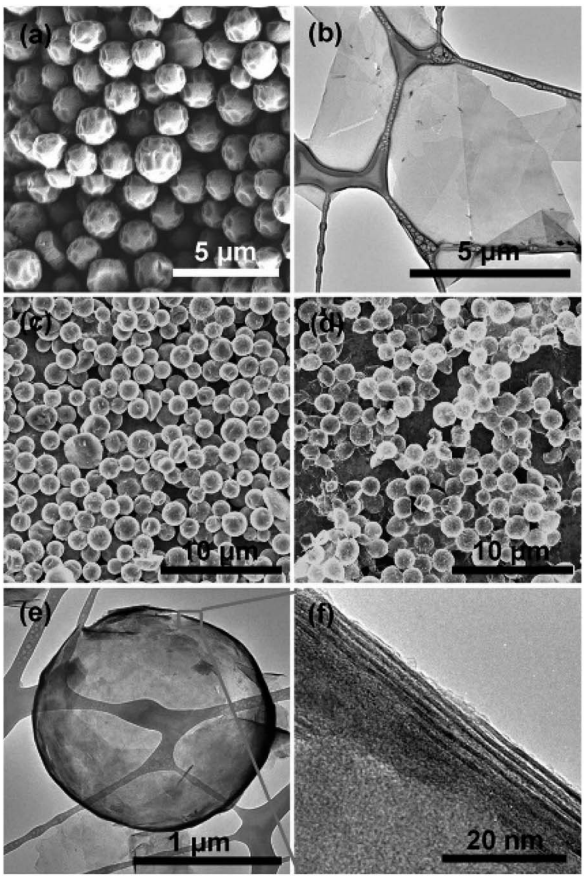

Fig. 5 (a) SEM images showing the morphology of the as-produced PMMA spheres. (b) TEM image of $Ti_3C_2T_x$ flakes. SEM image of (c) $Ti_3C_2T_x$/PMMA hybrids and (d) hollow $Ti_3C_2T_x$ spheres after removal of PMMA, showing that the spherical shape is retained after PMMA's thermal evaporation at 450 °C. TEM images showing (e) a hollow $Ti_3C_2T_x$ sphere and (f) its wall MXene layers. Reproduced with permission from ref. 84, Copyright 2017 Wiley Publications.

solution, sphere like 3D architectures can be produced. Free standing 3D network structures were developed by assembling MXenes in the presence of templates.[88–90] MXene quantum dots (QDs) were fabricated by dissociating their layered structure using HTT, an ultrasonic method, *etc.*[91–94]

For photocatalytic applications, post-synthetic procedures are almost always necessary for MXenes. Simple oxidation treatment sometimes results in partial oxidation of the metallic species in MXenes, resulting in the formation of the corresponding MXene-oxide composites.[95,96] In addition, other wet-chemical approaches including HTT, ultrasonication, *etc.* are frequently employed.[97–99]

3.3. Photocatalytic applications for water splitting

In spite of MXenes being metallic, the surface functionalities can be effectively tailored so as to directly employ them as semiconductor photocatalysts.[100] Studies utilizing deformation potential theory (DPT), density functional theory (DFT) and *ab initio* molecular dynamics (AIMD) calculations clearly predicted several MXene compositions that can be used for photocatalytic

applications.[101–104] However, experimental validation of the synthesis of such compositions and the evaluation of their photocatalytic performance are yet to be made.

3.3.1 MXenes as photocatalyst-cocatalyst precursors. Even though the direct use of MXenes as photocatalysts is not yet proven, these materials can be preferentially oxidized under controlled conditions to generate oxide particles on the surface. In this case, a cocatalyst-photocatalyst composite is found to be generated from a single MXene precursor.

For instance, by performing controlled oxidation of Nb_2CT_x using CO_2 as a mild oxidant, Su *et al.*[95] successfully synthesized Nb_2O_5/C/Nb_2C composites. The materials obtained after an oxidation time of 1 h exhibited hydrogen evolution rates 4 times higher than that of pristine Nb_2O_5, with an AQY of 0.11%. Hydrogen yield remain consistent during four consecutive cycles. The Schottky layer formed at the interface acted as an electron sink from which backward diffusion to the Nb_2O_5 photocatalyst was hindered. The presence of an amorphous carbon layer at the Nb_2O_5/C/Nb_2C interface also contributed towards the separation of photogenerated charge carriers.[95] This work confirmed that MXenes can act as precursors for photocatalysts. In another study, it was observed that carbon doped TiO_2 can be produced from $Ti_3C_2T_x$ nanosheets under HTT.[105] This material exhibited a 9.7 times higher hydrogen production rate compared to commercial TiO_2 (P25) using triethanolamine (TEA) as a hole scavenger and in the absence of a cocatalyst. The authors carried out XRD analysis of the material recovered after the reaction and the pattern confirmed the structural stability of this material. This work further confirms the role of carbon in facilitating the separation of charge carriers and the use of MXene as a precursor for photocatalysts.[105]

Li *et al.*[96] effectively controlled the surface terminations in $Ti_3C_2T_x$ and synthesized TiO_2/$Ti_3C_2T_x$ hybrids by performing calcination of F- terminated and OH- terminated $Ti_3C_2T_x$, separately.[96] OH- terminated $Ti_3C_2T_x$ was obtained by treating $Ti_3C_2T_x$ with NaOH. Uniformly truncated octahedral bipyramidal TiO_2 particles with exposed [001] facets were preferentially formed on the surface of F- terminated MXenes after calcination. This material exhibited two times enhanced hydrogen production compared to TiO_2/$Ti_3C_2T_x$ produced from OH–terminated counterparts.[96]

3.3.2 MXenes as cocatalysts. As of now, MXenes are being used as cocatalysts that can promote the separation of photogenerated charge carriers, thereby facilitating the photocatalytic activity of semiconductors (*e.g.*, TiO_2). Being economical and non-toxic, with a band gap $\approx$3 eV, TiO_2 is the most studied photocatalyst so far. Its band structure permits both reduction and oxidation reactions under UV light irradiation as initially shown by Fujishima and Honda.[106,107] Table 1 summarizes several examples of MXene-based photocatalysts used in the most recent years for hydrogen production through water splitting. The synthetic approaches to combine different semiconductor photocatalysts with MXenes, and several reaction parameters are also presented. These reports demonstrated that the use of MXenes as cocatalysts could greatly improve the photoactivity compared to the use of solely the base photocatalyst.

Wang *et al.*[97] synthesized TiO_2/$Ti_3C_2T_x$ composites in different weight ratios (5–50% $Ti_3C_2T_x$) under HTT. Photocatalytic hydrogen evolution from water using methanol as a hole scavenger was monitored for these materials under visible light irradiation. Inclusion of 5 wt% $Ti_3C_2T_x$ resulted in a 400% enhancement in hydrogen evolution compared to pure rutile TiO_2. Photocatalytic activity was further found to be improved by replacing $Ti_3C_2T_x$ with Ti_2CT_x or Nb_2CT_x, among which 5% Nb_2CT_x exhibited the best performance among the series, with an apparent quantum yield (AQY) of 0.39%. Stability tests performed for three cycles using TiO_2/$Ti_3C_2T_x$ exhibited co nsistent results.

According to the authors, the hydrothermal synthesis method allowed an intimate contact between the semiconductor and the cocatalyst surfaces resulting in a flow of photogenerated electrons. A Schottky barrier thus formed at the interface prevented the electrons from diffusing back, thereby preventing charge recombination. In addition, the highest value of the work function for Nb_2CT_x (4 eV) among those of the series reflected a larger Schottky barrier explaining its best performance among the series (see Fig. 6).[97]

In a similar manner, Li *et al.*[108] synthesized TiO_2/$Ti_3C_2T_x$ nanoflowers from Ti_3C_2 under HTT followed by ion exchange and calcination.[108] Initially, $Na_2Ti_3O_7$–Ti_3C_2 composites were synthesized hydrothermally, and were then treated with HCl to replace Na^+ with H^+ producing $H_2Ti_3O_7$–Ti_3C_2. These materials were then calcined at 300–500 °C to produce TiO_2/$Ti_3C_2T_x$. Optimum materials obtained after calcination at 500 °C displayed overall water splitting in the absence of a sacrificial agent, with an AQY of 5.86%. The better performance was attributed to the ability of 3D porous nanoflower-like morphology to provide more active sites, and its greater ability to reflect and scatter light and reduce the diffusion length of photogenerated charge carriers. The Schottky junction formed at the interface hindered charge recombination resulting in more electrons participating in H_2 evolution and more holes participating in O_2 evolution.[108]

Su *et al.*[98] synthesized a series of $Ti_3C_2T_x$/TiO_2 composite photocatalysts by adding an aqueous dispersion of stacked monolayer $Ti_3C_2T_x$ in different weight ratios to commercial TiO_2 (Degussa P25), under sonication.[98] Photocatalytic tests performed in the presence of methanol as a hole scavenger indicated a 9 times higher hydrogen evolution rate (AQY = 15.8%) for the composite with 5 wt% MXene, compared to P25. Interestingly, this composite material exhibited a 2.5 times better performance than when the multi-layer MXene counterpart was used as the cocatalyst. The significantly enhanced activity is attributed to the superior electron conductivity of monolayer $Ti_3C_2T_x$ and enhanced charge separation at the interface. It is to be noted here that after four cycles, the hydrogen production rate decreased from 2650 μmol g^{-1} h^{-1} to 2300 μmol g^{-1} h^{-1}. Since the structural and surface properties of the photocatalyst recovered after the reaction remained unchanged, the observed decrease in the rate was attributed to the probable detachment between TiO_2 and $Ti_3C_2T_x$.[98]

Table 1 Compilation of synthetic and photocatalytic aspects of MXene-based materials in hydrogen production through the water splitting reaction[a]

Photocatalyst/cocatalyst	Synthetic method	Hole scavenger	Light region	Optimum H_2 production rate [μmol g^{-1} h^{-1}]	AQY [%]	Ref.
TiO_2/Ti_2CT_x	HTT (95 °C for 4 h)	Methanol (25%)	Visible	~32	0.27	97
TiO_2/Ti_3C2T_x				17.8	0.15	
TiO_2/Nb_2CT_x				~46	0.39	
$Nb_2O_5/C/Nb_2C$	Oxidation under CO2 (850 °C for 0.5–1.5 h)	Methanol (25%)	Visible	7.81	0.11	95
TiO_2/Ti_3C_2 nanoflowers	HTT (140 °C for 12 h), ion exchange (HCl, 24 h) and calcination in air (300–500 °C for 3 h)	Methanol (20%)	UV-visible	783.11	5.86 (350 nm)	108
TiO_2/Ti_3C2T_x composites	Sonication	Methanol (25%)	UV	2650	15.8 (305 nm)	98
C-doped TiO_2 derived from $Ti_3C_2T_x$	HTT (160 °C for 9 h)	TEA (10%)	Full spectrum	33.04	NP	105
Truncated octahedral bipyrmidal TiO_2/Ti_3C_2 hybrids	Calcination in air (550 °C for 4 h)	Glycerol (10%)	Full spectrum	~130	0.9 (365 nm)	96
0D/1D/2D Ag/Nb_2O_5@Nb_2CT_X nanohybrids	HTT (180 °C for 0.5–10 h) and *in situ* photodeposition	Methanol (7%) Glycerol (7%)	Full spectrum	682 824	1.6 (313 nm)	109
$La_2Ti_2O_7/Ti_3C_2$ composites	HTT (200 °C for 24 h)	Methanol (40%)	UV	1594	NP	110
CdS/Ti_3C_2 composites	HTT (180 °C for 12 h)	Lactic acid (22%)	Visible	14 342	40.1 (420 nm)	111
1D/2D CdS/Ti_3C_2 nanocomposites	HTT (160 °C for 48 h)	Lactic acid (10%)	Visible	2407	35.6 (420 nm)	112
1D/2D CdS/Ti_3C_2 composites	HTT (200 °C for 5 h)	TEA (20%)	Simulated solar light	63.53	2.28	113
2D/2D CdS/Ti_3C2T_x composites	HTT (80 °C for 48 h)	Lactic acid (10%)	Visible	3226	47 (420 nm)	114
CdS/TiO_2–C (derived from $Ti_3C_2T_x$)	γ-ray irradiation	Lactic acid (20%)	Visible	1480	NP	115
CdS/Mo_2C	HTT 180 °C for 24 h)	Lactic acid (17%)	Visible	17 964	48.06 (420 nm)	116
2D/2D $ZnIn_2S_4$/2D $Ti_3C_2T_x$ sandwich like hierarchical heterostructures	Reflux (80 °C for 2 h)	TEA (10%)	Visible	3475	11.14 (420 nm)	117
$BiVO_4$@$ZnIn_2S_4/Ti_3C_2$ QD	Ultrasonication	None	Visible	6.16	2.9 (460 nm)	118
Ti_3C_2@$TiO_2/ZnIn_2S_4$ ternary composites	HTT (180 °C for 3 h)	Na_2S/Na_2SO_3	Simulated solar light	1185.8	NP	119
CdS–MoS_2–Ti_3C_2 composites	HTT (160 °C for 24 h)	Na_2S/Na_2SO_3	Visible	9679	26.7 (420 nm)	120
MoxS@TiO_2@Ti_3C_2 composites	HTT (160 °C for 12 h)	TEA	UV-visible-near IR	10 505.8	7.535	121
CdS@Au/Ti_3–xC_2T_y ternary composites	Solvothermal treatment (180 °C for 12 h)	Lactic acid (10%)	Visible	5371	16.7 (420 nm)	122
2D/2D g-C_3N_4/Ti_3C_2 nanosheets	Electrostatic self-assembly	TEA (10%)	Visible	72.3	0.81 (400 nm)	99
2D/0D g-C_3N_4/Ti_3C_2 composites	Freeze drying	TEA (15%)	Simulated solar light	5111.8	3.654	123
p-g-$C_3N_4/Ti_3C_2T_x$ hollow spheres	Electrostatic self-assembly with a sacrificial template	TEA (10%)	Visible	982.8	NP	124
2D/3D g-C_3N_4/Ti_3C_2 hybrid	Calcination under N_2 (550 °C for 2 h)	TEA (10%)	Visible	116.2	NP	125
0D black phosphorous/2D Ti_3C_2/2D g-C_3N_4	Grinding and sonication	TEA (10%)	Visible	18 420	17.6 (420 nm)	126
$Chl/Ti_3C_2T_x$	Wet chemical	Ascorbic acid	Visible	1010	NP	127
Chl-1@ChI-2/0$Ti_3C_2T_x$	Wet chemical	Ascorbic acid	Visible	143	NP	128

[a] ~ Data taken from a graphical representation of the corresponding reference; NP: value not provided; TEA = triethanolamine.

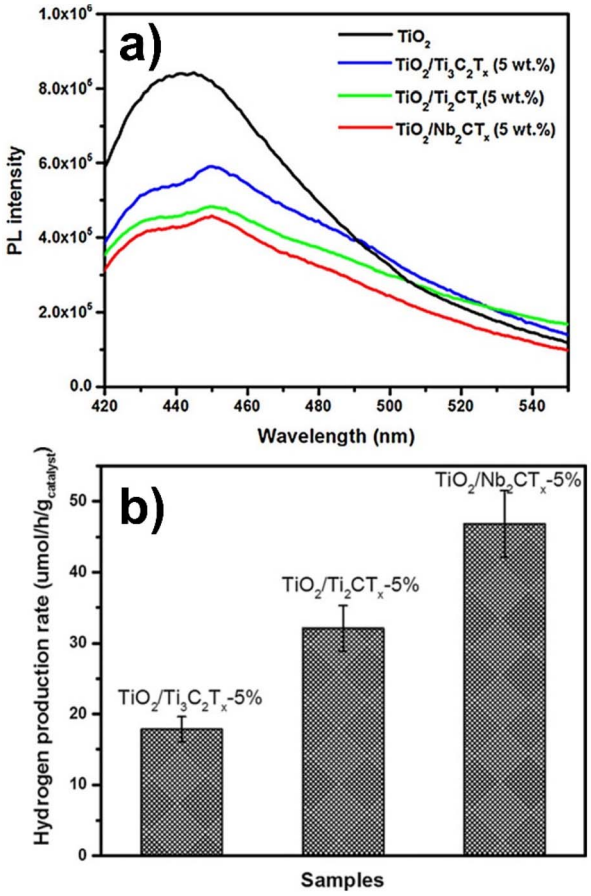

Fig. 6 (a) Photoluminescence spectra of pure TiO_2 along with those of the materials with different 5 wt% metal carbide cocatalysts. The excitation wavelength was 400 nm. (b) Photocatalytic hydrogen production rates obtained for different metal carbide cocatalysts. Reproduced with permission from ref. 97, Copyright 2016 European Chemical Societies Publishing.

In an attempt to study the charge carrier dynamics, Debow *et al.*[129] observed that band bending resulted in the formation of a Schottky barrier at the contact point between TiO_2 and $Ti_3C_2T_x$. The hot electrons generated from MXenes are rapidly (180 fs) transferred into the conduction band of TiO_2, indicating strong electronic coupling.[129]

Peng *et al.*[109] fabricated 1D Nb_2O_5 nanorod arrays with a [001] orientation on 2D Nb_2CT_x under HTT followed by the photodeposition of Ag nanoparticles. While the low work function of –OH terminated Nb_2CT_x promoted the trapping of photogenerated holes from Nb_2O_5 nanorods, Ag nanoparticles acted both as an electron reservoir and active sites for hydrogen evolution, resulting in an effective spatial separation of charge carriers. Under solar light irradiation, these nanohybrids produced 824.2 μmol g^{-1} h^{-1} using glycerol as the sacrificial agent.[109] Studies regarding stability and reusability were also carried out by these authors. It was found that hydrogen production remained unchanged after three sequential cycles. Moreover, the morphology, phase composition and surface functional groups of $Ag/Nb_2O_5@Nb_2CT_x$ recovered after the reaction, was not altered significantly.

In another interesting study, Wang *et al.*[110] hydrothermally synthesized $La_2Ti_2O_7/Ti_3C_2T_x$ composites. The introduction of 20 wt% $Ti_3C_2T_x$ resulted in a 16 times higher hydrogen production rate than that of pristine $La_2Ti_2O_7$, in the presence of methanol. Solid-state NMR and Raman spectroscopy clearly indicated the formation of graphene quantum dots in $Ti_3C_2T_x$. In contrast to the vast majority of reports on MXene-based photocatalysts, these authors proposed that graphene quantum dots produced *in situ* during the HF etching process, rather than $Ti_3C_2T_x$ itself, played the role of a co-catalyst during the photocatalytic reaction, by suppressing the charge recombination.[110] However, in our understanding, no further reports have appeared in this regard.

Metal sulfides are another category of semiconductors widely investigated for photocatalytic applications. In comparison to MOs, these materials comprise a narrow band gap, enabling a visible light response, and hence, several metal sulfides were also coupled with MXenes in photocatalytic water splitting.

Ran *et al.*[111] integrated $Ti_3C_2T_x$ nanoparticles with a series of metal sulfides in different proportions. Combination with CdS resulted in the best hydrogen yields with an apparent quantum efficiency of 40.1%. Similarly, 386% and 217% enhancement of the photocatalytic performance was respectively observed for $Zn_{0.8}Cd_{0.2}S$ and ZnS by incorporating 1% of $Ti_3C_2T_x$. The authors attributed this to a favourable Fermi level position and superior electronic conductivity of MXenes. Significant variations in the performance of $CdS/Ti_3C_2T_x$ were not observed during seven successive cycling tests. A comparison between the fresh and used materials also indicated consistency in the crystalline phase, morphology and size.[111]

Hydrothermally synthesized 1D CdS nanorod/2D $Ti_3C_2T_X$ nanosheet heterojunctions displayed 7 times increased hydrogen production compared to pristine CdS nanorods with an AQY of 35.6%, under visible light irradiation in the presence of lactic acid. In this study also, no obvious decrease in hydrogen production was observed for five consecutive cycles. The enhanced performance was attributed to the accelerated charge separation facilitated by the Schottky heterojunction formed, as well as to the synergistic interactions between the components.[112]

Another study highlighting the effectiveness of combining CdS with $Ti_3C_2T_x$ under HTT, reported hydrogen evolution rates higher than that of pure CdS and CdS@Pt, with an AQY of 2.28%. The authors also noted 87.61% retention of performance after three cycles. Apart from a slightly weakened intensity of the XRD peaks, no significant changes were observed for the material recovered after the reaction.[113] $CdS/Ti_3C_2T_x$ composites forming 2D/2D Schottky heterojunctions exhibited a 5-fold enhancement of photocatalytic performance of pure CdS, with an AQY of 47%. Stable performance was observed for five consecutive cycles. In this case also, the superior performance was attributed to an intimate interface promoting rapid charge transfer and hindering their recombination, which was confirmed by DFT calculations.[114]

In another interesting study, $Ti_3C_2T_x$/CdS nanocomposites prepared under γ-ray irradiation, upon NaOH treatment resulted in the formation of TiO_2–C/CdS nanocomposites. This material exhibited hydrogen evolution rates 6.4 and 7.0 times greater than that of $Ti_3C_2T_x$/CdS and CdS, respectively. In this case, oxygen vacancies in amorphous TiO_2 also acted as electron trapping sites to facilitate the transfer of photoexcited electrons. No significant loss in photocatalytic performance was observed for five cycles.[115]

Jin *et al.*[116] synthesized hybrid structures of 2D Mo_2C sheets covered with CdS nanocrystals. This hybrid photocatalyst with 2.5 wt% of Mo_2C exhibited a 11% higher hydrogen production rate than noble-metal catalysts with an apparent quantum yield of 48.06%.[116]

Zuo *et al.*[117] used $Ti_3C_2T_x$ nanosheets to support ultrathin $ZnIn_2S_4$ nanosheets, forming sandwich-like hierarchical heterostructures. The resultant materials exhibited improved specific surface area, pore diameter, and hydrophilicity.

A 6.6 times improvement in photocatalytic hydrogen evolution was observed for pure $ZnIn_2S_4$ with an AQY of 11.14%, which was attributed to facile charge transfer and inhibition of their recombination (see Fig. 7). The values of hydrogen evolved remained nearly constant after six cycles.[117]

A hierarchical core@shell structure consisting of $BiVO_4$@-$ZnIn_2S_4$ over which Ti_3C_2 quantum dots were uniformly distributed, was obtained by following a multi-step hydrothermal approach. This material exhibited overall water splitting under visible light irradiation. Stable photocatalytic performance was observed during five cycles. The addition of Ti_3C_2 significantly improved the light absorption efficiency and range, extending towards the near infrared region. The close contact between $BiVO_4$ and $ZnIn_2S_4$ resulted in effective charge separation. MXenes captured electrons from the conduction band of $ZnIn_2S_4$ and thereby suppressed charge recombination. The inherent confinement effects of Ti_3C_2 in the form of quantum dots is also found to contribute.[118]

Similarly, Huang *et al.*[119] hydrothermally generated TiO_2 nanoparticles on the surface of Ti_3C_2 nanosheets, which were then subjected to an additional HTT to obtain hierarchical Ti_3C_2@TiO_2/$ZnIn_2S_4$ structures. Under simulated solar light irradiation, hydrogen generation rates 9.1 times higher than that of Ti_3C_2@TiO_2 and 4.6 times higher than that of pure $ZnIn_2S_4$ were obtained. This was attributed to the superior light harvesting, availability of sufficient active sites, intimate interfacial contact and efficient charge separation resulting from the formed heterojunction. A minor decrease in H_2 amounts was observed by the authors after four cycles and was attributed to the mass loss that occurred during photocatalyst separation and recovery.[119] The CdS–MoS_2–$Ti_3C_2T_x$ composite exhibited a 251.3% enhancement of the hydrogen generation rate of CdS–MoS_2, under visible light irradiation, with an AQY of 26.7%. Here, the authors identified three mechanisms for the migration of photogenerated electrons from the conduction band of CdS directly to MoS_2 or $Ti_3C_2T_x$ and to MoS_2 through $Ti_3C_2T_x$. The adsorbed H^+ will get converted into hydrogen either on the surface of $Ti_3C_2T_x$ or MoS_2 edges, implying the significance of the synergy between the components. In this study, the authors noted that adding MXenes above 2% can induce agglomeration and can act as recombination sites for the charge carriers.[120] Hydrothermally enabled *in situ* growth of TiO_2 on Ti_3C_2 nanosheets followed by the distribution of MoS_2 on the surface resulted in the formation of Mo_xS@TiO_2@Ti_3C_2 with molybdenum vacancies and double cocatalysts. This unique composite displayed a 193 times higher hydrogen production rate compared to pure TiO_2. The authors observed no significant decrease in hydrogen evolution rates for 3 cycles. Molybdenum vacancies acted as active sites and suppressed charge carrier recombination, whereas MXenes enhanced the electron conductivity.[121]

Li *et al.*[122] synthesized a ternary CdS@Au/$Ti_{3-x}C_2T_y$ composite by a solvothermal method. In particular, core−shell structured CdS@Au nanojunctions were supported on MXenes. The composite with 1 wt% $Ti_{3-x}C_2T_y$ and 0.1 wt% Au resulted in 26.6 times enhancement of hydrogen production compared to pristine CdS. The dual Schottky barriers formed at the interface of CdS/Au and CdS/$Ti_{3-x}C_2T_y$ facilitated photogenerated electron migration from CdS while limiting back transfer, as evident from XPS analysis, Kelvin probe measurements and DFT calculations. Nanoparticles on the surface of $Ti_{3-x}C_2T_y$ nanosheets exhibited signs of aggregation after 4 h which became more pronounced after 29 h, resulting in the decline of photoactivity.[122]

Polymeric compounds are also investigated for photocatalytic reactions among which graphitic carbon nitrides (g-C_3N_4) are the most promising. A proper band edge position and narrow bandgap (≈2.9 eV) permits this material to function under visible light. Su *et al.*[99] adapted an electrostatic self-assembly approach to synthesize 2D/2D Ti_3C_2/g-C_3N_4 composites by introducing varying amounts of monolayer Ti_3C_2. Incorporating 3 wt% Ti_3C_2 resulted in a 10-fold increase in photocatalytic hydrogen evolution performance of pure g-C_3N_4, under visible light irradiation in the presence of TEA as a hole scavenger. The hydrogen evolution rates were consistent for 3 consecutive cycles of photocatalytic reaction. Moreover, no changes were observed in the composition and structure after

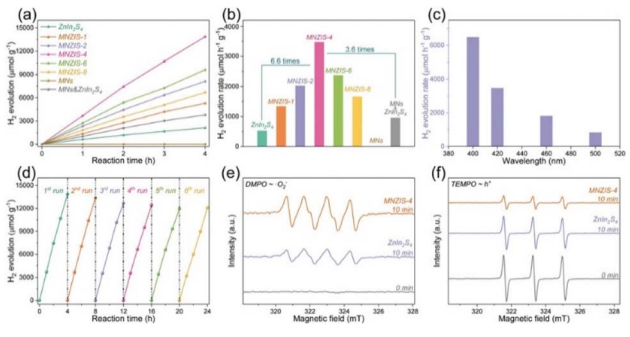

Fig. 7 (a) Time–yield plots and (b) comparison of photocatalytic H_2 evolution for $ZnIn_2S_4$, $Ti_3C_2T_x$- $ZnIn_2S_4$ (MNZIS-*X*), MNs, and a physical mixture of MNs & $ZnIn_2S_4$, (c) H_2 evolution rates for MNZIS-4 with different long-pass cut-off filters, (d) cyclic experiments of H_2 evolution using MNZIS-4, and EPR spectra of (e) DMPO $^{\bullet}O_2^-$ and (f) TEMPO h^+ for MNZIS-4 and $ZnIn_2S_4$. Reproduced with permission from ref. 117, Copyright 2020 Wiley Publications.

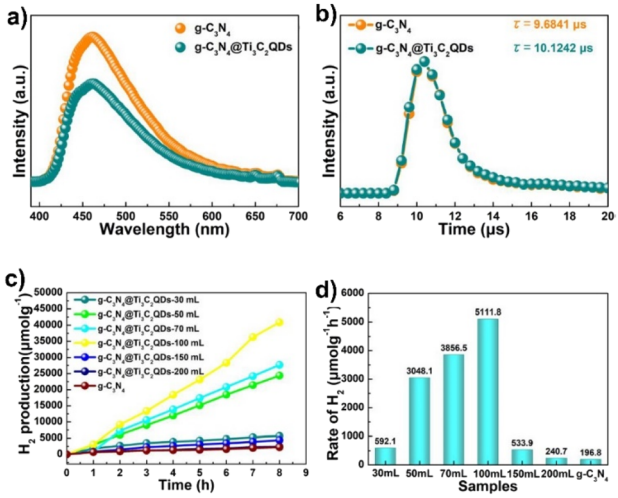

Fig. 8 (a) Steady photoluminescence (PL) and (b) time-resolved fluorescence decay spectra of g-C_3N_4 and g-C_3N_4@Ti_3C_2 QDs-100 mL composites, $\lambda_{ex} = 325$ nm. (c) Photocatalytic H_2 evolution and (d) rate of g-C_3N_4 NSs, Pt/g-C_3N_4, Ti_3C_2 MXene sheet/g-C_3N_4 and g-C_3N_4@Ti_3C_2 QDs. Reproduced with permission from ref. 123, Copyright 2019 The Royal Society of Chemistry.

the reaction. A slight decrease in light absorption was attributed to the probable separation of Ti_3C_2 flakes from the g-C_3N_4 nanosheets. The Schottky junction formed at the interface with the maximum contact surface greatly enhanced electron transport and inhibited their recombination with holes.[99]

Introduction of 5.5 wt% of Ti_3C_2 QDs in g-C_3N_4 by the freeze-drying method resulted in 26 times higher than that of pure g-C_3N_4, in the presence of TEA (see Fig. 8). Interestingly, these materials also outperformed Pt/g-C_3N_4. The authors attributed the better performance of these materials to the close contact between Ti_3C_2 and g-C_3N_4, large specific surface area and small particle size of Ti_3C_2 quantum dots. The authors also examined the recyclability and stability of these materials. No significant decrease in the amount of H_2 produced was observed during three consecutive eight hour cycles.[123]

Kang *et al.*[124] synthesized g-C_3N_4/$Ti_3C_2T_x$ hollow spheres, by electrostatic layer-by-layer assembly, in the presence of amino-functionalized polystyrene beads as sacrificial templates. Protonation of g-C_3N_4 sheets was carried out using HCl. The resultant hybrid materials exhibited a 3.5 times better hydrogen production rate compared to pure protonated g-C_3N_4, and a 1.22-fold higher hydrogen production rate than its non-spherical counterpart. The rate of hydrogen production remained approximately the same during three repeated cycles. The 3D hollow structure enabled enhanced light absorption, while the 2D heterostructure between the components shortens the electron migration distance and high surface area providing sufficient active sites.[124]

2D/3D g-C_3N_4/Ti_3C_2 hybrids were fabricated by calcination of melamine together with pre-formed MXenes. This unique material displayed a 6 times higher hydrogen production rate compared to pristine g-C_3N_4 under visible light irradiation, which was attributed to the Schottky junction formed, preventing charge recombination, together with high electron conductivity of Ti_3C_2 and an intimate interface.[125] The performance remained stable for five cycles. Also, the crystal structure of fresh and recycled samples remained the same, indicating better stability.

Introduction of Ti_3C_2 into a heterojunction formed between black phosphorus quantum dots and g-C_3N_4 resulted in hydrogen evolution rates 47.2 and 19.4 times, respectively, higher than that of bulk g-C_3N_4 and ultrathin g-C_3N_4. Stable photocatalytic hydrogen evolution was observed for six consecutive cycles. With the apparent quantum yield reaching 17.6%, the composite photocatalysts with an optimum mass ratio exhibited enhanced light absorption and strong interfacial contact. Here, Ti_3C_2 acted as a bridge to accelerate charge transfer between black phosphorous and g-C_3N_4.[126]

Li *et al.*[127] fabricated organic–inorganic composites by depositing supramolecular aggregates of a chlorophyll derivative (zinc methyl 3-devinyl-3-hydroxymethyl-pyropheophorbide a (Chl)) on the surface of $Ti_3C_2T_x$. In this case, Chl served as an organic semiconductor and MXene, a co-catalyst. For 2 wt% ChI, 52 ± 5 μmol h^{-1} g^{-1} hydrogen evolution was observed under visible light irradiation in the presence of ascorbic acid. Efficient light harvesting followed by exciton transfer in Chl aggregates and the resultant charge separation at the interface were responsible for the observed performance.[127] In a similar study, Li *et al.*[128] grafted chlorophyll derivatives, Chl-1 and Chl-2, on the surface of 2D $Ti_3C_2T_x$ forming a Chl-1@Chl-2@$Ti_3C_2T_x$ composite. Under visible light irradiation, the hydrogen evolution rate was found to be 143 μmol h^{-1} g^{-1} which was substantially higher than the values obtained individually for Chl-1@$Ti_3C_2T_x$ or Chl-2@$Ti_3C_2T_x$.[128]

3.4. Photocatalytic applications for CO_2 reduction

Photocatalytic conversion of CO_2 into consumable chemicals and fuels is an ideal approach to harvest solar energy and at the same time counter the challenges related to increasing CO_2 emissions. A summary of frequently used reactants, catalysts and products is schematically shown in Fig. 9. Apart from the undesired charge carrier recombination generally encountered in photocatalysis, poor surface adsorption and activation of CO_2 molecules must also be addressed in this case. Even though addition of cocatalysts is found to be effective, noble metal free compositions are still scarce in this regard. In comparison to water splitting, fewer studies have been carried out so far using $Ti_3C_2T_x$ for the photocatalytic conversion of CO_2. It needs to be noted here that $Ti_3C_2T_x$ (or MXenes in general) itself is a source of carbon, and therefore, additional care should be taken while interpreting the results.

Table 2 summarizes several examples of MXene-based photocatalysts used in the most recent years for CO_2 reduction. The synthetic approaches to combine different semiconductor photocatalysts with MXenes and several reaction parameters are also presented. These reports demonstrated that the use of MXenes as a cocatalyst greatly improves the photocatalytic activity compared to the use of solely the semiconductor photocatalyst. As shown in Table 2, $Ti_3C_2T_x$, as a co-catalyst,

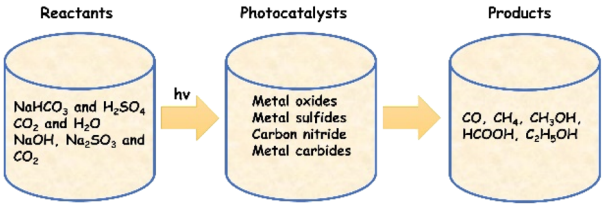

Fig. 9 Schematic representation of photocatalytic CO_2 conversion highlighting frequently used reactants, photocatalysts and possible products that can be formed.

promotes the separation of charge carriers, leading to the formation of mainly C1 products (*i.e.*, CO, formaldehyde, formic acid, methanol and CH_4). The absence of C2 product formation (*e.g.*, ethanol, ethylene or oxalic acid) indicates that $Ti_3C_2T_x$ cannot change the energy barrier of the photocatalyst.

3.4.1 MXenes as a photocatalyst-cocatalyst precursor. Low *et al.*[130] studied the effect of calcination temperature on the stability of $Ti_3C_2T_x$ and observed an *in situ* growth of surface TiO_2 nanoparticles. Photocatalytic CO_2 reduction was carried out over these materials under light irradiation from a Xe arc lamp. $NaHCO_3$ and HCl were used as the reactants to *in situ* generate CO_2 and H_2O vapours. Formation of CH_4 as a major product with small amounts of methanol and ethanol was observed for the material obtained after calcination at 550 °C. The CH_4 production rate was 3.7 times higher than that of commercial TiO_2 (P25). The labelling of the products confirmed that the hydrocarbon products originated from CO_2. Moreover, the rate of CH_4 production remained stable for five consecutive cycles. The *in situ* growth of TiO_2 resulted in an intimate contact with Ti_3C_2, facilitating the transfer and accumulation of photogenerated electrons for multi-electron CO_2 conversion to take place. In addition, increased specific surface area and enhanced light absorption properties of the composite also contributed towards performance enhancement. The authors also proposed that an excess of $Ti_3C_2T_x$ will compete with the light absorption properties of TiO_2, thereby decreasing the efficiency.[130]

In the same direction, Song *et al.*[132] synthesized 3D hierarchical $Ti_3C_2T_x$ and performed calcination in air to generate TiO_2 on the surface of nanosheets resulting in the formation of a heterostructure with bimodal macro-mesoporosity. These materials were used for photocatalytic conversion of gas phase CO_2 produced from the reaction between $NaHCO_3$ and H_2SO_4 under simulated solar light. In the absence of CO_2, product formation was not observed. Also in this case, the composites obtained after calcination at 500 °C, exhibited a 2-fold increase in the CH_4 evolution rate compared to commercial TiO_2. In this case, the 3D hierarchical structure promoted enhanced light absorption and efficient electron–hole separation whereas strong adsorption of CO_2 on Ti_3C_2 ensured the availability of electrons for the reaction.[132]

3.4.2 MXenes as cocatalysts. Surface alkalinization was found to have a profound effect on electronic conductivity of MXenes. A simple KOH treatment can effectively replace the surface –F groups in MXenes with hydroxyl groups. For the photoreduction of gas phase CO_2 carried out with H_2O as the hydrogen source, the presence of alkalinized $Ti_3C_2T_x$ as a cocatalyst improved the CH_4 production rate of the commercial TiO_2 photocatalyst by 277 times, as shown in Fig. 10. However, on addition of above 5 wt% Ti_3C_2, P25 was shielded from light irradiation, decreasing the activity. In this study, no carbonaceous products were determined during the control experiments performed over pure $Ti_3C_2T_x$ or by replacing CO_2 with Ar. CO_2 molecules are acidic in nature and the presence of basic OH surface functionalities on Ti_3C_2 acted as active sites for adsorption. The electron rich environment created in Ti_3C_2 after capturing the conduction band electrons from TiO_2, readily improves the reduction of the adsorbed CO_2 molecules, thus explaining the enhanced activity.[131] Similar to the studies carried out by Ye *et al.*,[131] surface-alkalinized Ti_3C_2 was integrated with ZnO by Li *et al.* following an electrostatic self-assembly strategy. Here, the presence of 7.5 wt% of Ti_3C_2 in the composite resulted in a 35 times higher CH_4 production rate and 7 times higher CO production rate, compared to those of pure ZnO. Here, both CH_4 and CO evolution remained constant for three cycles.[138]

The presence of Ru along with TiO_2 on the surface of Ti_3CN MXenes produced a mixture of CO, CH_4 and other hydrocarbons from CO_2 using water as the hydrogen source. With 0.5 wt% Ru, CO and CH_4 production rates increased by 20.5 and 9.3 times, respectively, compared to that of P25. Isotopic labelling studies confirmed CO_2 as the origin of the reaction products. Gas production rates exhibited a 13.4% decrease during the first three cycles. This was attributed to the accumulation of intermediate products on the active sites, hindering further reaction. To confirm this, the photocatalyst was recovered and washed with deionized water. This resulted in a performance similar to that observed during the first cycle.[133]

Wang *et al.*[134] prepared a core@shell structured *meso*-TiO_2@$ZnIn_2S_4$ and different amounts of Ti_3C_2 were deposited on the $ZnIn_2S_4$ shell. This ternary photocatalyst, under UV-visible light irradiation, resulted in CO and CH_4 evolution with slightly better CH_4 selectivity. The better performance in comparison with that of the individual components was attributed to accelerated electron transfer to Ti_3C_2 as well as the enhanced CO_2 adsorption capacity of the 3D mesostructure.[134]

Zeng *et al.*[135] developed a hierarchical heterostructure by decorating Cu_2O nanowires with Ti_3C_2 quantum dots (QDs) on a Cu mesh, adapting an electrostatic self-assembly strategy. Photocatalytic transformation of a CO_2 saturated H_2O medium was carried out under solar light irradiation, and selective formation of CH_3OH was observed. Product yields were found to be 8.25 times higher compared to that of Cu_2O nanowires on a Cu mesh. Interestingly, the presence of MXenes as QDs resulted in a 2.15 times higher methanol yield compared to MXene sheets with the same composition. 89% retention of methanol yield was observed after six cycles of photocatalytic reaction. The authors reported a multi-fold influence of $Ti_3C_2T_x$ on the performance of Cu_2O NWs by enhancing charge transport, carrier density, and light adsorption, as well as by decreasing the band bending edge and limiting charge carrier recombination.[135] Taking into account the good synergy with Cu_2O, a series of $Cu_2O/Ti_3C_2T_x$ heterostructures with varying

Table 2 Compilation of synthetic and photocatalytic aspects of MXene-based materials in CO_2 conversion[a]

Photocatalyst composite	Synthetic method	Reactants	Light region	Products [μmol g^{-1} h^{-1}]	AQY [%]	Ref.
TiO_2/Ti_3C_2	Calcination in air (350–650 °C)	$NaHCO_3$ and HCl	Simulated solar light	CH_4 (0.22) CH_3OH (NP) C_2H_5OH (NP)	NP	130
Alkalinized TiO_2/Ti_3C_2	KOH treatment and physical mixing	CO_2 and H_2O	Simulated solar light	CH_4 (16.61) CO (11.74)	1.61 0.32	131
3D hierarchical $TiO_2/Ti_3C_2T_x$ heterojunction	Calcination in air (300–700 °C for 1 h)	$NaHCO_3$ and H_2SO_4	Simulated solar light	CH_4 (4.41) CO (NP)	NP	132
Ru–Ti_3CN–TiO_2	HTT (180 °C for 4 h)	CO_2 and H_2O	Simulated solar light	CO (99.58 μmol g^{-1} for 5 h) CH_4 (8.97 μmol g^{-1} for 5 h)	NP	133
Core@shell *meso*- TiO_2@$ZnIn_2S_4/Ti_3C_2$	Electrostatic self-assembly	CO_2 and H_2O	Visible	CO (30.5 μmol g^{-1} for 3 h) CH_4 (34 μmol g^{-1} for 3 h)	NP	134
Ti_3C_2 QDs/Cu_2O NWs/Cu mesh	Dip coating and calcination under Ar (200 °C for 1 h)	CO_2 and H_2O	Simulated solar light	CH_3OH (78.50)	NP	135
Ti_3C_2 sheets/Cu_2O NWs/Cu	Dip coating and calcination under Ar (200 °C for 1 h)	CO_2 and H_2O	Simulated solar light	CH_3OH (36.51)	NP	135
Cu_2O/Ti_3C_2 heterojunction composites	HTT (90 °C for 5 h)	CO_2	Simulated solar light	CO (17.55) CH_4 (0.96)	NP	136
2D/2D Ti_3C_2/Bi_2WO_6 nanosheets	HTT (120 °C for 24 h)	$NaHCO_3$ and H_2SO_4	Simulated solar light	CH_4 (1.78) CH_3OH (0.44)	NP	137
Alkalinized Ti_3C_2/ZnO	KOH treatment followed by electrostatic self-assembly	CO_2 and H_2O	Simulated solar light	CO (30.30) CH_4 (20.33)	0.32 0.46	138
2D/2D Ti_3C_2/g-C_3N_4 nanosheets	Calcination under N_2 (550 °C for 2 h)	$NaHCO_3$ and H_2SO_4	Visible	CO (5.19) CH_4 (0.044)	NP	139
2D/2D/0D $TiO_2/C_3N_4/Ti_3C_2$	Electrostatic self-assembly	$NaHCO_3$ and H_2SO_4	Simulated solar light	CO (4.39) CH_4 (1.20)	NP	140
Alkalinized Ti_3C_2/g-C_3N_4	Wet chemical mixing	CO_2 and H_2O	Visible	CO (11.21 μmol g^{-1} for 5 h) CH_4 (0.203 μmol g^{-1} for 5 h) C_2H_4; CH_3CHO	NP	141
Few layer Ti_3C_2/boron-doped g-C_3N_4	Sonication and freeze drying	CO_2 and H_2O	Visible	CO (14.4 μmol g^{-1} for 5 h) CH_4 (0.8 μmol g^{-1} for 5 h) H_2 (3.35 μmol g^{-1} for 5 h)	NP	142
g-C_3N_4/$BiOIO_3/Ti_3C_2$ ternary composites	Electrostatic self-assembly	CO_2 and H_2O	Visible	CO (5.88) CH_4 (1.55)	NP	143
3D hierarchical Co–Co LDH/$Ti_3C_2T_x$ nanosheets	HTT (120 °C for 1 h)	MeCN, H_2O, TEA, $[Ru(bpy)_3]Cl_2$ and CO_2	Visible	CO (12 500) H_2 (NP)	0.92	144
3D hierarchical NiAl LDH/Ti_3C_2	HTT (120 °C for 24 h)	CO_2 and H_2O	Simulated solar light	CO (11.82) CH_4 (1.02)	NP	145
0D/2D $FAPbBr_3/Ti_3C_2$	Wet chemical synthesis	CO_2 and H_2O	Simulated solar light	CO (283.41) CH_4 (17.67) H_2 (4.51)	NP	146
2D/2D $FAPbBr_3/Ti_3C_2$	Wet chemical synthesis	CO_2 and H_2O	Simulated solar light	CO (93.82) H_2 (∼0.9)	NP	147
$Cs_2AgBiBr_6$ nanocrystals/$Ti_3C_2T_x$ nanosheets	Ultrasonication	CO_2 and H_2O	Visible	CO (11.1 μmol g^{-1}) CH_4 (1.3 μmol g^{-1}) H_2 (8.9 μmol g^{-1})	0.083	148

[a] ∼ Data taken from a graphical representation of the corresponding reference; NP: value not provided; MeCN: acetonitrile; TEA: triethanolamine.

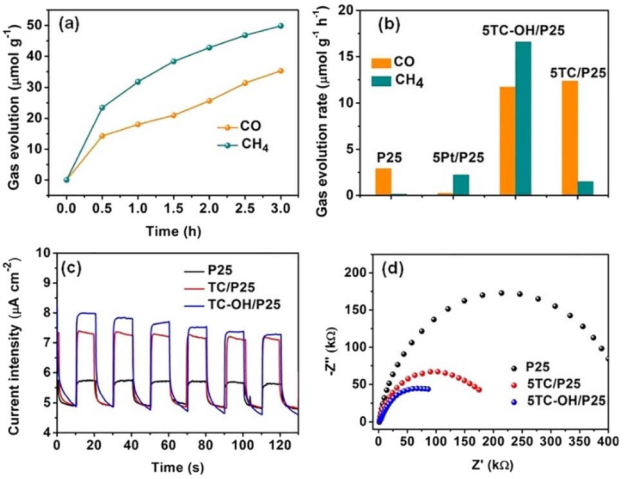

Fig. 10 (a) Gas evolution (CO and CH_4) over 5TC-OH/P25 as a function of irradiation time under a 300 W Xe lamp. (b) Evolution rates of CO and CH_4 over P25, 5Pt/P25, 5TC/P25, and 5TC-OH/P25 under irradiation of a 300 W Xe lamp. (c) Transient photocurrent responses and (d) EIS Nyquist plots of P25, 5TC/P25, and 5TC-OH/P25. Reproduced with permission from ref. 131, Copyright 2018 European Chemical Societies Publishing.

amounts of $Ti_3C_2T_x$, synthesized under hydrothermal conditions were studied for the photoconversion of CO_2 to CO in the absence of a hydrogen source.[136] Addition of 10 mg of $Ti_3C_2T_x$ to the initial precursor solution for Cu_2O synthesis, exhibited 3 times higher CO production rates compared to that of pristine Cu_2O. After three cycles, the amount of CO produced remains 85.8% in comparison with the first cycle. The slight decrease was attributed to the loss of the sample during recovery. Surprisingly, the authors noticed the formation of minor amounts of CH_4. However, since the reaction took place under a pure CO_2 atmosphere, the detection of CH_4 clearly indicates the presence of impurities. Here also, the performance enhancement was attributed to the separation and concentration of electrons on Ti_3C_2, facilitating CO_2 conversion.[136]

The 2D/2D heterojunctions were found to be very active in photocatalytic transformation of CO_2. Therefore, Cao *et al.*[137] fabricated a 2D/2D heterojunction comprising $Ti_3C_2T_x/Bi_2WO_6$ nanosheets under hydrothermal conditions. H_2SO_4 and $NaHCO_3$ were reacted for the *in situ* production of CO_2 which under simulated solar light irradiation produced CH_4 as the major product along with CH_3OH. The results indicate a 4.6 times increment in CH_4 and CH_3OH yields compared to that of pristine Bi_2WO_6 ultrathin nanosheets. The large interfacial surface area resulting from the 2D/2D heterojunction and lower charge transport distance ensured efficient electron transfer from Bi_2WO_6 to Ti_3C_2. This effect coupled with enhanced CO_2 adsorption capacity resulted in the observed performance of this study.[137]

In the same line, Yang *et al.*[139] synthesized a series of 2D/2D Ti_3C_2/g-C_3N_4 ultra-thin heterojunctions by performing calcination of varying amounts of $Ti_3C_2T_x$ and urea. Here, apart from being the precursor for C_3N_4, the presence of urea facilitated the exfoliation of MXene sheets. Photocatalytic conversion of *in situ* generated CO_2 was carried out under visible light irradiation. In the absence of $Ti_3C_2T_x$, CO was the major product observed beside small traces of CH_4. The optimized composite material (with 10 mg of Ti_3C_2) added to the urea precursor, exhibited better yields of CO and CH_4 with 8.1 times higher CO_2 conversion, compared to pure C_3N_4. The performance, structure and morphology of the photocatalyst remained reasonably unchanged during five cycles. The detrimental effect of excess $Ti_3C_2T_x$ was observed in this study also, as previously reported by Low *et al.*[130] The spatial separation of charge carriers facilitated by the formation of an ultra-thin heterojunction, along with an improved CO_2 adsorption and activation was responsible for the improvement of performance.[139]

Integration of Ti_3C_2 quantum dots into a TiO_2/C_3N_4 core@-shell structure resulted in a 2D/2D/0D dual heterojunction photocatalyst. This material exhibited superior photoconversion of *in situ* generated CO_2 into CO and CH_4 along with lower amounts of methanol and ethanol. Product yields remained consistent during four cycles of photocatalytic reactions. The formation of dual heterojunctions was found to be responsible for an improved separation and utilization of charge carriers, resulting in the enhanced performance.[140]

The effect of alkalinized Ti_3C_2 was also observed by coupling it with g-C_3N_4. The composite prepared by mixing 5 wt% alkalinized Ti_3C_2 with g-C_3N_4 exhibited better CO evolution rates during photocatalytic conversion of a CO_2 saturated H_2O medium under visible light irradiation, compared to pure g-C_3N_4. A slight decrease in performance was observed during the first three cycles. However, after washing the catalyst, the activity increased and remained unchanged during the fourth and fifth cycles. A large Fermi level difference between the components contributed towards the enhanced separation of photogenerated charge carriers.[141]

Wang *et al.*[142] synthesized a few-layer Ti_3C_2/B-doped C_3N_4 composite material by adding different volumes of an aqueous solution of $Ti_3C_2T_x$ (1 mg mL^{-1}) to a fixed amount of B-doped g-C_3N_4 (0.4 g). Because of the intimate interfacial contact, the optimal (12 mL) MXene suspension added to the composite exhibited 3.2 times and 8.9 times higher CO and CH_4 yields, respectively, compared to pristine g-C_3N_4 under visible light irradiation. A slight decrease (~14%) in CH_4 and CO production was observed during the first three cycles which was then increased after washing with water.[142]

A $BiOIO_3$/g-C_3N_4 *Z*-scheme heterojunction modified with Ti_3C_2 nanosheets was prepared by Hong *et al.*[143] following an electrostatic self-assembly method. Photocatalytic CO_2 conversion in an aqueous medium under visible light irradiation indicated a 6.6 times higher CO production rate for heterojunction photocatalysts with 4 wt% Ti_3C_2, in comparison with pure g-C_3N_4. No significant reduction in CH_4 and CO yields was observed during three cycles.[143]

Chen *et al.*[144] synthesized a 3D hierarchical Co–Co layered double hydroxide/$Ti_3C_2T_X$ nanoarray under HTT. These materials exhibited a significant enhancement in CO evolution rates, with an apparent quantum efficiency of 0.92%. The high electron conductivity of $Ti_3C_2T_x$, coupled with the nanoarray architecture synergistically contributed towards the

performance enhancement. For these materials, the product yield remained 90% of its initial value after five cycles.[144]

Shi *et al.*[145] synthesized a 3D hierarchical NiAl layered double hydroxide/Ti_3C_2 nanocomposite under HTT by adding different volumes of an aqueous solution of Ti_3C_2 (15 mg mL^{-1}) to the NiAl-LDH precursor solution. Photoconversion of CO_2 was carried out using H_2O as the hydrogen source, producing CO with 92% selectivity, along with CH_4. Up to 3 times enhancement of CO production was observed and the 2D/2D interface interaction was found to promote charge separation and to facilitate CO_2 capture and activation. The CO yield remained constant for four cycles.[145]

Organic–inorganic hybrid perovskites are another interesting category of materials coupled with MXenes for photocatalytic applications. Que *et al.*[146] anchored $FAPbBr_3$ QDs on Ti_3C_2 nanosheets resulting in a composite 0D/2D heterojunction photocatalyst for CO_2 reduction. The amount of Ti_3C_2 in the composite was varied between 0 and 1 mg. Under simulated solar light irradiation, CO was formed as the major product along with minor quantities of CH_4 and H_2 as shown in Fig. 11. In the presence of 0.2 mg of Ti_3C_2, CO yields were found to be 1.84 times higher compared that of to pure $FAPbBr_3$. No significant changes in product yields were observed during three reaction cycles. Ti_3C_2 QDs served as the electron acceptor as well as provided more active sites.[146]

In another study, $FAPbBr_3$ nanoplates were combined with Ti_3C_2 by Que *et al.*[147] resulting in a 2D/2D Schottky heterojunction. A 1.5-fold enhancement in average CO production was observed for the composite, compared to pure halide perovskite.[147] Zhang *et al.*[148] assembled whole inorganic halide double perovskite $Cs_2AgBiBr_6$ nanocrystals (NCs) on $Ti_3C_2T_x$ nanosheets. Superior product yields with 71% selectivity to CO, were obtained for the heterostructures, compared to the individual components. The authors used the electron consumption yield to determine the stability of the material. It remained almost unchanged after 3 cycles. Structural or morphological changes were also not observed during the reaction. The presence of $Ti_3C_2T_x$ reduced the large exciton binding energy of $Cs_2AgBiBr_6$ and promoted the formation of free charge carriers with prolonged life times. Charge carrier recombination was therefore suppressed and this together with enhanced CO_2 adsorption, resulted in better performance.[148]

3.5. Photocatalytic applications for N_2 photofixation

In addition to the well-established photocatalytic applications presented above, the MXenes are used as a cocatalyst in photocatalytic systems for the N_2 reduction reaction (NRR) to ammonia. In contrast to modern Haber-Bosch technology, which directly utilizes fossil fuels through intensive energy processes at high pressure and temperature and with high CO_2 emissions,[149,150] the NRR is regarded as an environmentally friendly, sustainable and green NH_3 synthesis that utilises N_2 and water molecules under mild conditions.[151] Obtaining high reaction efficiencies is primarily constrained by electron–hole recombination and limited interfacial charge transfer, but it is also difficult to activate and break the strong and stable NN bond.[152] The effectiveness of the NRR can be increased by using MXenes as a cocatalyst to create Schottky junctions with semiconductor materials. Table 3 highlights a few examples of MXene-based photocatalysts that have been applied recently for the NRR.

The 0D/2D $AgInS_2/Ti_3C_2$ *Z*-scheme heterostructures constructed by HTT, with various mass ratios of $AgInS_2$, showed a notable improvement in photocatalytic activity for the NRR, according to Qin *et al.*[153] For the mass ratio of 30% $AgInS_2$ in N_2 saturated solution and under visible light, the greatest ammonia yield rate was 38.8 μmol g^{-1} h^{-1}, with an AQY = 0.07% at 420 nm. The utilization of Ti_3C_2 MXenes as a cocatalyst and *Z*-scheme heterojunction, allowed the effective charge separation and migration of photogenerated electrons and holes, which are responsible for the photocatalytic activity for the NRR.

According to Chang *et al.*,[154] the usage of partly reduced Ti_3C_2 (r-Ti_3C_2) with Au nanospheres interlaminated in a layered r-Ti_3C_2 structure helped to expose several low-valence Ti sites that act as active sites. Injection of photogenerated hot electrons from Au nanospheres under illumination reduces N_2 molecules, which are then captured and activated at the active site. In N_2 saturated water, the NRR of r-Ti_3C_2/Au generated NH_4^+ at a rate of 12.4 μmol g^{-1} h^{-1} under visible light, which is 5.9 and 10.3 times higher than those of Ti_3C_2/Au and r-Ti_3C_2, respectively, while under white light the rate was 22.6 μmol g^{-1} h^{-1}, which is 5.8 and 10.2 times higher than those of Ti_3C_2/Au and r-Ti_3C_2. By measuring the quantity of ammonia generated in pure water under monochromatic light irradiation, the apparent quantum efficiencies (AQE) of r-T_3C_2/Au were found to reach 0.697% at 520 nm. The NH_3 production rate increased to 21.26 μmol g^{-1} h^{-1} when the lighting source was changed to simulated sunlight irradiation (by using an AM 1.5G filter).

The material exhibits high stability, with ammonia generation remaining close to 95%, according to the results of five successive stability test cycles. This may be due to the electrons that are constantly produced and transferred from the Au nanospheres to Ti_3C_2 under illumination, which can prevent oxidation of MXenes.

Hao *et al.*[155] demonstrated outstanding activity for the NRR in water at room temperature using a RuO_2-loaded TiO_2-MXene

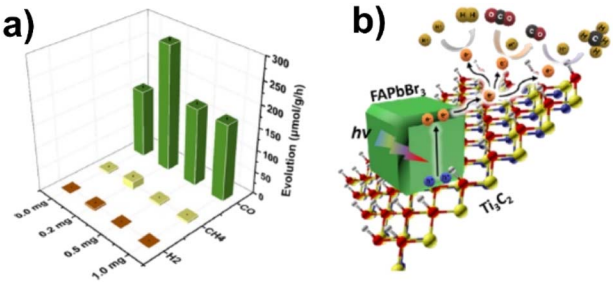

Fig. 11 (a) Photocatalytic CO_2 reduction performances of $FAPbBr_3$/*x*-Ti_3C_2 (*x* = 0.0, 0.2, 0.5, and 1.0) in deionized water under AM 1.5 G (150 mW cm^{-2}). (b) Schottky heterojunction photocatalytic system for CO_2 reduction in $FAPbBr_3$/*x*-Ti_3C_2. Reproduced with permission from ref. 146, Copyright 2021 American Chemical Society.

Table 3 Compilation of synthetic and photocatalytic aspects of MXene-based materials in N_2 photofixation[a]

Photocatalyst	Preparation methods	Reaction conditions	Light source	Sacrificial reagent	NH_3 production [μmol g^{-1} h^{-1}]	AQY [%]	Ref.
0D/2D $AgInS_2/Ti_3C_2$	HTT (150 °C for 5 h)	20 mg of sample dispersed in 100 mL 20% methanol solution, RT	300 W xenon lamp (>400 nm)	Methanol	38.8	0.07 (420 nm)	153
r-Ti_3C_2/Au	Solvent-driven	80 mg of the photocatalyst and 50 mL of water, RT	300 W xenon lamp	None	22.6[b] 12.4[c]	0.697 (520 nm)	154
		200 mg of the photocatalyst and 50 mL of water, RT	Simulated solar light		21.26		
RuO_2@TiO_2-MXene	HTT (150 °C for 10 h)	50 mg of photocatalyst with 100 mL distilled water	300 W xenon lamp, full spectrum (100 mW cm^{-2})	None	4.37	NP	155
MXene/TiO_2/Co-0.5%	Two-step calcination-under N_2 (400 °C for 1 h)	30 mg was dispersed in 100 mL of ultrapure water	300 W xenon lamp (UV-vis light)	None	106.7	NP	156
CdS@Ti_3C_2	HTT (200 °C for 5 h)	20 mg photocatalyst dispersed in 100 mL aqueous solution containing 20 vol% methanol	300 W xenon lamp	Methanol	293.06 μmol L^{-1} h^{-1}	7.88	113
Nb_2O_5/C/Nb_2C/g^{-1}-C_3N_4	Calcination under CO_2 (850 °C) and co-sintering (550 °C for 2 hours)	50 mg of photocatalyst in 50 mL of double distilled water with 20 vol% methanol	Visible light (λ > 420 nm)	Methanol	365	NP	157
TiO_2@C g^{-1}-C_3N_4:10%	One-step calcination in air (550 °C for 2 hours)	50 mg of photocatalyst suspended in 100 mL of DD water containing 20 vol% methanol	300 W xenon lamp	Methanol	250.6	0.14 (420 nm)	158
OV-C/TiO_2-600	One-step calcination in air (600 °C for 2 hours)	50 mg of catalyst dispersed in 50 mL of ultrapure water, RT	300 W xenon lamp (200–800 nm)	H_2O Methanol	41 81	0.04 (400 nm)	159
$Ti_3C_2T_x$/TiO_2-400	Calcination in air (400 °C for 15 min)	10 mg of photocatalysts and 20 mL of deionized water, RT	Xenon lamp (320–780 nm), full spectrum (250 mW cm^{-2})	None	422	NP	160
W/$Ti_3C_2T_x$-U	Ball milling	20 mL of ultrapure water, 10 mg of purified photocatalysts, RT	Xenon lamp, full-spectrum (250 mW cm^{-2})	None	227.5	0.05–0.15 in UV-vis and NIR	161
C_3N_4/r-Ti_3C_2 QDs-2	Electrostatical assembling	20 mg photocatalyst and 50 mL of 20 vol% methanol, RT	300 W xenon lamp	Methanol	328.9[b] 197[c]	0.92 (380 nm)	162

[a] NP: value not provided. [b] White light (300–780 nm). [c] Visible light (420–780 nm).

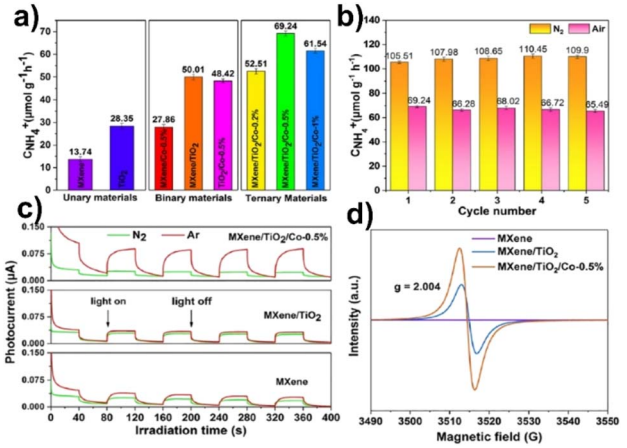

Fig. 12 (a) NH_4^+ production rate in ambient air; (b) the stability of N_2 photofixation activity of MXene/TiO_2/Co-0.5% under N_2 and an air atmosphere; (c) photocurrent spectra of MXene, MXene/TiO_2 and MXene/TiO_2/Co-0.5%; (d) EPR spectra. Reproduced with permission from ref. 163, Copyright 2015 American Chemical Society.

hybrid nanostructure with varied RuO_2 ratios. After 450 minutes of Xe-lamp irradiation, the as-prepared RuO_2@TiO_2-MXene exhibits good N_2 reduction performance, reaching a production rate of 4.37 μmol g^{-1} h^{-1}. The results show that RuO_2@TiO_2-MXene is really a viable material for the NRR. Since TiO_2 creates electrons and holes, MXenes offer efficient electron transport due to metallic conductivity, and RuO_2 presents activation sites, and combining the three components in the hybrid structure has a significant impact on the material's photofixation performance.

In a two-step calcination procedure, Gao *et al.*[156] created MXene/TiO_2/Co composite materials for the NRR. The production rate of MXene/TiO_2/Co-0.5% increased 1.4 times by the addition of Co (50 μmol g^{-1} h^{-1}) compared to that of MXene/TiO_2, and 2.4 times compared with that of TiO_2 (69 μmol g^{-1} h^{-1}). It is significant to note that the ammonia concentration reached 107 μmol g^{-1} h^{-1} under UV-vis light. More than this, the photocatalysts exhibit structural stability throughout the reaction as the XRD diffractograms after five cycles of the NRR show no change at all before and after 10 hours of irradiation. Electron paramagnetic resonance (EPR) spectroscopy was used to examine the reaction mechanism and the results suggested that MXene/TiO_2/Co-0.5% had a higher oxygen vacancy concentration which is beneficial for photocatalytic nitrogen fixation,[163] as shown in Fig. 12.

Sun *et al.*[113] investigated the effects of Ti_3C_2 as a co-catalyst generated by HTT for the NRR, as well as the photocatalytic performance of CdS@Ti_3C_2 composites. Pure CdS NRs (nanorods) had a low rate of photocatalytic NH_4^+ formation (156.62 μmol L^{-1} h^{-1}), while Ti_3C_2 does not produce any ammonia. To create the CdS@Ti_3C_2 composites, several amounts of Ti_3C_2 ranging from 15 to 100 mg, were tested. Of these, in the presence of a scavenger, CdS@Ti_3C_2-15 with 15 mg of MXenes has shown the best NRR activity at a rate of 293.06 μmol L^{-1} h^{-1}, which is 1.9 and 1.4 times higher than that of pure CdS NRs and CdS@Pt, respectively, with an AQY = 7.88%. As a result, Ti_3C_2 MXenes may be able to replace and outperform Pt in terms of enhancing CdS's capacity for the NRR. Photocatalytic nitrogen fixation on a CdS Ti_3C_2-15 composite was conducted in the absence of a sacrificial agent at a nitrogen fixation rate of 27 μmol L^{-1} h^{-1}. The stability test revealed that the production rate is 99.35% of the initial rate after three cycles. Due to their affordability and stability, these composites are expected to play a significant role in the production of ammonia in the future.

Jiang *et al.*[157] reported a 2D MXene-derived Nb_2O_5/C/Nb_2C/g-C_3N_4 heterojunction which was created by uniformly growing Nb_2O_5 on Nb_2C and then forming g-C_3N_4 nanosheets *in situ* on Nb_2O_5/C/Nb_2C. With methanol acting as a scavenger and an optimum Nb_2O_5/C/Nb_2C:g-C_3N_4 ratio of 1 : 1, the heterojunctions exhibited a 9.1 times higher nitrogen reduction rate (365 μmol g^{-1} h^{-1}) in water under visible light, compared with an MXene derived Nb_2O_5/g-C_3N_4 composite. Additionally, a pH adjustment from 3 to 9 would enhance the efficiency of the NRR from 180 to 927 μmol L^{-1} h^{-1} by changing the energy barrier of proton reduction. The improved nitrogen reduction photocatalytic performance may be due to both the Schottky junction produced at the Nb_2O_5/Nb_2C interface as well as the increased electron and hole separation due to the close contact between the conductive Nb_2C and the Nb_2O_5. The NRR efficiency decreased as the pH of the catalytic system is higher than 9, due to extra negative charges created on the photocatalyst surface that prevent the reaction substrate from effectively making contact with the catalytically active site[164] (Fig. 13). Nb_2O_5/C/Nb_2C/g^{-1}-C_3N_4 heterojunctions are stable materials, with no noticeable NH_3 production rate loss observed after 5 cycles.

Through one-step calcination in air of a mixture of Ti_3C_2 and melamine with various ratios of TiO_2@C to g-C_3N_4, Liu *et al.*[158] fabricated a TiO_2@C/g-C_3N_4 heterojunction for the NRR. This approach produces a large number of Ti^{3+} species which act as active sites. The composite material involves the formation of TiO_2 by thermal treatment of Ti_3C_2Tx MXenes, which is further tightly wrapped by *in situ* formed g-C_3N_4 nanosheets. The remarkable performance of the TiO_2@C/g-C_3N_4 heterojunction for photocatalytic nitrogen reduction to ammonia is due to its extensive surface defects, high electron-donating ability, improved light absorption zone, efficient charge transport and reduced recombination, and also strong nitrogen activation ability. The TiO_2@C/g-C_3N_4:10% sample had the highest photocatalytic activity of all the samples, with an ammonia production rate of 250.6 μmol g^{-1} h^{-1}, with an AQE of 0.14% (420 nm) under visible light irradiation. The performance of TiO_2@C/g-C_3N_4:10% is found to be 18 and 10 times higher than that of g-C_3N_4 and TiO@C, respectively. A recycling NH_3 test on TiO_2@C/g-C_3N_4 revealed no detectable decrease in the NH_3 production rate following five cycles in six hours, demonstrating the good stability of the sample.

Using a one-step calcination method at varied temperatures, Qian *et al.*[159] used Ti_3C_2 as a precursor to produce an oxygen vacancy (OV)-rich C/TiO_2 (OV–C/TiO_2) material to convert N_2 into NH_3 under sunlight irradiation. Among the samples, OV-C/TiO_2-600 produced NH_3 at a rate of 41 μmol g^{-1} h^{-1} using water as a proton source (AQY of 0.04% for 400 nm light and 0.01% for

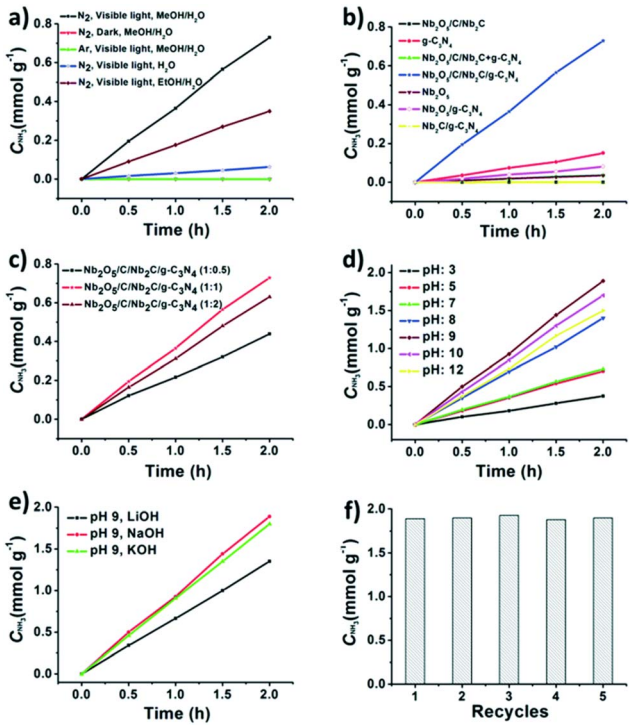

Fig. 13 (a) Control experiments on photocatalytic NH3 production with the MXene-derived Nb_2O_5/C/Nb_2C/g-C_3N_4 heterojunction under different conditions. (b) Photocatalytic activity of the Nb_2O_5/C/Nb_2C, g-C_3N_4, Nb_2O_5/C/Nb_2C + g-C_3N_4, Nb_2O_5/C/Nb_2C/g-C_3N_4, Nb_2O_5, Nb_2O_5/g-C_3N_4 and Nb_2C g^{-1}-C_3N_4 for NH_3 production under visible light irradiation (λ > 420 nm). (b) Photocatalytic NH_3 production activity of Nb_2O_5/C/Nb_2C/g^{-1}-C_3N_4 with the ratio variation of Nb_2O_5/C/Nb_2C: melamine from 0.5 to 1 and 2 during catalyst preparation; (c) photocatalytic NH_3 production activity of Nb_2O_5/C/Nb_2C/g-C_3N_4 with different pH values adjusted by using HCl or NaOH solution. Reproduced with permission from ref. 157, Copyright 2020 The Royal Society of Chemistry.

of 420 nm light, respectively) which is 26.5 times higher than that of TiO_2 Degussa P25. When using methanol as a proton source the NH_3 rate increased to 84 μmol g^{-1} h^{-1}. The addition of oxygen vacancies on the TiO_2 surface and carbon doping increased electron–hole pair formation and decreased electron–hole pair recombination. Moreover, there was an increase in the photocarrier lifetime, as well as chemisorption and activation of N_2 molecules. The NH_3 production yields essentially stayed constant during four photocatalytic cycling trials in 2 h, showing the OV-C/TiO_2-600 sample's good stability.

Hou *et al.*[160] developed plasmonic $Ti_3C_2T_x$ and TiO_2 hybrid structures ($Ti_3C_2T_x$/TiO_2) at various temperatures, with $Ti_3C_2T_x$/TiO_2-400 exhibiting higher activity for the NRR. At room temperature, the $Ti_3C_2T_x$/TiO_2-400 hybrid structure yielded 422 μmol g^{-1} h^{-1} of NH_3 without the use of any sacrificial agents. After being exposed to monochromatic light at 630 nm, $Ti_3C_2T_x$/TiO_2-400 generated 50 μmol g^{-1} h^{-1} of NH_3, with an AQE of 0.05%. Once monochromatic light was changed to 740 nm light, the NH_3 generation rate for $Ti_3C_2T_x$/TiO_2-400 improved to 82 μmol g^{-1} h^{-1}, while the AQE became 0.07%. Additionally, the stability test of $Ti_3C_2T_x$/TiO_2-400 shows that more than 90% of the initial reaction activity was conserved in ten consecutive rounds of reaction, demonstrating the high stability of $Ti_3C_2T_x$/TiO_2-400. The activity of $Ti_3C_2T_x$/TiO_2-400 hybrid structures was attributed to the coexistence of $Ti_3C_2T_x$ and defective TiO_2, which considerably improved charge carrier separation efficiency. The plasmonic $Ti_3C_2T_x$ phase may collect visible and near-infrared light to generate hot electrons that are transported to the TiO_2 conduction band and then trapped by oxygen vacancies.

Under full-spectrum irradiation at room temperature without the use of sacrificial materials, Qi *et al.*[161] demonstrated a remarkable ammonia production rate (227.5 μmol g^{-1} h^{-1}) utilizing $Ti_3C_2T_x$ doped with a W atom. Further research on the catalytic performance was conducted using monochromatic light of various wavelengths. At 630 nm, the production rate was 43.6 μmol g^{-1} h^{-1}, but it dropped to 28 μmol g^{-1} h^{-1} when the light source was centered at 740 nm. In particular, the AQEs of W/$Ti_3C_2T_x$-U were 0.05–0.15% in UV-vis and NIR wavelengths. In addition, W/$Ti_3C_2T_x$-U are stable materials preserving >90% activity after ten subsequent rounds of reaction. Doping with W atoms enhances the physical and chemical adsorption of N_2, and they also serve as the active sites for reducing reaction energy during the NRR.

According to Chang *et al.*,[162] mesoporous hollow g-C_3N_4 spheres were improved with partly reduced Ti_3C_2 quantum dots (r-Ti_3C_2 QDs) on the surface for effective NRR. This resulted in the formation of a C_3N_4/r-Ti_3C_2 QD Schottky junction *via* electrostatic self-assembly. The C_3N_4/r-Ti_3C_2 QDs' nitrogen photofixation activity was better when exposed to white light than it was when exposed to visible light since the photocatalysts had a limited capacity to absorb visible light. The ammonia

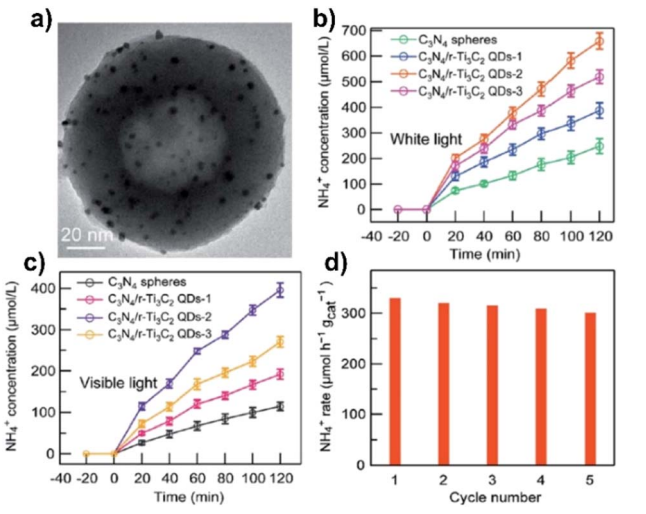

Fig. 14 (a) TEM image of C_3N_4/r-Ti_3C_2 QDs-2; (b and c) N_2 photofixation over the different as-obtained photocatalysts. Time courses of the ammonia concentrations measured under white light illumination (light intensity: 300 mW cm^{-2} and λ = 300–780 nm) and visible light illumination (light intensity: 300 mW cm^{-2} and λ = 420–780 nm); (d) stability tests of C_3N_4/r-Ti_3C_2 QDs-2 for N_2 photofixation under white light. Reproduced with permission from ref. 162, Copyright 2022 The Royal Society of Chemistry.

production rate of C_3N_4/r-Ti_3C_2 QDs reduced from 328.9 μmol g^{-1} h^{-1} to 197 μmol g^{-1} h^{-1} when the light source was switched from white to visible light (Fig. 14), which, under the same circumstances, are 1.6 and 1.9 times as high as that of C_3N_4, respectively. The AQE value of C_3N_4/r-Ti_3C_2 QDs is 0.92% at 380 nm. When C_3N_4 is exposed to light, photoinduced electrons and holes are produced, and r-Ti_3C_2 QDs enable effective migration and separation for these particles. Numerous OV-defect state sites and Ti^{3+} sites found in r-Ti_3C_2 QDs serve as active sites for collecting and activating N_2 molecules. Quickly moving from C_3N_4 to r-Ti_3C_2 QDs *via* the close contact interface, photogenerated electrons from C_3N_4 may next be reduced to NH_3 by trapping and accumulating photoexcited electrons from g-C_3N_4.

4. Metal oxides

4.1. Synthesis and structure evolution

The most facile strategy to tailor the physicochemical properties of MOs is by varying their composition. In binary oxides such as TiO_2, ZnO, Fe_2O_3, *etc.*, a small quantity of an additional metallic component can be introduced into the lattice, while maintaining the overall crystal structure.[165–167] This approach is more straightforward in mixed oxides such as perovskites, brownmillerites, *etc.*, since such materials include more than one metal in their pristine form.

However, more complex compositions with fascinating properties can be made by doping with additional cationic components.[168–171] In all these cases, excellent control of desired properties, including photocatalysis, can be achieved. On the other hand, photocatalytic performance also significantly relies on the nanoscale structural features and morphology of the materials involved. Since fabricating nanostructures depends on synthesis methodology, the choice of the synthesis method is important. The conventional approach for making MOs is the solid-state method where thermal energy drives the formation of the desired phase with a high degree of crystallinity. Here, agglomerated large grains are often produced with lower values of specific surface area. Mechanochemical approaches such as ball milling replaced thermal energy with mechanical energy, with limited extent of applicability and poor control over morphology and nanostructure. It is to be noted that mixed oxide compositions more or less require higher temperatures for the formation of the desired single-phase materials. Also, it is difficult to ensure a homogeneous mixing of the precursors in solid state and mechanochemical methods.[168–171] Therefore, several soft chemical approaches were developed, incorporating a variety of precursors, templates and reaction media by following a number of complexation, precipitation, hydrothermal and templating routes.[172–175] Wet chemical approaches such as the polyol method, sol–gel method, *etc.*, allowed the synthesis of semiconductor photocatalysts with a uniformly distributed particle size and morphology, at comparatively lower temperatures. These methods generally involve the presence of organic molecules such as citric acid, ethylene glycol, *etc.* The interactions between these organic components with their metallic counterparts along with the mechanism of their cross linking and/or decomposition can exert better control on particle size and morphology.[172]

One step synthesis of binary and ternary oxides can be achieved by carrying out the reaction in a sealed reaction vessel above the boiling point of the solvent. This method is designated as the hydrothermal method when water is used as the solvent or the solvothermal method when an organic solvent is used instead.[173,176] A homogeneous solution of the precursor in an appropriate solvent is subjected to thermal treatment at a temperature higher than the boiling point of the solvent. This promotes an increase in pressure inside the reaction chamber. The combined effect of enhanced temperature and autogenous pressure will drive the formation of the desired product. Excellent control of morphology and nanostructure formation is observed in this method. Simple synthesis parameters such as reactant concentration, pH and temperature were found to significantly influence the formation of the desired phase and morphology in most of the cases. Additional control of microstructure and porosity can be achieved by introducing appropriate amounts of organic templates during synthesis. Even though an additional calcination step is not necessary in most of the cases, high temperature treatments are always required to remove the organic structure directing agents and for the structure stabilization of the materials for applications involving enhanced temperatures.[177] To date, a variety of binary and ternary oxide compositions with varied nanostructures and morphologies have been synthesized by following the hydrothermal method.[178–180]

Followed by the successful synthesis of MCM-41 silica with ordered mesopore channels, templating methods are widely used to produce MOs with controlled porosity and textural parameters.[181] The initial focus was on the use of surfactants as soft templates to direct the synthesis of porous oxides.[182] Apart from ordered mesoporous silica and carbon materials, limited success was obtained for the soft template method for oxides.[183–185] This was primarily due to the non-availability of precursors that undergo hydrolysis in a controlled manner with organic templates. Also, organic template removal is generally carried out at high temperatures. Since the crystallization temperature for most of the MO phases was higher than the decomposition temperature of the template, the quality of the resultant materials was compromised. On the other hand, the nanocasting method was also being developed in parallel, for which an inert porous oxide was used as the hard template.[182–187] This method was initially used for the synthesis of ordered mesoporous carbon and was then extended to oxides, utilizing ordered mesoporous silica or carbon as hard templates. A wide variety of binary oxides with extremely high values of surface area and well-ordered pore structure were obtained by this method. Nanocasting was found to be highly versatile and was then used to synthesize complex ternary oxides and non-oxide compositions such as sulfides.[188,189] Unfortunately, this multi-step method was time consuming, costly and non-scalable.

Uniform integration of oxide cocatalysts with semiconductors is necessary to develop highly efficient photocatalysts. Several studies reported single step calcination

treatments under oxidizing or inert atmospheres to combine oxide cocatalysts with photocatalysts including photocatalysts such as TiO_2, g-C_3N_4, *etc.*[190–192] In addition, other approaches including simple impregnation of the cocatalyst species, HTT, photodeposition, *etc.*, are also followed to develop cocatalyst-photocatalyst combinations.[193–195]

4.2. Photocatalytic applications for water splitting

MOs are considered as low cost and easily available cocatalysts for photocatalytic applications including H_2 evolution by splitting water. Fundamentally, the photogenerated electrons from the semiconductor photocatalyst move towards the MO, acting as a cocatalyst, through the interface, resulting in electron–hole separation. Table 4 summarizes several examples of such cocatalyst/photocatalyst systems used in the most recent years for hydrogen production through water splitting. The synthetic approaches to combine different semiconductor photocatalysts and several reaction parameters are also presented.

Thus, Chen *et al.*[196] photodeposited Ni_2O_3 on the surface of hydrothermally synthesized CdS, and H_2 evolution was monitored under visible light irradiation. The presence of Ni_2O_3 resulted in the enhancement of the hydrogen evolution rate up to 41 times that of pure CdS and up to 1.9 times that of Pt loaded CdS. The authors attributed this improvement to the ability of Ni_2O_3 to act as electron traps, thereby promoting charge separation. Stability tests were performed for five cycles and the activity was found to decrease to 86.8% of the initial activity. The authors attributed this to the catalyst loss during filtration and washing.[196] To study the effect of the chemical environment of photodeposition, nickel oxides were loaded onto CdS under neutral as well as alkaline conditions. Interestingly, the materials synthesized under alkaline conditions resulted in a 117 times enhancement of the hydrogen production rate compared to that of pure CdS. It was proposed that the presence of OH^- ions contributed to charge separation by facilitating hole transfer towards the sacrificial agent, methanol.[193]

Lin *et al.*[30] combined 1D $Cd_{1-x}Zn_xS$ nanocrystals with oxygen enriched MoS_2 resulting in $Cd_{1-x}Zn_xS$@O–MoS_2 nanohybrids. NiO_x species were deposited by following an *in situ* photodeposition method. The optimized composition of these nanohybrids exhibited 25 times higher hydrogen evolution rates compared to Pt containing CdZnS. Under visible light

Table 4 Compilation of synthetic and photocatalytic aspects of MO-based materials in hydrogen production through the water splitting reaction[a]

Cocatalyst/photocatalyst	Synthetic method	Hole scavenger	Light region	Optimum H_2 production rate [μmol h^{-1} g^{-1}]	AQY [%]	Ref.
NiO_x/CdS	*In situ* photodeposition	Methanol (30%)	Visible	445.6	NP	196
NiO_x/CdS	*In situ* photodeposition	Methanol (30%)	Visible	590.8	8.6 (400 nm)	193
NiO/$Zn_{0.8}Cd_{0.2}S$	*In situ* photodeposition	None	Visible	783.11	5.86 (350 nm)	197
NiO/TiO_2 nanofibers	Electrospinning and calcination in air (500 °C for 3 h)	Methanol (25%)	Full spectrum	377	1.7 (365 nm)	200
Amorphous NiO/g-C_3N_4	Calcination in air (100–500 °C for 3 h)	TEA (10%)	Visible	68.8	∼0.12 (370 nm)	190
NiO/g-C_3N_4	Impregnation, HTT (125 °C for 10 h) and calcination in air (200–400 °C for 1 h)	None	Visible	1.41	NP	198
NiO/TiO_2	Impregnation and calcination in static air (450 °C for 3 h)	Methanol (5%)	Simulated solar light	∼130	NP	199
NiO/TiO_2	Impregnation and calcination in static air (450 °C for 3 h)	Methanol (5%)	UV	∼70	NP	199
NiO/red phosphorous	Calcination in air (300 °C for 1 h)	Methanol (10%)	Visible	57.27	0.37 (420 nm)	201
Amorphous MoO_x/CdS nanorods	Sonication	Lactic acid (10%)	Simulated solar light	19 300	21.3 (420 nm)	202
Cu_2O/g-C_3N_4	Calcination in air (520 °C for 4 h)	TEA (10%)	Visible	241.3	NP	203
CuO/TiO_2 composite nanofibers	Electrospinning and calcination in air (500 °C for 2 h)	Methanol (10%)	Simulated solar light	1146.9	NP	204
CuO nanodots on TiO_2 nanocrystals	Precipitation using ammonium hydroxide followed by calcination in air (200 °C for 1 h)	Methanol (10%)	UV-visible	∼16 000	NP	191
CuO@NiO core@shell nanoparticles	Chemical reduction (using $N_2H_4.H_2O$) followed by calcination under an inert atmosphere (400 °C for 2 h)	Glycerol (5%)	Solar light	26 100	NP	192
CuO quantum dots/TiO_2 nanosheets	Impregnation followed by calcination in air (300 °C for 2 h)	Methanol (20%)	Full spectrum	18 390	26.93 (313 nm)	205
CoO/g-C_3N_4	Calcination under Ar (400 °C for 4 h)	TEA (10%)	Visible	651.3	NP	206
CoO/C_3N_4 nanotubes	Calcination under vacuum (400 °C for 4 h)	TEA (10%)	Visible	788.6	4.9 (420 nm)	207
Co_3O_4/C_3N_4 nanotubes	Calcination in static air (400 °C for 4 h)	TEA (10%)	Visible	725.7	4.07 (420 nm)	207

[a] ∼ Data taken from a graphical representation of the corresponding reference; NP: value not provided; TEA = triethanolamine.

irradiation using Na_2S/Na_2SO_3 as a sacrificial agent, an AQY of 64.1% was obtained for these materials. Repeated reactions during five cycles indicated minor activity loss. Also, the structure and composition of the recovered material remained unchanged after the photocatalytic reaction.[30]

Liu *et al.*[190] synthesized a series of amorphous NiO modified g-C_3N_4 under different temperature treatments. The heterojunctions formed at the interface between amorphous NiO and g-C_3N_4 created an inner electric field allowing the transfer of photogenerated electrons from C_3N_4 to NiO. Under visible light irradiation, NiO/g-C_3N_4 exhibited 430 times higher hydrogen evolution rates compared to pristine g-C_3N_4 and was consistent during five cycles. Also, the structure and chemical state did not change after the reaction. The authors concluded that the presence of amorphous NiO enhanced the visible light response, promoted the separation and transfer of charge carriers and provided active sites for hydrogen evolution.[190]

Ning *et al.*[197] synthesized a series of $Zn_{1-x}Cd_xS$ and an ultrathin layer of NiO was assembled over it by photodeposition. Under visible light irradiation and in the absence of a sacrificial agent, these materials showed significantly higher photocatalytic activity with an AQY of 0.66% for H_2 evolution, compared to Pt/ZnCdS, as shown in Fig. 15. The NiO layer suppressed the photocorrosion of ZnCdS and the strong electronic coupling between the NiO layer and $Zn_{1-x}Cd_xS$ enabled efficient charge separation and transport.[197]

Fu *et al.*[198] synthesized a series of NiO-g-C_3N_4 by following a successive hydrothermal and calcination procedure. Overall water splitting was achieved for these materials among which the best performance was observed for the materials calcined at 300 °C. In this case, a H_2 evolution rate of 1.41 μmol g^{-1} h^{-1} and an O_2 evolution rate of 0.71 μmol g^{-1} h^{-1} were obtained. Experiments carried out for seven cycles along with characterization performed using the recovered catalyst confirmed the stability of these materials. Photocatalytic efficiency decreased for the materials calcined at higher temperatures. Here also, the presence of NiO aided in visible light absorption, separated the charge carriers and provided active sites.[198] These results are in agreement with the report by Liu *et al.*[190]

Banic *et al.*[199] synthesized a series of NiO/TiO_2 materials with varying mass ratios, by wet impregnation. The photocatalytic water splitting reaction was performed in the presence of methanol under simulated solar irradiation and artificial UV irradiation. The materials with 7 wt% NiO enhanced hydrogen production rates up to 7.6 times compared to that of pure TiO_2 and 112.8 times compared to that of pure NiO. Under optimum conditions, a 1.8 times higher hydrogen production rate was achieved under simulated solar light compared to that under the influence of artificial UV radiation.[199]

Since the preparation method is very important, Li *et al.*[200] synthesized mesoporous NiO/TiO_2 nanofibers by the electrospinning method. The presence of NiO inhibited the crystal growth of TiO_2 resulting in an increase in surface area, pore volume and pore size. Under simulated solar irradiation, an optimum NiO content (0.25 wt%) exhibited a 7 times higher H_2 evolution rate with an AQY of 1.7%, compared to pure TiO_2.[200] Chen *et al.*[201] synthesized a NiO/RP (red phosphorous) composite by HTT followed by high temperature calcination. In this study, the 3 wt% NiO/RP composite exhibited the highest photocatalytic activity for hydrogen production which is 68.56 times higher than that of pure RP under visible light irradiation. The rates did not change significantly for 10 cycles and the physicochemical properties of the recovered materials were in agreement with those of the fresh ones. In the presence of light, electrons are excited towards the conduction band of RP leaving behind holes in the valence band, which simultaneously combines with the electrons from NiO. The holes in NiO are consumed by methanol and photogenerated electrons accumulated on the conduction band of RP which participate in H_2 generation. This material also exhibited H_2 evolution activity in the near IR region.[201]

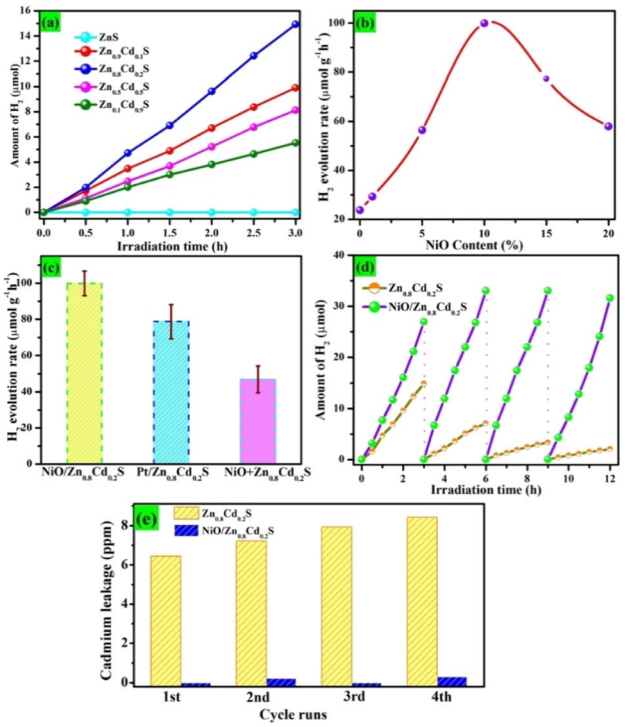

Fig. 15 (a) Photocatalytic H_2 evolution over $Zn_{1-x}Cd_xS$. (b) Rate of H_2 evolution over the x% NiO/$Zn_{0.8}Cd_{0.2}S$ composite samples. (c) A comparison of the H_2 evolution rate over 10% NiO/$Zn_{0.8}Cd_{0.2}S$, 2% Pt/$Zn_{0.8}Cd_{0.2}S$, and NiO + $Zn_{0.8}Cd_{0.2}S$ (simple mechanical mixture of NiO and $Zn_{0.8}Cd_{0.2}S$). (d) Cycling runs for photocatalytic H_2 evolution in pure water with the $Zn_{0.8}Cd_{0.2}S$ and 10 wt% NiO/$Zn_{0.8}Cd_{0.2}S$ composite samples under visible light irradiation. (e) Cd^{2+} leakage profiles under visible light irradiation. Reproduced with permission from ref. 197, Copyright 2019 European Chemical Societies Publishing.

Yan *et al.*[202] prepared nanocomposites consisting of CdS and amorphous MoO_x and studied photocatalytic hydrogen production under visible light irradiation. A 16 times enhancement in hydrogen evolution rates was observed compared to that of pristine CdS. The amounts of hydrogen evolved remained stable for five cycles. The photogenerated electrons from CdS resulted in an *in situ* reduction of Mo^{6+} in amorphous MoO_x creating electronic structure reconstruction in the nanocomposite.[202]

Chen *et al.*[203] synthesized g-C_3N_4 modified with different amounts of Cu_2O nanoparticles by a simple calcination method. In the presence of Cu_2O, up to a 70% increase in visible light induced photocatalytic H_2 evolution was observed. Cu_2O nanoparticles acted as visible light sensitizers, induced sufficient charge separation and exhibited a negative shading effect so that their content above an optimum level reduced the number of active sites. The rate of hydrogen evolution remained stable for five cycles and the chemical state of Cu in the recovered catalyst was the same as that in the fresh one.[203]

Zhu *et al.*[204] reported the use of wheat grain like textured TiO_2/CuO composite nanofibers synthesized by electrospinning for photocatalytic water splitting. CuO incorporation was found to enhance H_2 generation by about 16.8 times in comparison with that of pure TiO_2. Significant loss of photocatalytic performance was not observed for four cycles.[204]

Moon *et al.*[191] reported that size tunable Cu_2O nanodots decorated on the surface of TiO_2 nanocrystals got reduced to Cu under UV irradiation. The resultant metal–semiconductor Schottky junction enhanced the hydrogen production rate significantly in comparison with P25 and reached approximately 50% of the one achieved with Pt/TiO_2 counterparts, as shown in Fig. 16.[191]

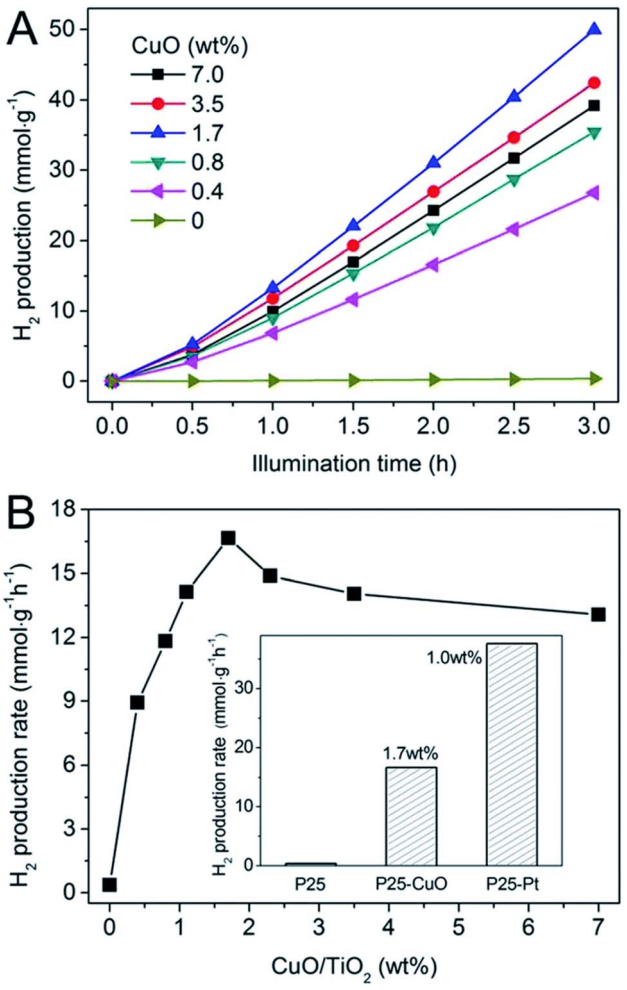

Fig. 16 (A) Hydrogen production *vs.* illumination time in the presence of CuO-decorated TiO_2 catalysts. (B) H_2 production rate *vs.* loading amount of CuO. The inset of (B) is a bar graph showing the activity of CuO-decorated TiO_2 in comparison to that of a Pt-decorated system. Reproduced with permission from ref. 191, Copyright 2014 The Royal Society of Chemistry.

Sadanandam *et al.*[205] hydrothermally synthesized TiO_2 nanosheets with [001] facets exposed and impregnated with CuO quantum dots. It was observed that during the reaction CuO changed to Cu_2O and then to Cu. The energy band alignment of the double heterojunction TiO_2/Cu_2O/Cu provided effective charge separation, increasing the H_2 production efficiency. Under visible light irradiation, the hydrogen production rate of the optimized material was approximately 10 times higher than that of pure TiO_2, with an AQY of 26.93%. Cycling tests were carried out for the optimum catalyst and a H_2 production retention ratio of 96% is obtained after four cycles. The system was then purged with O_2 for 2 h to regenerate the used catalyst. After this, the retention ratio increased to 98%, indicating good cycling stability and photo corrosion resistance.[205] The synergy between CuO and NiO, the most studied oxides as cocatalysts, was verified by Ravi *et al.*[192] who synthesized CuO@NiO core@shell nanoparticles deposited on anatase TiO_2 and studied them for photocatalytic H_2 evolution under direct solar light irradiation. The rate of hydrogen evolution was found to be influenced by the thickness of the NiO shell and cocatalyst loading. 6-fold higher values were obtained in comparison with those of pure TiO_2. The performance of this material was examined for few days. The setup was kept under dark conditions after 4 h solar light illumination and was purged with N_2 gas before the experiments on the next day. The rate of H_2 evolution remained similar for the first 2 days while a minor decrease was noticed on the third day. The authors attributed this to the decrease in the concentration of the sacrificial agent.[192]

Another MO that was studied as a cocatalyst for water splitting is CoO. Mao *et al.*[206] studied the photocatalytic behaviour of g-C_3N_4/CoO nanocomposites with varying amounts of CoO, under visible light irradiation This material with 0.5 wt% CoO content exhibited 3 times superior H_2 evolution rates compared to pure g-C_3N_4, owing to enhanced light absorption and separation of charge carriers. Stable performance was observed during three cycling experiments. Also, the recycled material exhibited no sign of aggregation.[206]

Zhu *et al.*[207] prepared CoO_x confined in g-C_3N_4. The heterojunction formed primarily depended on the conditions of temperature treatment. The type II heterojunction formed between CoO nanoparticles and C_3N_4 nanotubes, under vacuum, exhibited the highest H_2 yield, due to the rapid electron transfer between CoO and C_3N_4. CoO/C_3N_4 NTs were found to exhibit 6% activity loss while for Co_3O_4/C_3N_4 NTs it was almost 18.0%. A slight decrease in the intensity of the main peaks indexed to Co_3O_4 NPs was detected by XRD. This indicates the loss of a portion of anchored Co_3O_4 nanoparticles on C_3N_4 NTs during the recycling process. Also, some extent of agglomeration was observed for this material.[207]

4.3. Photocatalytic applications for CO_2 reduction

For photocatalytic conversion of CO_2, enhancing surface adsorption of CO_2 and suppressing charge carrier recombination represent one of the major focuses. As in the case of water splitting, transition MOs based on Cu, Ni, Co and Fe were most widely investigated as cocatalysts, along with CaO, MgO and In_2O_3 (see Table 5).

Uzunova *et al.*[208] used DFT to deduce the mechanism of CO_2 photoconversion to methanol, using H_2O as the hydrogen source. The presence of MOs results in bending of a CO_2 molecule prior to hydrogenation and the bridging hydroxyl groups which resulted from water dissociation provided H_2. Methanol is formed by following a step-wise mechanism *via* the formation of carboxyl groups, formic acid and formaldehyde intermediates. A comparatively stronger interaction between CO_2 and Cu_2O compared to that between metallic catalysts was reported.[208]

Zhu *et al.*[209] deposited Cu_2O clusters on TiO_2 nanosheets by photodeposition. The authors noticed the formation of surface oxygen vacancies on TiO_2 which was attributed to the presence of Cu_2O. Under simulated solar light irradiation and in the presence of water as the hydrogen source, methane was the only product formed. The presence of 1 wt% Cu_2O resulted in a 30 times enhancement of the photoactivity of pure TiO_2. Cu_2O clusters increased the surface alkalinity and enhanced CO_2 adsorption ability. High concentration of surface oxygen vacancies has also played the role of active sites for CO_2 conversion.[209]

Cu_2O loaded SiC photocatalysts were found to be selective towards methanol under visible light irradiation, using water as the hydrogen source. The CH_3OH yields were comparatively higher than that by the individual components.[210] In agreement with the report by Zhu *et al.*,[209] Cu_2O nanoparticles electrochemically deposited on TiO_2 nanotubes selectively produced CH_4. Under visible light irradiation in the presence of water vapour, an optimum amount of octahedral Cu_2O nanoparticles exhibited high efficiency and selectivity towards methane.

The nanotube structure of TiO_2 provided active sites for the adsorption of reactants and facilitated the transport of photogenerated charge carriers. Synergistically, Cu_2O participated in light absorption and prevented oxidation of the reaction products.[211]

Fang *et al.*[194] synthesized CuO incorporated TiO_2 hollow microspheres with a hollow core and mesoporous shell structure, by a template free one pot HTT, followed by calcination. Photo-reduction of CO_2 was carried out over this material using H_2O as the hydrogen source under UV irradiation, producing CO and CH_4, as shown in Fig. 17. For an optimum CuO loading (3 wt%), 5.8- and 2.7-times higher CO and CH_4 yields, respectively, were obtained compared with those of pristine TiO_2 hollow microspheres, and 7.3- and 9.0-times higher yields were obtained compared to those of commercial TiO_2, respectively. The used catalysts were recovered from the reactor and stored under ambient conditions for 24 h. When this material was tested again, a minimum decrease in product yield was observed indicating regeneration of the catalyst due to desorption of the gas products from its surface during storage.[194]

Gui *et al.*[195] prepared MWCNT@TiO_2 core@shell nanocomposites, impregnated with a series of binary oxides (FeO_x, CuO_x, NiO, CoO_x and ZnO). The efficiency of these materials for CO_2 photoreduction was studied under visible light irradiation in the presence of water vapour. Methane was selectively produced and CuO modified MWCNT@TiO_2 exhibited superior performance among the series. The better performance was attributed to the MO band position with respect to that of TiO_2.[195]

Tahir *et al.*[212] used cordierite honeycomb monoliths loaded with N/TiO_2 and Cu/TiO_2 nanocatalysts using a sol–gel dip coating method for dynamic photocatalytic CO_2 reduction with H_2 selectively to CO under UV-light irradiation. Both Cu and N doping resulted in a shift of band gap energy towards the visible region and also in an efficient transport and trapping of electrons, hindering carrier recombination. The presence of Cu resulted in a 14 times higher CO production than N/TiO_2 and 64 times higher CO production than that of pure TiO_2. Here, the CO production decreased after 4 h of irradiation time, indicating deterioration of photoactivity.[212]

Shoji *et al.*[213] loaded Cu_xO as a reduction cocatalyst and cobalt phosphate (CoPi) as an oxidation cocatalyst on $SrTiO_3$ nanorod thin films. Photocatalytic experiments under UV irradiation were conducted by immersing the film in an aqueous solution bubbled with CO_2. Selective evolution of CO was observed with the highest rate exhibited by the materials with dual cocatalysts. The CO generation rate was found to increase linearly in accordance with the irradiation time. Here, Cu_xO nanoclusters facilitated CO_2 reduction whereas CoPi facilitated surface oxidation to promote oxygen generation. The dual cocatalyst incorporated materials exhibited a 2.5 times superior CO generation rate compared to pure $SrTiO_3$.[213]

Junior *et al.*[214] synthesized layered semiconductor $K_2Ti_4O_9$ by the solid-state method and pillared it with TiO_2. The resultant mesoporous composite was then loaded with Cu_2O nanoparticles as the cocatalyst. CO_2 photoreduction was carried out using water as the hydrogen source under simulated solar light. Improved performance was observed for the pillared material TiO_2/Ti_4O_9 than the pristine layered potassium tetratitanate. Here, electron transfer between the guest TiO_2 and the host $Ti_4O_9^{2-}$ layers could have played a role, along with the presence of additional photoactive sites. Loading of Cu_2O nanoparticles resulted in further improvement of photo activity due to enhanced visible light harvest promoting electron transfer with TiO_2 and $Ti_4O_9^{2-}$. It is to be noted here that since the temperature in the system reached 70 °C during the reaction, the contribution of photothermal effects cannot be ignored.[214]

Jeyalakshmi *et al.*[215] hydrothermally synthesized $Na_{(1-x)}La_x$-$TaO_{(3+x)}$ and Pt, Ag, Au, CuO, NiO and RuO_2 were introduced as cocatalysts by following the wet impregnation method. CO_2 photoconversion was carried out in an alkaline medium under UV-visible light. Methanol and ethanol were produced as the major products along with traces of methane, ethane, ethylene, *etc.* The amounts of methanol produced remained consistent for three cycles over NiO/$Na_{(1-x)}La_xTaO_{(3+x)}$. High AQYs among

Table 5 Compilation of synthetic and photocatalytic aspects of MO-based materials in CO_2 conversion[a]

Cocatalyst/ photocatalyst	Synthetic method	Reactants	Light region	Products [μmol g^{-1} h^{-1}]	AQY [%]	Ref.
Cu_2O/TiO_2 nanosheets	Photodeposition and calcination in air (200 °C, 2 h)	CO_2 and H_2O	Simulated solar light	CH_4 (8.68)	NP	209
Cu_2O/SiC	Precipitation using NaOH followed by chemical reduction using $N_2H_4 \cdot H_2O$	NaOH, Na_2SO_3 and CO_2	Visible	CH_3OH (38)	NP	210
Octahedral Cu_2O/TiO_2 nanotube arrays	Electrochemical deposition	CO_2 and H_2O	Visible	CH_4 (~400 ppm for 4 h)	NP	211
CuO–TiO_2 hollow microspheres	HTT (180 °C for 20 h)	CO_2 and H_2O	UV	CO (14.5) CH_4 (2.1) H_2 (2.8)	1.285 0.747	194
FeOx-MWCNT@TiO_2	Impregnation and calcination under N_2 (400 °C for 2 h)	CO_2 and H_2O	Visible	CH_4 (0.85 μmol g^{-1} for 8 h)	NP	195
CuO-MWCNT@TiO_2	Impregnation and calcination under N_2 (400 °C for 2 h)	CO_2 and H_2O	Visible	CH_4 (0.93 μmol g^{-1} for 8 h)	NP	195
NiO-MWCNT@TiO_2	Impregnation and calcination under N_2 (400 °C for 2 h)	CO_2 and H_2O	Visible	CH_4 (0.44 μmol g^{-1} for 8 h)	NP	195
CoO-MWCNT@TiO_2	Impregnation and calcination under N_2 (400 °C for 2 h)	CO_2 and H_2O	Visible	CH_4 (0.38 μmol g^{-1} for 8 h)	NP	195
ZnO-MWCNT@TiO_2	Impregnation and calcination under N_2 (400 °C for 2 h)	CO_2 and H_2O	Visible	CH_4 (0.27 μmol g^{-1} for 8 h)	NP	195
Cu–TiO_2 in a cordierite honeycomb monolith	Dip coating and calcination in air (500 °C for 5 h)	CO_2 and H_2	Simulated solar light	CO (763) CH_4 (4.20)	0.0826 NP	212
CuxO/CoPi-$SrTiO_3$ nanorod thin films	Impregnation or photoelectrochemical deposition	CO_2 and H_2O	UV	CO (0.4 μmol cm^{-2})	NP	213
Cu_2O on TiO_2-pillared $K_2Ti_4O_9$	Calcination in air (800 °C for 20 h), ion-exchange (using HCl), exfoliation using (TBAOH), impregnation and reflux (160 °C for 2 h)	CO_2 and H_2O	Simulated solar light	CH_3OH (2.93 μmol g^{-1} for 5 h)	NP	214
CuO/$Na_{(1-x)}LaxTaO_{(3+x)}$	Impregnation and calcination in air (300 °C for 2 h)	NaOH, CO_2 and H_2O	UV-visible	CH_3OH (60.5) C_2H_5OH (15.9) C_2H_4O (0.9) C_3H_6 (0.15) C_2H_6 (0.04) C_2H_4 (0.03) CH_4 (0.01) H_2 (0.2)	0.0105	215
NiO/$Na_{(1-x)}LaxTaO_{(3+x)}$	Impregnation and calcination in air (270 °C for 2 h)	NaOH, CO_2 and H_2O	UV-visible	CH_3OH (59.6) C_2H_5OH (18.8) C_2H_4O (2.15) C_3H_6 (0.4) C_2H_6 (0.01) C_2H_4 (0.03) CH_4 (0.02) H_2 (0.2)	0.0112	215
$Co_3O_4/K_2Ti_6O_{13}$	Calcination in air (800 °C for 12 h)	CO_2 and H_2O	Visible	CH_3OH (36.4 μmol g^{-1} for 3 h) HCHO (453.2 μmol g^{-1} for 3 h) CH_4 (1.3 μmol g^{-1} for 3 h) H_2 (8 μmol g^{-1} for 3 h)	NP	216
$NiO/K_2Ti_6O_{13}$	Calcination in air (800 °C for 12 h)	CO_2 and H_2O	Visible	CH_3OH (31.2 μmol g^{-1} for 3 h) HCHO (99.7 μmol g^{-1} for 3 h) CH_4 (1.1 μmol g^{-1} for 3 h) H_2 (201 μmol g^{-1} for 3 h)	NP	216

Table 5 (*Contd.*)

Cocatalyst/ photocatalyst	Synthetic method	Reactants	Light region	Products [μmol g^{-1} h^{-1}]	AQY [%]	Ref.
$CuO/K_2Ti_6O_{13}$	Calcination in air (800 °C for 12 h)	CO_2 and H_2O	Visible	CH_3OH (159.7 μmol g^{-1} for 3 h) HCHO (41.4 μmol g^{-1} for 3 h) CH_4 (0.8 μmol g^{-1} for 3 h) H_2 (282 μmol g^{-1} for 3 h)	NP	216
$Cu–Bi_2O_3/TiO_2$	Calcination under H_2 (550 °C for 5 h)	CO_2 and H_2O	UV-visible	CO (5.74) CH_4 (11.90)	NP	217
$NiO/InTaO_4$	Sol–gel method and calcination in air (1100 °C for 12 h)	NaOH, CO_2 and H_2O	Sunlight	CH_3OH (11.3)	0.063	218
$NiO–InNbO_4$	Incipient wetness impregnation and calcination in air (350 °C for 1 h)	CO_2 and H_2O	Simulated solar light	CH_3OH (1.577)	NP	219
$Co_3O_4–InNbO_4$	Incipient wetness impregnation and calcination in air (350 °C for 1 h)	CO_2 and H_2O	Simulated solar light	CH_3OH (1.503)	NP	219
$NiO–KTaO_3$	HTT (180 °C for 12 h) and calcination in air (600 °C for 1 h)	CO_2 and isopropanol	UV	CH_3OH (1523)	NP	220
$NiO–InVO_4$	Impregnation and calcination in air (350 °C for 2 h)	CO_2, H_2O and $KHCO_3$	Visible	CH_3OH (1.526)	NP	221
$Ni@NiO/InTaO_4–N$	Impregnation, chemical reduction (using NaBH4) and calcination in air (200 °C for 1 h)	CO_2 and H_2O	Visible	CH_3OH (∼300 μmol g^{-1})	NP	222
Macro/microporous MgO modified TiO_2	Biotemplating and calcination in air (500 °C for 3 h)	CO_2 and H_2O	Simulated solar light	CH_4 (1.87)	NP	223
TiO_2/MgO	HTT (200 °C for 12 h)	CO_2, H_2O and NaOH	UV	CO (70.7 μmol g^{-1} L^{-1} for 24 h) CH_4 (34.5 μmol g^{-1} L^{-1} for 24 h) HCOOH (19.5 μmol g^{-1} L^{-1} for 24 h) CH_3COOH (24.9 μmol g^{-1} L^{-1} for 24 h)	NP	224
$Ca/Ti_xSiMCM-41$	HTT (100 °C for 12 h) and calcination (500 °C for 2 h)	CO_2 and H_2O	UV	CH_4 (82 μmol g^{-1} L^{-1} for 8 h)	NP	225

[a] ∼ Data taken from a graphical representation of the corresponding reference; NP: value not provided.

the series were obtained for 0.2 wt% NiO (11.29%) and 1 wt% CuO (10.50%) as cocatalysts. These oxides reduced the band gap energy of $NaTaO_3$ and at the same time the light absorption onset edge was found to be extended to the visible region.[215]

Garay-Rodriguez *et al.*[216] used an ultrasound assisted sol–gel method for synthesizing MO (Co_3O_4, NiO, and CuO) incorporated $K_2Ti_6O_{13}$. Interestingly while some extent of Co^{2+} cations were found to selectively substitute Ti^{4+} cations, Ni^{2+} and Cu^{2+} were incorporated in both Ti^{4+} and K^+ sites. The metal-cation introduction between the tunnels favoured the growth of potassium-poor phases as impurities, especially in the CuO loaded $K_2Ti_6O_{13}$ samples. Photoconversion of CO_2 using H_2O as the hydrogen source under UV-visible light, resulted in different products depending on the loaded MO. It was observed that while the presence of Co_3O_4 favoured the formation of formaldehyde, NiO favoured hydrogen evolution due to additional photo-reforming of the organic compounds and CuO enhanced the selectivity towards methanol and hydrogen. The product yields remained consistent for three consecutive reaction cycles for Co_3O_4, NiO, and CuO incorporated $K_2Ti_6O_{13}$. Moreover, no structural changes were observed by comparing the XRD patterns of the fresh and used catalysts.[216]

Jeong *et al.*[217] explored the use of Bi_2O_3 as a promoter for Cu cocatalysts anchored on the surface of TiO_2 nanoparticles for the photocatalytic conversion of CO_2 to CH_4, under UV-visible light irradiation. The presence of Bi_2O_3 increased the product selectivity towards methane (see Fig. 18). In the absence of Bi_2O_3, the photogenerated electrons reduce the CO_2 adsorbed on the cocatalyst surface to CO, which has a low binding strength and will get detached as the product. Bi_2O_3 provided additional binding sites for CO where it undergoes further transformation, producing CH_4.[217]

Wang *et al.*[218] used a NiO loaded $InTaO_4$ photocatalyst to carry out both aqueous phase and vapor phase photoconversion of CO_2 using visible light. The rate of methanol production was 11.1 μmol g^{-1} h^{-1} which was slightly increased up to 11.30 μmol

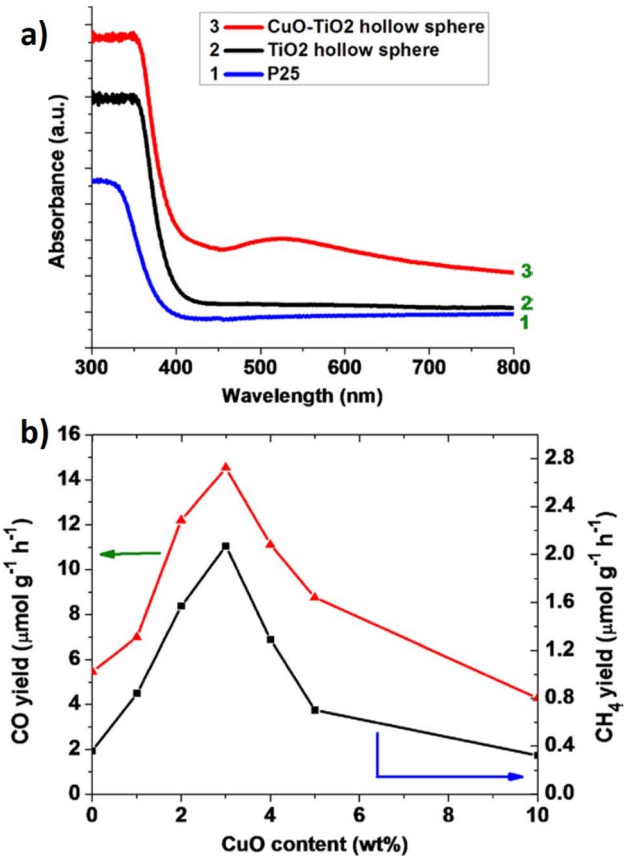

Fig. 17 (a) UV-vis DRS for various TiO_2 based nano-materials. The CuO content in the CuO–TiO_2 catalyst is 3 wt%. (b) Yields of the gas products (CO and CH_4) produced during 24 h of photo-driven CO_2 reduction on the TiO_2 hollow microsphere catalysts with various Cu contents. Reproduced with permission from ref. 194, Copyright 2015 American Chemical Society.

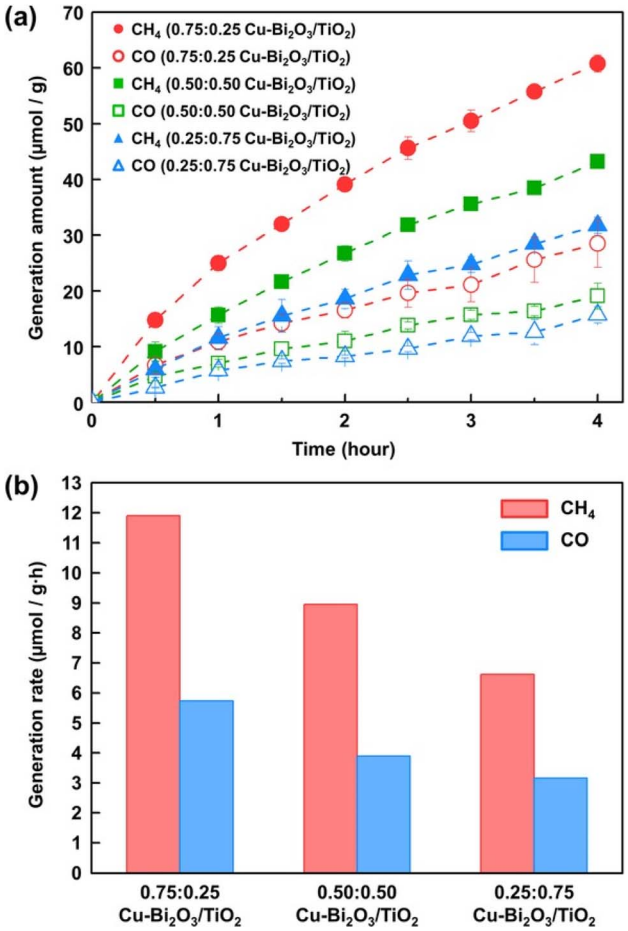

Fig. 18 (a) Amount of CH_4 and CO generated upon using 0.75 : 0.25, 0.50 : 0.50, and 0.25 : 0.75 Cu–Bi_2O_3/TiO_2 photocatalysts. (b) Rates of CH_4 and CO generation in the first 4 h of irradiation. Reproduced with permission from ref. 217, Copyright 2016 European Chemical Societies Publishing.

g^{-1} h^{-1} by utilizing concentrated sunlight. The quantum efficiencies were estimated to be 0.0045% and 0.063% in aqueous-phase and gas phase reactors, respectively.[218]

Lee *et al.*[219] synthesized $InNbO_4$ from the corresponding binary oxides, and cocatalysts (NiO and Co_3O_4) were impregnated by following the incipient-wetness method. NiO–$InNbO_4$ after a reduction–oxidation pre-treatment exhibited the highest activity for producing methanol under visible light which was attributed to the presence of core–shell type Ni^0/NiO on the surface and the presence of a small amount of Nb_2O_5 as a promoter.[219]

Comparative studies were carried out between hydrothermally synthesized perovskite-type and pyrochlore-type powders of potassium tantalate ($KTaO_3$). The pyrochlore form exhibited better photocatalytic activities for producing methanol under UV light irradiation which was further increased by adding NiO as a co-catalyst.[220] Lee *et al.*[221] synthesized $InVO_4$ by the solid-state reaction method using In_2O_3 and V_3O_4 as the starting materials and NiO was added as the cocatalyst by incipient wetness impregnation. The photocatalytic reduction of CO_2 with water was carried out under visible light illumination, producing methanol. Introduction of NiO resulted in lowering of the bandgap due to the formation of sub bands in the valence band by creating additional defect sites on the surface of $InVO_4$, resulting in a higher methanol yield with an AQY of 2.8%.[221]

Tsai *et al.*[222] synthesized N-doped $InTaO_4$ photocatalysts and introduced Ni@NiO core@shell nanostructures as a cocatalyst for transforming CO_2 into methanol. Under visible light irradiation, a 2-fold increment in methanol yield was observed for the N-doped samples which was further increased by the presence of Ni@NiO cocatalysts, compared to that of pristine $InTaO_4$. Due to a narrow band gap, Ni@NiO/$InTaO_4$–N absorbed more light, and the Ni@NiO core@shell structures promoted more efficient electron transport.[222]

Wang *et al.*[223] synthesized porous MgO modified TiO_2 using water convolvulus as the biotemplate. This material photoreduces CO_2 in the presence of water vapour, selectively producing methane. 0.2 wt% MgO resulted in a 3.5 times increase in the CH_4 evolution rate in comparison with pure TiO_2. The authors attributed this to various factors including CO_2 adsorption capacity, charge carrier transport, and enhanced number of active sites, which depend on the amount of added MgO.[223]

Table 6 Compilation of synthetic and photocatalytic aspects of MO-based materials in the NRR

Cocatalyst/photocatalyst	Preparation methods	Reaction conditions	Light source	Sacrificial reagent	NH_3 production[a]	AQY [%]	Ref.
Bi_2MoO_6/OV-BiOBr	HTT (120 °C for 8 h)	30 mg of the photocatalyst in 60 mL of ultrapure water, RT	300 W xenon lamp	None	90.7 μmol g^{-1} h^{-1}	NP	226
30 wt% SV-1T-MoS_2/CdS	HTT (200 °C for 24 h)	20 mg of photocatalyst in 100 mL 20 vol% methanol solution	Simulated solar light	Methanol	8220.83 μmol L^{-1} g^{-1} h^{-1}	4.424	227
18% $Sb_2O_3/W_{18}O_{49}$	Solvothermal (180 °C for 20 h)	5 mg photocatalyst in the aqueous solution (10 mL) containing 20 vol% methanol, RT	300 W xenon lamp	Methanol	35.3 μmol g^{-1} h^{-1}	0.063	228
g-C_3N_4/40 wt% Fe_2O_3	Ternary deep eutectic solvents and calcination (550 °C for 4 h)	10 mg of photocatalyst in 100 mL of distilled water, RT	300 W xenon lamp	Methanol	4380 μmol L^{-1} h^{-1}	NP	229

[a] The production rates were expressed as how they appear in the references.

Torres *et al.*[224] mixed MgO with TiO_2 in different proportions and the resultant nanocomposites were studied in the photoconversion of CO_2. Enhanced selectivity was observed for CO, while CH_4, HCOOH and CH_3COOH were also produced in lower amounts. Addition of 1 wt% of MgO enhanced CH_4 production compared to that with pure TiO_2, however, a further increase in the MgO content significantly deteriorated the performance. The authors attributed this effect to the insulating behaviour of MgO. It is also likely that higher amounts of MgO are blocking the active sites, thereby lowering the light absorption properties.[224]

Jo *et al.*[225] used a series of MCM-41 mesoporous silica modified with Ca and Ti for the photoreduction of CO_2 to CH_4. The optimum material among the series exhibited extremely high yields of methane under solar light irradiation. Optimum Ca doping contributed towards photoreduction by providing additional sites for CO_2 adsorption and by promoting charge carrier separation. It is to be noted that excess metal sites diminish the performance by providing charge recombination centers.[225]

4.4. Photocatalytic applications for N_2 photofixation

In addition to the well-known photocatalytic applications previously mentioned, MOs are also utilized as a cocatalyst in photocatalytic systems for the photoreduction of N_2 to produce NH_3. Cocatalysts as MOs are used to broaden the range of absorbed light, as well as to facilitate the electron transport throughout the system and stop electron–hole recombination. Table 6 summarizes several examples of MO-based photocatalysts used in recent years for the NRR.

For enhanced photocatalytic performance for N_2 conversion to ammonia without any noble metal and sacrificial agents under ambient conditions, Xue *et al.*[226] produced heterojunctions based on n-type Bi_2MoO_6 nanorods and oxygen-vacancy-rich p-type BiOBr nanosheets (Bi_2MoO_6/OV-BiOBr). The average ammonia generation rate of the Bi_2MoO_6/OV-BiOBr heterojunctions is 90.7 μmol g^{-1} h^{-1}, which is about 30 times higher than that of pristine Bi_2MoO_6 nanorods (3.0 μmol g^{-1} h^{-1}) and 3 times higher than that of OV-BiOBr nanosheets (31.2 μmol g^{-1} h^{-1}). This study highlights the significantly increased photocatalytic N_2 fixation activity of the Bi_2MoO_6/OV-BiOBr heterojunctions, without the use of any sacrificial agents.

Sun *et al.*[227] reported sulfur vacancy (SV)-rich O-doped 1T-MoS_2 nanosheets (denoted as SV-1T-MoS_2), prepared by HTT, as cocatalysts to assist in the photocatalytic nitrogen fixation of CdS nanorods, as a hybrid material SV-1T-MoS_2/CdS. Different quantities of the cocatalyst, ranging from 5 to 100 mg, representing 5 to 100 wt%, were used to produce the SV-1T-MoS_2/CdS composites. A remarkable photocatalytic N_2 reduction rate of 8220 μmol L^{-1} h^{-1} g^{-1} is demonstrated by the optimized 30 wt% SV-1T-MoS_2/CdS composites, under simulated solar light irradiation (AM 1.5 G), with methanol as a scavenger, obtaining an AQE of 4.424%. This rate is 2.4 and 4.6 times greater than that of CdSPt (0.1 wt%) and CdS nanorods, respectively, suggesting that SV-1T-MoS_2 may exceed Pt in the CdS's photocatalytic nitrogen fixation performance. However, the rate of NH_4^+ will decrease as the amount of SV-1T-MoS_2 in the composites increased from 30 to 100 wt%. This is probably because excessive MoS_2 prevents the light from being used. Meanwhile, under visible light (780 nm > λ > 420 nm), the photocatalytic nitrogen fixation rate was 3168 μmol L^{-1} h^{-1} g^{-1}.

Three cycles were performed to evaluate the stability over 30 wt% SV-1T-MoS_2/CdS, and after 9 hours of testing, 80% of the incipient activity was still present, demonstrating the materials' good cycle stability.

$Sb_2O_3/W_{18}O_{49}$, a composite made of 2D Sb_2O_3 nanosheets and 1D $W_{18}O_{49}$ nanowires, was created by Hui *et al.*[228] *via* the solvothermal process, by varying the Sb_2O_3 weight, ranging from 1.8 to 70%. The highest NH_3 production was obtained for 18% $Sb_2O_3/W_{18}O_{49}$ with a production rate of 35.3 μmol g^{-1} h^{-1}, with methanol as a scavenger under visible light illumination, which is 3.4 and 5.5 times higher than that of $W_{18}O_{49}$ and

Sb_2O_3, respectively, with an AQE of 0.063%. However, as the Sb_2O_3 concentration was increased above 18 wt%, the rate of NH_3 synthesis decreased. This is probably due to Sb_2O_3 aggregation and the low $Sb_2O_3/W_{18}O_{49}$ interface active regions, which inhibited N_2 adsorption and activation. The heterostructures demonstrated good repeatability with approximately consistent NH_3 production rates. Additionally, cycling studies showed that even after five consecutive cycles, the catalytic activity was mainly the same, with a certain decrease of activity due to aggregation.

Mou *et al.*[229] created g-C_3N_4/MO composites utilizing a simple one-step calcination procedure and a ternary deep eutectic solvent (DES) technique, in which g-C_3N_4/Fe_2O_3 was of interest due to its photocatalytic response. Melamine was added in various amounts to control the loading of α-Fe_2O_3, ranging from 0.1582 g to 2.291 g for the production of 50%-DES, 40%-DES, 35%-DES, and 30%-DES, respectively. At 40 wt%, the best activity was attained (g-C_3N_4/40 wt% Fe_2O_3) with an average rate of 4380 μmol L^{-1} h^{-1} for producing NH_3, with methanol acting as a scavenger. The effective interfacial contact between 2D g-C_3N_4 nanosheets and α-Fe_2O_3 nanoparticles, which improves the transfer and separation efficiency of the charge carriers, may be the reason for the high photocatalytic activity.

5. Comparison between MXenes and metal oxides

MXenes and MOs have gained a lot of interest and have been investigated for photocatalytic applications due to their unique properties, such as electronic band structures, catalytic edge effects, planar morphology, *etc.*[230] This section is dedicated to a comparison as succinct as possible between these two categories of materials when they are used as cocatalysts in photocatalytic reactions. The most important criteria taken into account was the employed synthesis methods, their role in promoting photogenerated charge separation, environmental issues, the cost/benefit ratio, the number of combinations in which they can be used and their photocatalytic stability.

Thus, in terms of synthesis conditions, both categories of materials can be obtained by following relatively simple approaches. While chemical liquid-phase etching of the MAX phase results in the corresponding MXenes, MOs in their amorphous, polycrystalline or single crystal form can be synthesized from their precursors (nitrates, chlorides, *etc.*) under thermal or hydrothermal conditions.[231] In the previous sections, a summary of individual synthesis methods of the two categories of materials is provided. While making a comparison, we need to take into account the fact that MXenes are still in their infancy, whereas MOs have a long history of evolution. A vast majority of photocatalytic studies using MXenes were carried out using $Ti_3C_2T_x$ while for oxides several material options were available. For a fair and realistic assessment, the strategies frequently used to integrate these cocatalysts (MXenes and MOs) with the photocatalysts are to be considered. Thus, the choice of a method relies not only on maintaining the structural, compositional and morphological integrity of the materials employed, but also on establishing a homogeneous and intimate contact between them. In addition, the amount of cocatalyst used is important since an excess can be detrimental for the overall performance.

Broadly, the methods used to develop cocatalyst-photocatalyst composites can be classified into two categories: (i) multi-step synthesis – the components can be synthesized separately and can be combined in desired proportions in a post-synthetic manner; and (ii) "one-pot" approaches – in which the cocatalyst and the photocatalyst are formed simultaneously under the same conditions. As mentioned in the previous sections, post-synthetic approaches are always required for MXenes, since the etching conditions (usually HF) are not compatible with the semiconductor photocatalysts. Also, in cases where the desired phase formation and thermal stabilization of the composites under oxidizing conditions are required, total destruction of MXenes can occur, forming the corresponding MOs. It is to be noted here that a few studies reported controlled oxidation of MXenes (as a precursor) producing cocatalyst-photocatalyst composites. However, it is difficult to control the cocatalyst-photocatalyst ratio in this way and to date, it is not sure whether this approach can be generalized. In our understanding, HTT is the most optimum method that can be adapted to both MXenes and MOs to produce photocatalyst composites. An advantage here for MXenes is their rich surface chemistry that enables them to bind appropriately with the semiconductors. Physical mixing approaches such as grinding are also compatible with both these families of materials; however, it is difficult to establish an intimate contact between the cocatalyst and photocatalyst as required to maintain their synergistic functioning.

In photocatalytic reactions, the main role of cocatalysts is to promote the separation of photogenerated charge carriers by acting either as electron mediators or hole mediators. In this regard, starting from their discovery, due to their excellent electrical conductivity (possessing mostly metallic or semimetallic properties and thus mainly forming Schottky junctions in contact with the semiconductor photocatalysts),[232] MXenes have been mainly promoted as a promising reservoir to trap and shuttle the photogenerated electrons from semiconductors. However, as was demonstrated in many studies, the MXene's role of electron- or hole-mediator depends very much on the type of surface functional groups[37,102,233–236] and/or the work function compatibility between the MXene and the semiconductor forming the composites.[237] This latter situation is also applicable in the case of photocatalytic composites with MOs as cocatalysts. Consequently, across the interfaces between the components of the composite photocatalysts, photogenerated holes will flow from the high-work-function component (the semiconductor acting as a photocatalyst) to the low-work-function component (the MO acting as a cocatalyst), while the photogenerated electrons will follow the opposite direction. In other words, the MO cocatalyst, which is actually a semiconductor material, might work either as an electron mediator or a hole mediator depending on the type of junction it makes with the semiconductor photocatalyst (*e.g.*, p-type/n-type, n-type/n-type junction or even *Z* or *S* scheme). To

summarize, in terms of the type of junction formed within the composite photocatalyst, the main difference between the MXenes and the MOs is given by their intrinsic properties. MXenes generally possessing a metallic character form Schottky junctions with the semiconductor photocatalyst depending on the terminal functional groups (*e.g.*, –OH, –O, and –F). On the other hand, MOs generally form either p-type/n-type or n-type/n-type junctions as they have semiconductor properties.

Regarding the environmental concerns associated with the use of MXenes or MOs as cocatalysts that might arise, it should be noted that MXene synthesis is much more harmful to the environment than that of the MOs, mainly due to the use of the HF etchant. However, the use of proper handling and disposal measures can minimize the potential hazards, as well as the use of alternative synthetic methods that are currently being developed.

We will reach the same conclusion if we compare the production costs (the production costs for MXenes are comparatively higher, considering the synthesis of parent MAX phases), but perhaps the fairest cost-benefit comparison would be to follow the gain resulting from their use in the three types of reactions discussed in this review.

Regarding the photocatalytic water splitting reaction, multiple reactions occur on the surface of the composite photocatalyst as represented in eqn (9)–(11):

$$H_2O + e^- \rightarrow H^* + OH^- \quad (9)$$

$$H_2O + H^* + e^- \rightarrow H_2 + OH^- \quad (10)$$

$$H^* + H^* + 2e^- \rightarrow H_2 \quad (11)$$

As shown, in the first step (eqn (9)), an intermediate adsorbed H* is formed and then, in the second step, the H_2 is desorbed by two possible ways: the reaction between the adsorbed H* and a H^+ (eqn (10)) or through the combination of two H* (eqn (11)). In the evaluation of photoactivity of a composite, the Gibbs free energy of the adsorbed hydrogen (ΔG_{H^*}) is regarded as a crucial parameter, and in an ideal situation its value should be close to zero. A large negative or positive ΔG_{H^*} indicates too strong or too weak chemical adsorption of H*, meaning a harder or easier desorption of the H_2 molecule as the reaction product, respectively. In this view, it has to be specified that MXenes show in general $|\Delta G_{H^*}|$ values closer to zero than the MOs. Thus, for example, the O-terminated Ti_3C_2 shows a near-zero $|\Delta G_{H^*}|$ value (0.00283 eV),[111] which is even lower than the values of noble metal platinum (0.09 eV),[238,239] MoS_2 (0.08 eV)[240] and WS_2 (0.22 eV),[240] which are among the most active cocatalysts for the water splitting reaction, while TiO_2 shows ΔG_{H^*} values of 2.37 eV and 2.32 eV for the (101) and (001) exposed facets,[241] respectively. Actually, this could be an explanation for the very good photoactivity observed for the MXene-based composites.

In the case of both photocatalytic CO_2 reduction and N_2 photofixation reactions, the common step is the activation of the reactants (*i.e.*, CO_2 and N_2). As both reactants are acid molecules (with CO_2 possessing much higher acidity than N_2), the presence of basic sites, such as the hydroxyl groups, is a prerequisite to perform the activation of these molecules. In view of that, in the case of MXenes, surface alkalinisation is needed in order to create more surface hydroxyl groups as active sites[131] to adsorb and activate both CO_2 and N_2 molecules. This post-synthetic procedure is not necessary in the case of MOs, which already possess large amounts of such hydroxyl groups on the surface.

To summarize, in terms of the best activities reached so far, studies on water splitting indicate that a combination of MXenes ($Ti_3C_2T_x$) with black phosphorous and g-C_3N_4 exhibited the best performance for hydrogen evolution. Also, superior performances were observed for MXenes combined with CdS. In addition, TEA and lactic acid were reported to be the most appropriate hole scavengers under visible light irradiation. In the case of MOs, the highest H_2 production rates were observed for CuO as the cocatalyst in the presence of methanol or glycerol as hole scavengers. It is clear from the literature data that extremely high values for AQY were obtained when MXenes were used as cocatalysts. On the other hand, for photocatalytic CO_2 conversion, selectivity is a major parameter to consider. Using MXenes as the cocatalyst, CO and CH_4 were found to be the main products in most of the cases. Even though a few studies reported the formation of methanol, the product window was narrow. Instead, as a general trend, MOs were found to be more selective for hydrocarbons (other than CH_4) and oxygenated products like methanol. There are no big differences in the photocatalytic activity when MOs or MXenes are used as the cocatalyst for N_2 photofixation, because the product formation and selectivity are related to the cocatalyst-photocatalyst composite, rather than the individual components.

Regarding the number of possible combinations, by comparing Tables 1–3 with Tables 4–6 one can observe that in the case of MXenes there are limited combinations used, mainly Ti-based MXenes, while for the MOs many more possibilities were explored.

As the last comparison criterion, the durability of the composites based on MXenes and metal oxides represents an important aspect that has to be considered for practical applications. Thus, it has to be specified that leaving a photocatalyst for a longer period of time under the harsh conditions imposed by the photocatalytic reactions will finally lead to photocorrosion phenomena.[242] In this view, in comparison with the MOs, one of the biggest advantages of using MXenes as cocatalysts is to improve the photostability of the composites that contain it by shuttling photogenerated carriers from the unwanted side reaction with semiconductors.[243,244]

To conclude, regardless of the comparison criteria used here, both categories of materials present advantages that should further guide research in the field of photocatalysis towards finding the most efficient cocatalyst/photocatalyst combinations (see Fig. 19).

6. Summary and future perspectives

This review underlined how important is to optimize the amount and type of the cocatalyst, and its choice should be

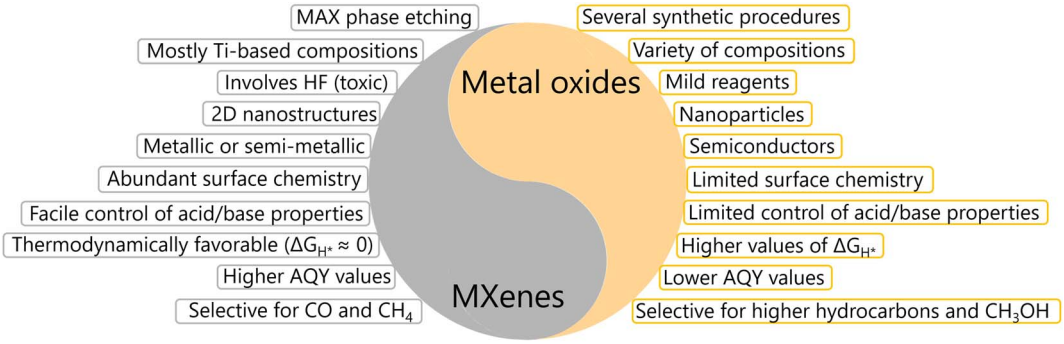

Fig. 19 Scheme summarising the advantages and disadvantages of MXenes and metal oxides to be used as cocatalysts in photocatalytic reactions.

carefully addressed and controlled. Moreover, the electronic properties, composition, loading, and morphology, among other factors, play an important role, affecting the overall photocatalytic activity of the hybrid materials. The literature survey presented in this review demonstrated that the use of MXenes and MOs as cocatalysts could greatly improve the photoactivity of a photocatalyst. This is mainly due to their capacity to promote the separation of photogenerated charge carriers. Overall, the photocatalytic processes presented in this review appear to be very attractive; however, there are challenges, such as activity and stability or high cost, that need to be elucidated.

Since the photocatalytic process takes place on the surface of the photocatalysts, the screening of the surface and electronic properties of the photocatalytic composites should be more systematic. This is mandatory especially in the case of MXenes as their surface is terminated with different functional groups, the type of which not only depending on the etching procedure but also altering under reaction conditions, thus changing the photocatalytic behaviour of the MXene-based composites. In this view, a single characterization approach (which in most cases is carried out before performing the photocatalytic reaction) is insufficient to support a comprehensive understanding of the surface properties of MXenes and thus, a combination of complementary characterization techniques is required.

With regard to the stability issues of the currently used photocatalytic systems, it should be underlined that the effects of the reaction environment on the composite's surface demand more research attention. On this subject, as compared with MOs, MXenes have not been as extensively investigated as cocatalysts in photocatalytic processes. As already mentioned, MXenes are unstable in aqueous environments and in the presence of O_2 and UV irradiation, because under such conditions MXenes are transformed into their corresponding oxides.[45] However, as shown within this review in subSections 3.3.1 and 3.4.1, this can result in a positive approach for obtaining materials with properties of both type of materials, carbides and oxides, paving the way for new materials for photocatalysis. Moreover, there are studies that confirm the role of carbon in facilitating the separation of charge carriers and the use of MXenes as a precursor for photocatalysts.[105,158,159] To sum up, in regard to the stability of MXenes and MOs acting as cocatalysts, probing approaches at the molecular level, such as different *in situ/operando* spectroscopies, are required in order to investigate the reaction mechanisms happening on the surface of these composites under specific chemical environment and photocatalytic conditions. Nevertheless, additional theoretical and rigorous experimental studies will be helpful for the development of the next generation of both MXene- and MO-based composites with target applications in the area of photocatalysis.

Last but not least, with the focus on the abundant tunability of MXene chemical compositions, but unfortunately with a high production cost, the majority of the photocatalytic studies are still concentrating on the use of Ti-based MXenes and less studies focus on the synthesis of other MXene materials. Therefore, utilization of other MXene-based composites requires further attention in both theoretical and experimental aspects.

To finish, although MXene and MO cocatalysts are a promising and attractive alternative to replace expensive noble-metal cocatalysts in the targeted photocatalytic applications presented here, significant research efforts are still needed. Following the literature displayed in this review, it is clear that there is room for improvement especially in the design and synthesis of MXene-based composites, and in this regard, several approaches can be envisaged, such as developing more environment-friendly methods for the existing ones and extending the preparation protocols to other MXenes besides Ti-based ones.

Author contributions

M. N. and A. I. contributed to Sections 1–4, while F. N., M. F. and S. N. contributed to Sections 5 and 6, all with scientific writing, illustrations and table drafting. M. F. and S. N. supervised the research work and contributed to funding acquisition, outline drafting, reviewing, and editing the overall text, illustrations and tables of the manuscript.

Conflicts of interest

There are no conflicts to declare.

Acknowledgements

This work was supported by grants of the Ministry of Research, Innovation and Digitization, CNCS – UEFISCDI, project number PN–III–P4-PCE-2021-1461 and PN–III–P4-ID-ERC-2021-0007, all within PNCDI III. Financial support from Romanian Ministry of Research, Innovation and Digitization through the Core Program 2023–2026 (contract PC3-PN23080303) is gratefully acknowledged.

References

1 N. S. Lewis, *Science*, 2016, **351**, aad1920.
2 R. Schäppi, D. Rutz, F. Dähler, A. Muroyama, P. Haueter, J. Lilliestam, A. Patt, P. Furler and A. Steinfeld, *Nature*, 2022, **601**, 63–68.
3 Q. Wang, C. Pornrungroj, S. Linley and E. Reisner, *Nat. Energy*, 2022, **7**, 13–24.
4 R. Wang, T. Huang, J. Xue, J. Tong, K. Zhu and Y. Yang, *Nat. Photonics*, 2021, **15**, 411–425.
5 I. Massiot, A. Cattoni and S. Collin, *Nat. Energy*, 2020, **5**, 959–972.
6 Y. Tachibana, L. Vayssieres and J. R. Durrant, *Nat. Photonics*, 2012, **6**, 511–518.
7 J. H. Montoya, L. C. Seitz, P. Chakthranont, A. Vojvodic, T. F. Jaramillo and J. K. Nørskov, *Nat. Mater.*, 2017, **16**, 70–81.
8 B. Qiu, M. Du, Y. Ma, Q. Zhu, M. Xing and J. Zhang, *Energy Environ. Sci.*, 2021, **14**, 5260–5288.
9 Z. Wang, Y. Hu, S. Zhang and Y. Sun, *Chem. Soc. Rev.*, 2022, **51**, 6704–6737.
10 G. Chen, G. I. N. Waterhouse, R. Shi, J. Zhao, Z. Li, L. Wu, C. Tung and T. Zhang, *Angew. Chem., Int. Ed.*, 2019, **58**, 17528–17551.
11 D. G. Nocera, *Acc. Chem. Res.*, 2012, **45**, 767–776.
12 R. M. Navarro Yerga, M. C. Álvarez Galván, F. del Valle, J. A. Villoria de la Mano and J. L. G. Fierro, *ChemSusChem*, 2009, **2**, 471–485.
13 A. Kubacka, M. Fernández-García and G. Colón, *Chem. Rev.*, 2012, **112**, 1555–1614.
14 X. Sun, S. Jiang, H. Huang, H. Li, B. Jia and T. Ma, *Angew. Chem., Int. Ed.*, 2022, **61**, e2022048.
15 X. Li, J. Yu and M. Jaroniec, *Chem. Soc. Rev.*, 2016, **45**, 2603–2636.
16 Z. Wang, C. Li and K. Domen, *Chem. Soc. Rev.*, 2019, **48**, 2109–2125.
17 L. Jing, W. Zhou, G. Tian and H. Fu, *Chem. Soc. Rev.*, 2013, **42**, 9509.
18 M. Ahmed and G. Xinxin, *Inorg. Chem. Front.*, 2016, **3**, 578–590.
19 M. Z. Rahman, M. G. Kibria and C. B. Mullins, *Chem. Soc. Rev.*, 2020, **49**, 1887–1931.
20 J. Yoon, J. Kim, C. Kim, H. W. Jang and J. Lee, *Adv. Energy Mater.*, 2021, **11**, 2003052.
21 Q. Xiang, B. Cheng and J. Yu, *Angew. Chem., Int. Ed.*, 2015, **54**, 11350–11366.
22 S. Bai, W. Yin, L. Wang, Z. Li and Y. Xiong, *RSC Adv.*, 2016, **6**, 57446–57463.
23 J. Ran, M. Jaroniec and S. Qiao, *Adv. Mater.*, 2018, **30**, 1704649.
24 G. Zhao and X. Xu, *Nanoscale*, 2021, **13**, 10649–10667.
25 H. Zhao, L. Jian, M. Gong, M. Jing, H. Li, Q. Mao, T. Lu, Y. Guo, R. Ji, W. Chi, Y. Dong and Y. Zhu, *Small Struct.*, 2022, **3**, 2100229.
26 D. Wang and X.-Q. Gong, *Nat. Commun.*, 2021, **12**, 158.
27 R. Reichert, Z. Jusys and R. J. Behm, *J. Phys. Chem. C*, 2015, **119**, 24750–24759.
28 X. Wang, Y. Ruan, S. Feng, S. Chen and K. Su, *ACS Sustainable Chem. Eng.*, 2018, **6**, 11424–11432.
29 S. Bai, L. Yang, C. Wang, Y. Lin, J. Lu, J. Jiang and Y. Xiong, *Angew. Chem., Int. Ed.*, 2015, **54**, 14810–14814.
30 H. Lin, B. Sun, H. Wang, Q. Ruan, Y. Geng, Y. Li, J. Wu, W. Wang, J. Liu and X. Wang, *Small*, 2019, **15**, 1804115.
31 T. Simon, N. Bouchonville, M. J. Berr, A. Vaneski, A. Adrović, D. Volbers, R. Wyrwich, M. Döblinger, A. S. Susha, A. L. Rogach, F. Jäckel, J. K. Stolarczyk and J. Feldmann, *Nat. Mater.*, 2014, **13**, 1013–1018.
32 G. Ge, M. Liu, C. Liu, W. Zhou, D. Wang, L. Liu and J. Ye, *J. Mater. Chem. A*, 2019, **7**, 9222–9229.
33 Z. Sun, H. Zheng, J. Li and P. Du, *Energy Environ. Sci.*, 2015, **8**, 2668–2676.
34 R. Tang, S. Xiong, D. Gong, Y. Deng, Y. Wang, L. Su, C. Ding, L. Yang and C. Liao, *ACS Appl. Mater. Interfaces*, 2020, **12**, 56663–56680.
35 L. Cheng, X. Li, H. Zhang and Q. Xiang, *J. Phys. Chem. Lett.*, 2019, **10**, 3488–3494.
36 Y. Zhao, M. Que, J. Chen and C. Yang, *J. Mater. Chem. C*, 2020, **8**, 16258–16281.
37 X. Xie and N. Zhang, *Adv. Funct. Mater.*, 2020, **30**, 2002528.
38 K. Huang, C. Li, H. Li, G. Ren, L. Wang, W. Wang and X. Meng, *ACS Appl. Nano Mater.*, 2020, **3**, 9581–9603.
39 X. Li, Y. Bai, X. Shi, N. Su, G. Nie, R. Zhang, H. Nie and L. Ye, *Mater. Adv.*, 2021, **2**, 1570–1594.
40 M. Naguib, M. W. Barsoum and Y. Gogotsi, *Adv. Mater.*, 2021, **33**, 2103393.
41 K. R. G. Lim, M. Shekhirev, B. C. Wyatt, B. Anasori, Y. Gogotsi and Z. W. Seh, *Nat. Synth.*, 2022, **1**, 601–614.
42 Á. Morales-García, F. Calle-Vallejo and F. Illas, *ACS Catal.*, 2020, **10**, 13487–13503.
43 R. Wang, M. Li, K. Sun, Y. Zhang, J. Li and W. Bao, *Small*, 2022, **18**, 2201740.
44 F. Bu, M. M. Zagho, Y. Ibrahim, B. Ma, A. Elzatahry and D. Zhao, *Nano Today*, 2020, **30**, 100803.
45 I. M. Chirica, A. G. Mirea, Ş. Neaţu, M. Florea, M. W. Barsoum and F. Neaţu, *J. Mater. Chem. A*, 2021, **9**, 19589–19612.
46 Y. Zhao, S. Zhang, R. Shi, G. I. N. Waterhouse, J. Tang and T. Zhang, *Mater. Today*, 2020, **34**, 78–91.
47 X. Meng, N. Yun and Z. Zhang, *Can. J. Chem. Eng.*, 2019, **97**, 1982–1998.
48 A. K. Singh, K. Mathew, H. L. Zhuang and R. G. Hennig, *J. Phys. Chem. Lett.*, 2015, **6**, 1087–1098.
49 X. Zhou and H. Dong, *ChemCatChem*, 2019, **11**, 3688–3715.

50 P. Liao and E. A. Carter, *Chem. Soc. Rev.*, 2013, **42**, 2401–2422.
51 C. Zhang, G. Chen, Y. Si and M. Liu, *Phys. Chem. Chem. Phys.*, 2022, **24**, 1237–1261.
52 Y. Dong, P. Duchesne, A. Mohan, K. K. Ghuman, P. Kant, L. Hurtado, U. Ulmer, J. Y. Y. Loh, A. A. Tountas, L. Wang, A. Jelle, M. Xia, R. Dittmeyer and G. A. Ozin, *Chem. Soc. Rev.*, 2020, **49**, 5648–5663.
53 H. Tong, S. Ouyang, Y. Bi, N. Umezawa, M. Oshikiri and J. Ye, *Adv. Mater.*, 2012, **24**, 229–251.
54 M. Humayun, C. Wang and W. Luo, *Small Methods*, 2022, **6**, 2101395.
55 D. M. Alonso, S. G. Wettstein and J. A. Dumesic, *Chem. Soc. Rev.*, 2012, **41**, 8075–8098.
56 R. Huang, X. Li, W. Gao, X. Zhang, S. Liang and M. Luo, *RSC Adv.*, 2021, **11**, 14844–14861.
57 L. Luo, T. Zhang, M. Wang, R. Yun and X. Xiang, *ChemSusChem*, 2020, **13**, 5173–5184.
58 C. C. Nguyen, N. N. Vu and T.-O. Do, *J. Mater. Chem. A*, 2015, **3**, 18345–18359.
59 M. Xiao, Z. Wang, M. Lyu, B. Luo, S. Wang, G. Liu, H. Cheng and L. Wang, *Adv. Mater.*, 2019, **31**, 1801369.
60 D. Chen, X. Zhang and A. F. Lee, *J. Mater. Chem. A*, 2015, **3**, 14487–14516.
61 H. Li, Z. Bian, J. Zhu, D. Zhang, G. Li, Y. Huo, H. Li and Y. Lu, *J. Am. Chem. Soc.*, 2007, **129**, 8406–8407.
62 X. Wang, M. Liao, Y. Zhong, J. Y. Zheng, W. Tian, T. Zhai, C. Zhi, Y. Ma, J. Yao, Y. Bando and D. Golberg, *Adv. Mater.*, 2012, **24**, 3421–3425.
63 T. Xiong, F. Dong and Z. Wu, *RSC Adv.*, 2014, **4**, 56307–56312.
64 G. Prieto, H. Tüysüz, N. Duyckaerts, J. Knossalla, G.-H. Wang and F. Schüth, *Chem. Rev.*, 2016, **116**, 14056–14119.
65 F. E. Osterloh, *Chem. Soc. Rev.*, 2013, **42**, 2294–2320.
66 M. Naguib, M. Kurtoglu, V. Presser, J. Lu, J. Niu, M. Heon, L. Hultman, Y. Gogotsi and M. W. Barsoum, *Adv. Mater.*, 2011, **23**, 4248–4253.
67 A. VahidMohammadi, J. Rosen and Y. Gogotsi, *Science*, 2021, **372**, eabf1581.
68 G. Deysher, C. E. Shuck, K. Hantanasirisakul, N. C. Frey, A. C. Foucher, K. Maleski, A. Sarycheva, V. B. Shenoy, E. A. Stach, B. Anasori and Y. Gogotsi, *ACS Nano*, 2020, **14**, 204–217.
69 O. Mashtalir, M. Naguib, V. N. Mochalin, Y. Dall'Agnese, M. Heon, M. W. Barsoum and Y. Gogotsi, *Nat. Commun.*, 2013, **4**, 1716.
70 M. Naguib, R. R. Unocic, B. L. Armstrong and J. Nanda, *Dalton Trans.*, 2015, **44**, 9353–9358.
71 M. Ghidiu, M. R. Lukatskaya, M.-Q. Zhao, Y. Gogotsi and M. W. Barsoum, *Nature*, 2014, **516**, 78–81.
72 J. Halim, M. R. Lukatskaya, K. M. Cook, J. Lu, C. R. Smith, L.-Å. Näslund, S. J. May, L. Hultman, Y. Gogotsi, P. Eklund and M. W. Barsoum, *Chem. Mater.*, 2014, **26**, 2374–2381.
73 W. Sun, S. A. Shah, Y. Chen, Z. Tan, H. Gao, T. Habib, M. Radovic and M. J. Green, *J. Mater. Chem. A*, 2017, **5**, 21663–21668.
74 T. Li, L. Yao, Q. Liu, J. Gu, R. Luo, J. Li, X. Yan, W. Wang, P. Liu, B. Chen, W. Zhang, W. Abbas, R. Naz and D. Zhang, *Angew. Chem., Int. Ed.*, 2018, **57**, 6115–6119.
75 H. Shi, P. Zhang, Z. Liu, S. W. Park, M. R. Lohe, Y. Wu, A. Shaygan Nia, S. Yang and X. Feng, *Angew. Chem., Int. Ed.*, 2021, **60**, 8689–8693.
76 Y. Li, H. Shao, Z. Lin, J. Lu, L. Liu, B. Duployer, P. O. Å. Persson, P. Eklund, L. Hultman, M. Li, K. Chen, X.-H. Zha, S. Du, P. Rozier, Z. Chai, E. Raymundo-Piñero, P.-L. Taberna, P. Simon and Q. Huang, *Nat. Mater.*, 2020, **19**, 894–899.
77 M. Li, J. Lu, K. Luo, Y. Li, K. Chang, K. Chen, J. Zhou, J. Rosen, L. Hultman, P. Eklund, P. O. Å. Persson, S. Du, Z. Chai, Z. Huang and Q. Huang, *J. Am. Chem. Soc.*, 2019, **141**, 4730–4737.
78 B. Anasori, Y. Xie, M. Beidaghi, J. Lu, B. C. Hosler, L. Hultman, P. R. C. Kent, Y. Gogotsi and M. W. Barsoum, *ACS Nano*, 2015, **9**, 9507–9516.
79 Q. Tao, M. Dahlqvist, J. Lu, S. Kota, R. Meshkian, J. Halim, J. Palisaitis, L. Hultman, M. W. Barsoum, P. O. Å. Persson and J. Rosen, *Nat. Commun.*, 2017, **8**, 14949.
80 L. Dong, H. Kumar, B. Anasori, Y. Gogotsi and V. B. Shenoy, *J. Phys. Chem. Lett.*, 2017, **8**, 422–428.
81 N. M. Caffrey, *J. Phys. Chem. C*, 2020, **124**, 18797–18804.
82 J. Halim, A. S. Etman, A. Elsukova, P. Polcik, J. Palisaitis, M. W. Barsoum, P. O. Å. Persson and J. Rosen, *Nanoscale*, 2021, **13**, 311–319.
83 R. Meshkian, H. Lind, J. Halim, A. El Ghazaly, J. Thörnberg, Q. Tao, M. Dahlqvist, J. Palisaitis, P. O. Å. Persson and J. Rosen, *ACS Appl. Nano Mater.*, 2019, **2**, 6209–6219.
84 M. Zhao, X. Xie, C. E. Ren, T. Makaryan, B. Anasori, G. Wang and Y. Gogotsi, *Adv. Mater.*, 2017, **29**, 1702410.
85 C. E. Ren, M. Zhao, T. Makaryan, J. Halim, M. Boota, S. Kota, B. Anasori, M. W. Barsoum and Y. Gogotsi, *ChemElectroChem*, 2016, **3**, 689–693.
86 M. R. Lukatskaya, S. Kota, Z. Lin, M.-Q. Zhao, N. Shpigel, M. D. Levi, J. Halim, P.-L. Taberna, M. W. Barsoum, P. Simon and Y. Gogotsi, *Nat. Energy*, 2017, **2**, 17105.
87 L. Xiu, Z. Wang, M. Yu, X. Wu and J. Qiu, *ACS Nano*, 2018, **12**, 8017–8028.
88 Y. Xia, T. S. Mathis, M.-Q. Zhao, B. Anasori, A. Dang, Z. Zhou, H. Cho, Y. Gogotsi and S. Yang, *Nature*, 2018, **557**, 409–412.
89 X. Xie, K. Kretschmer, B. Anasori, B. Sun, G. Wang and Y. Gogotsi, *ACS Appl. Nano Mater.*, 2018, **1**, 505–511.
90 Q. Zhao, Q. Zhu, J. Miao, P. Zhang, P. Wan, L. He and B. Xu, *Small*, 2019, **15**, 1904293.
91 Q. Xue, H. Zhang, M. Zhu, Z. Pei, H. Li, Z. Wang, Y. Huang, Y. Huang, Q. Deng, J. Zhou, S. Du, Q. Huang and C. Zhi, *Adv. Mater.*, 2017, **29**, 1604847.
92 Q. Zhang, Y. Sun, M. Liu and Y. Liu, *Nanoscale*, 2020, **12**, 1826–1832.
93 B. Shao, Z. Liu, G. Zeng, H. Wang, Q. Liang, Q. He, M. Cheng, C. Zhou, L. Jiang and B. Song, *J. Mater. Chem. A*, 2020, **8**, 7508–7535.

94 H. Mao, C. Gu, S. Yan, Q. Xin, S. Cheng, P. Tan, X. Wang, F. Xiu, X. Liu, J. Liu, W. Huang and L. Sun, *Adv. Electron. Mater.*, 2020, **6**, 1900493.
95 T. Su, R. Peng, Z. D. Hood, M. Naguib, I. N. Ivanov, J. K. Keum, Z. Qin, Z. Guo and Z. Wu, *ChemSusChem*, 2018, **11**, 688–699.
96 Y. Li, D. Zhang, X. Feng, Y. Liao, Q. Wen and Q. Xiang, *Nanoscale Adv.*, 2019, **1**, 1812–1818.
97 H. Wang, R. Peng, Z. D. Hood, M. Naguib, S. P. Adhikari and Z. Wu, *ChemSusChem*, 2016, **9**, 1490–1497.
98 T. Su, Z. D. Hood, M. Naguib, L. Bai, S. Luo, C. M. Rouleau, I. N. Ivanov, H. Ji, Z. Qin and Z. Wu, *ACS Appl. Energy Mater.*, 2019, **2**, 4640–4651.
99 T. Su, Z. D. Hood, M. Naguib, L. Bai, S. Luo, C. M. Rouleau, I. N. Ivanov, H. Ji, Z. Qin and Z. Wu, *Nanoscale*, 2019, **11**, 8138–8149.
100 K. Maeda, H. Wakayama, Y. Washio, A. Ishikawa, M. Okazaki, H. Nakata and S. Matsuishi, *J. Phys. Chem. C*, 2020, **124**, 14640–14645.
101 Z. Guo, J. Zhou, L. Zhu and Z. Sun, *J. Mater. Chem. A*, 2016, **4**, 11446–11452.
102 X. Zhang, X. Zhao, D. Wu, Y. Jing and Z. Zhou, *Nanoscale*, 2015, **7**, 16020–16025.
103 G. Gao, A. P. O'Mullane and A. Du, *ACS Catal.*, 2017, **7**, 494–500.
104 K. Xiong, P. Wang, G. Yang, Z. Liu, H. Zhang, S. Jin and X. Xu, *Sci. Rep.*, 2017, **7**, 15095.
105 G. Jia, Y. Wang, X. Cui and W. Zheng, *ACS Sustainable Chem. Eng.*, 2018, **6**, 13480–13486.
106 A. Fujishima and K. Honda, *Nature*, 1972, **238**, 37–38.
107 T. Inoue, A. Fujishima, S. Konishi and K. Honda, *Nature*, 1979, **277**, 637–638.
108 Y. Li, X. Deng, J. Tian, Z. Liang and H. Cui, *Appl. Mater. Today*, 2018, **13**, 217–227.
109 C. Peng, X. Xie, W. Xu, T. Zhou, P. Wei, J. Jia, K. Zhang, Y. Cao, H. Wang, F. Peng, R. Yang, X. Yan, H. Pan and H. Yu, *Chem. Eng. J.*, 2021, **421**, 128766.
110 B. Wang, M. Wang, F. Liu, Q. Zhang, S. Yao, X. Liu and F. Huang, *Angew. Chem., Int. Ed.*, 2020, **59**, 1914–1918.
111 J. Ran, G. Gao, F.-T. Li, T.-Y. Ma, A. Du and S.-Z. Qiao, *Nat. Commun.*, 2017, **8**, 13907.
112 R. Xiao, C. Zhao, Z. Zou, Z. Chen, L. Tian, H. Xu, H. Tang, Q. Liu, Z. Lin and X. Yang, *Appl. Catal., B*, 2020, **268**, 118382.
113 B. Sun, P. Qiu, Z. Liang, Y. Xue, X. Zhang, L. Yang, H. Cui and J. Tian, *Chem. Eng. J.*, 2021, **406**, 127177.
114 M. Ding, R. Xiao, C. Zhao, D. Bukhvalov, Z. Chen, H. Xu, H. Tang, J. Xu and X. Yang, *Sol. RRL*, 2021, **5**, 2000414.
115 N. Zhao, Y. Hu, J. Du, G. Liu, B. Dong, Y. Yang, J. Peng, J. Li and M. Zhai, *Appl. Surf. Sci.*, 2020, **530**, 147247.
116 S. Jin, Z. Shi, H. Jing, L. Wang, Q. Hu, D. Chen, N. Li and A. Zhou, *ACS Appl. Energy Mater.*, 2021, **4**, 12754–12766.
117 G. Zuo, Y. Wang, W. L. Teo, A. Xie, Y. Guo, Y. Dai, W. Zhou, D. Jana, Q. Xian, W. Dong and Y. Zhao, *Angew. Chem., Int. Ed.*, 2020, **59**, 11287–11292.
118 X. Du, T. Zhao, Z. Xiu, Z. Xing, Z. Li, K. Pan, S. Yang and W. Zhou, *Appl. Mater. Today*, 2020, **20**, 100719.
119 K. Huang, C. Li and X. Meng, *J. Colloid Interface Sci.*, 2020, **580**, 669–680.
120 R. Chen, P. Wang, J. Chen, C. Wang and Y. Ao, *Appl. Surf. Sci.*, 2019, **473**, 11–19.
121 Y. Li, L. Ding, Z. Liang, Y. Xue, H. Cui and J. Tian, *Chem. Eng. J.*, 2020, **383**, 123178.
122 Z. Li, W. Huang, J. Liu, K. Lv and Q. Li, *ACS Catal.*, 2021, **11**, 8510–8520.
123 Y. Li, L. Ding, Y. Guo, Z. Liang, H. Cui and J. Tian, *ACS Appl. Mater. Interfaces*, 2019, **11**, 41440–41447.
124 J. Kang, S. Byun, S. Kim, J. Lee, M. Jung, H. Hwang, T. W. Kim, S. H. Song and D. Lee, *ACS Appl. Energy Mater.*, 2020, **3**, 9226–9233.
125 J. Li, L. Zhao, S. Wang, J. Li, G. Wang and J. Wang, *Appl. Surf. Sci.*, 2020, **515**, 145922.
126 T. Song, L. Hou, B. Long, A. Ali and G. J. Deng, *J. Colloid Interface Sci.*, 2021, **584**, 474–483.
127 Y. Li, X. Chen, Y. Sun, X. Meng, Y. Dall'Agnese, G. Chen, C. Dall'Agnese, H. Ren, S. Sasaki, H. Tamiaki and X. Wang, *Adv. Mater. Interfaces*, 2020, **7**, 1902080.
128 Y. Li, Y. Sun, T. Zheng, Y. Dall'Agnese, C. Dall'Agnese, X. Meng, S. Sasaki, H. Tamiaki and X. Wang, *Chem. – Eur. J.*, 2021, **27**, 5277–5282.
129 S. Debow, T. Zhang, X. Liu, F. Song, Y. Qian, J. Han, K. Maleski, Z. B. Zander, W. R. Creasy, D. L. Kuhn, Y. Gogotsi, B. G. DeLacy and Y. Rao, *J. Phys. Chem. C*, 2021, **125**, 10473–10482.
130 J. Low, L. Zhang, T. Tong, B. Shen and J. Yu, *J. Catal.*, 2018, **361**, 255–266.
131 M. Ye, X. Wang, E. Liu, J. Ye and D. Wang, *ChemSusChem*, 2018, **11**, 1606–1611.
132 Q. Song, B. Shen, J. Yu and S. Cao, *ChemNanoMat*, 2021, **7**, 910–915.
133 Q. Tang, P. Xiong, H. Wang and Z. Wu, *J. Colloid Interface Sci.*, 2022, **619**, 179–187.
134 K. Wang, X. Li, N. Wang, Q. Shen, M. Liu, J. Zhou and N. Li, *Ind. Eng. Chem. Res.*, 2021, **60**, 8720–8732.
135 Z. Zeng, Y. Yan, J. Chen, P. Zan, Q. Tian and P. Chen, *Adv. Funct. Mater.*, 2019, **29**, 1806500.
136 J. Zhang, J. Shi, S. Tao, L. Wu and J. Lu, *Appl. Surf. Sci.*, 2021, **542**, 148685.
137 S. Cao, B. Shen, T. Tong, J. Fu and J. Yu, *Adv. Funct. Mater.*, 2018, **28**, 1800136.
138 J. Li, Z. Wang, H. Chen, Q. Zhang, H. Hu, L. Liu, J. Ye and D. Wang, *Catal. Sci. Technol.*, 2021, **11**, 4953–4961.
139 C. Yang, Q. Tan, Q. Li, J. Zhou, J. Fan, B. Li, J. Sun and K. Lv, *Appl. Catal., B*, 2020, **268**, 118738.
140 F. He, B. Zhu, B. Cheng, J. Yu, W. Ho and W. Macyk, *Appl. Catal., B*, 2020, **272**, 119006.
141 Q. Tang, Z. Sun, S. Deng, H. Wang and Z. Wu, *J. Colloid Interface Sci.*, 2020, **564**, 406–417.
142 H. Wang, Q. Tang and Z. Wu, *ACS Sustainable Chem. Eng.*, 2021, **9**, 8425–8434.
143 L. Hong, R. Guo, Y. Yuan, X. Ji, Z. Lin, X. Yin and W. Pan, *Colloids Surf., A*, 2022, **639**, 128358.
144 W. Chen, B. Han, Y. Xie, S. Liang, H. Deng and Z. Lin, *Chem. Eng. J.*, 2020, **391**, 123519.

145 Q. Shi, X. Zhang, Y. Yang, J. Huang, X. Fu, T. Wang, X. Liu, A. Sun, J. Ge, J. Shen, Y. Zhou and Z. Liu, *J. Energy Chem.*, 2021, **59**, 9–18.
146 M. Que, Y. Zhao, Y. Yang, L. Pan, W. Lei, W. Cai, H. Yuan, J. Chen and G. Zhu, *ACS Appl. Mater. Interfaces*, 2021, **13**, 6180–6187.
147 M. Que, W. Cai, Y. Zhao, Y. Yang, B. Zhang, S. Yun, J. Chen and G. Zhu, *J. Colloid Interface Sci.*, 2022, **610**, 538–545.
148 Z. Zhang, B. Wang, H.-B. Zhao, J.-F. Liao, Z.-C. Zhou, T. Liu, B. He, Q. Wei, S. Chen, H.-Y. Chen, D.-B. Kuang, Y. Li and G. Xing, *Appl. Catal., B*, 2022, **312**, 121358.
149 H. Liu, *Chin. J. Catal.*, 2014, **35**, 1619–1640.
150 S. D. Minteer, P. Christopher and S. Linic, *ACS Energy Lett.*, 2019, **4**, 163–166.
151 A. Liu, Y. Yang, X. Ren, Q. Zhao, M. Gao, W. Guan, F. Meng, L. Gao, Q. Yang, T. Ma and X. Liang, *ChemSusChem*, 2020, **13**, 3766–3788.
152 J. A. Pool, E. Lobkovsky and P. J. Chirik, *Nature*, 2004, **427**, 527–530.
153 J. Qin, X. Hu, X. Li, Z. Yin, B. Liu and K. Lam, *Nano Energy*, 2019, **61**, 27–35.
154 B. Chang, Y. Guo, D. Wu, L. Li, B. Yang and J. Wang, *Chem. Sci.*, 2021, **12**, 11213–11224.
155 C. Hao, Y. Liao, Y. Wu, Y. An, J. Lin, Z. Gu, M. Jiang, S. Hu and X. Wang, *J. Phys. Chem. Solids*, 2020, **136**, 109141.
156 W. Gao, X. Li, S. Luo, Z. Luo, X. Zhang, R. Huang and M. Luo, *J. Colloid Interface Sci.*, 2021, **585**, 20–29.
157 H. Jiang, C. Zang, Y. Zhang, W. Wang, C. Yang, B. Sun, Y. Shen and F. Bian, *Catal. Sci. Technol.*, 2020, **10**, 5964–5972.
158 Q. Liu, L. Ai and J. Jiang, *J. Mater. Chem. A*, 2018, **6**, 4102–4110.
159 J. Qian, S. Zhao, W. Dang, Y. Liao, W. Zhang, H. Wang, L. Lv, L. Luo, H.-Y. Jiang and J. Tang, *Adv. Sustainable Syst.*, 2021, **5**, 2000282.
160 T. Hou, Q. Li, Y. Zhang, W. Zhu, K. Yu, S. Wang, Q. Xu, S. Liang and L. Wang, *Appl. Catal., B*, 2020, **273**, 119072.
161 L. I. Qi, J. Xu, S. Wang, K. Yu, W. Zhu, T. Hou, L. Zhang, W. Zhang, S. Liang and L. Wang, *Trans. Nonferrous Met. Soc. China*, 2022, **32**, 233–250.
162 B. Chang, Y. Guo, H. Liu, L. Li and B. Yang, *J. Mater. Chem. A*, 2022, **10**, 3134–3145.
163 H. Li, J. Shang, Z. Ai and L. Zhang, *J. Am. Chem. Soc.*, 2015, **137**, 6393–6399.
164 W. Song, E. M. Lopato, S. Bernhard, P. A. Salvador and G. S. Rohrer, *Appl. Catal., B*, 2020, **269**, 118750.
165 S. Martha, P. Chandra Sahoo and K. M. Parida, *RSC Adv.*, 2015, **5**, 61535–61553.
166 Y. Sun, T. Zhang, C. Li, K. Xu and Y. Li, *J. Mater. Chem. A*, 2020, **8**, 13415–13436.
167 Y. Yang, S. Niu, D. Han, T. Liu, G. Wang and Y. Li, *Adv. Energy Mater.*, 2017, **7**, 1700555.
168 X. Li, H. Zhao, J. Liang, Y. Luo, G. Chen, X. Shi, S. Lu, S. Gao, J. Hu, Q. Liu and X. Sun, *J. Mater. Chem. A*, 2021, **9**, 6650–6670.
169 Z. Zeng, Y. Xu, Z. Zhang, Z. Gao, M. Luo, Z. Yin, C. Zhang, J. Xu, B. Huang, F. Luo, Y. Du and C. Yan, *Chem. Soc. Rev.*, 2020, **49**, 1109–1143.
170 M. A. Peña and J. L. G. Fierro, *Chem. Rev.*, 2001, **101**, 1981–2018.
171 S. Royer, D. Duprez, F. Can, X. Courtois, C. Batiot-Dupeyrat, S. Laassiri and H. Alamdari, *Chem. Rev.*, 2014, **114**, 10292–10368.
172 A. E. Danks, S. R. Hall and Z. Schnepp, *Mater. Horiz.*, 2016, **3**, 91–112.
173 D. R. Modeshia and R. I. Walton, *Chem. Soc. Rev.*, 2010, **39**, 4303.
174 X. Huang, G. Zhao, G. Wang and J. T. S. Irvine, *Chem. Sci.*, 2018, **9**, 3623–3637.
175 Y. Jun, J. Choi and J. Cheon, *Angew. Chem., Int. Ed.*, 2006, **45**, 3414–3439.
176 Y. Mao, T.-J. Park, F. Zhang, H. Zhou and S. S. Wong, *Small*, 2007, **3**, 1122–1139.
177 M.-M. Titirici, M. Antonietti and A. Thomas, *Chem. Mater.*, 2006, **18**, 3808–3812.
178 A. Querejeta, A. Varela, M. Parras, F. del Monte, M. García-Hernández and J. M. González-Calbet, *Chem. Mater.*, 2009, **21**, 1898–1905.
179 S. Bie, Y. Zhu, J. Su, C. Jin, S. Liu, R. Yang and J. Wu, *J. Mater. Chem. A*, 2015, **3**, 22448–22453.
180 J. J. Urban, L. Ouyang, M.-H. Jo, D. S. Wang and H. Park, *Nano Lett.*, 2004, **4**, 1547–1550.
181 C. T. Kresge, M. E. Leonowicz, W. J. Roth, J. C. Vartuli and J. S. Beck, *Nature*, 1992, **359**, 710–712.
182 D. Gu and F. Schüth, *Chem. Soc. Rev.*, 2014, **43**, 313–344.
183 H. Yang and D. Zhao, *J. Mater. Chem.*, 2005, **15**, 1217–1231.
184 A.-H. Lu and F. Schüth, *Adv. Mater.*, 2006, **18**, 1793–1805.
185 F. Schüth, *Angew. Chem., Int. Ed.*, 2003, **42**, 3604–3622.
186 M. M. Nair, H. Yen and F. Kleitz, *C. R. Chim.*, 2014, **17**, 641–655.
187 M. M. Nair, S. Kaliaguine and F. Kleitz, *ACS Catal.*, 2014, **4**, 3837–3846.
188 Y. Shi, Y. Wan and D. Zhao, *Chem. Soc. Rev.*, 2011, **40**, 3854.
189 B. T. Yonemoto, G. S. Hutchings and F. Jiao, *J. Am. Chem. Soc.*, 2014, **136**, 8895–8898.
190 J. Liu, Q. Jia, J. Long, X. Wang, Z. Gao and Q. Gu, *Appl. Catal., B*, 2018, **222**, 35–43.
191 G. D. Moon, J. B. Joo, I. Lee and Y. Yin, *Nanoscale*, 2014, **6**, 12002–12008.
192 P. Ravi, V. Navakoteswara Rao, M. V. Shankar and M. Sathish, *Int. J. Hydrogen Energy*, 2020, **45**, 7517–7529.
193 X. Chen, W. Chen, H. Gao, Y. Yang and W. Shangguan, *Appl. Catal., B*, 2014, **152–153**, 68–72.
194 B. Fang, Y. Xing, A. Bonakdarpour, S. Zhang and D. P. Wilkinson, *ACS Sustainable Chem. Eng.*, 2015, **3**, 2381–2388.
195 M. M. Gui, S.-P. Chai and A. R. Mohamed, *Appl. Surf. Sci.*, 2014, **319**, 37–43.
196 X. Chen, W. Chen, P. Lin, Y. Yang, H. Gao, J. Yuan and W. Shangguan, *Catal. Commun.*, 2013, **36**, 104–108.
197 X. Ning, W. Zhen, X. Zhang and G. Lu, *ChemSusChem*, 2019, **12**, 1410–1420.

198 Y. Fu, C. Liu, C. Zhu, H. Wang, Y. Dou, W. Shi, M. Shao, H. Huang, Y. Liu and Z. Kang, *Inorg. Chem. Front.*, 2018, **5**, 1646–1652.
199 N. Banic, J. Krstić, S. Stojadinović, A. Brnović, A. Djordjevic and B. Abramović, *Int. J. Energy Res.*, 2020, **44**, 8951–8963.
200 L. Li, B. Cheng, Y. Wang and J. Yu, *J. Colloid Interface Sci.*, 2015, **449**, 115–121.
201 N. Chen, J. Cao, M. Guo, C. Liu, H. Lin and S. Chen, *Int. J. Hydrogen Energy*, 2021, **46**, 19363–19372.
202 B. Yan, J. Li, Z. Lin, C. Du and G. Yang, *ACS Appl. Nano Mater.*, 2019, **2**, 6783–6792.
203 J. Chen, S. Shen, P. Guo, M. Wang, P. Wu, X. Wang and L. Guo, *Appl. Catal., B*, 2014, **152–153**, 335–341.
204 L. Zhu, M. Hong and G. W. Ho, *Nano Energy*, 2015, **11**, 28–37.
205 G. Sadanandam, X. Luo, X. Chen, Y. Bao, K. P. Homewood and Y. Gao, *Appl. Surf. Sci.*, 2021, **541**, 148687.
206 Z. Mao, J. Chen, Y. Yang, D. Wang, L. Bie and B. D. Fahlman, *ACS Appl. Mater. Interfaces*, 2017, **9**, 12427–12435.
207 Y. Zhu, T. Wan, X. Wen, D. Chu and Y. Jiang, *Appl. Catal., B*, 2019, **244**, 814–822.
208 E. L. Uzunova, N. Seriani and H. Mikosch, *Phys. Chem. Chem. Phys.*, 2015, **17**, 11088–11094.
209 S. Zhu, S. Liang, Y. Tong, X. An, J. Long, X. Fu and X. Wang, *Phys. Chem. Chem. Phys.*, 2015, **17**, 9761–9770.
210 H. Li, Y. Lei, Y. Huang, Y. Fang, Y. Xu, L. Zhu and X. Li, *J. Nat. Gas Chem.*, 2011, **20**, 145–150.
211 Y. Li, W. Zhang, X. Shen, P. Peng, L. Xiong and Y. Yu, *Chin. J. Catal.*, 2015, **36**, 2229–2236.
212 M. Tahir and B. Tahir, *Appl. Surf. Sci.*, 2016, **377**, 244–252.
213 S. Shoji, A. Yamaguchi, E. Sakai and M. Miyauchi, *ACS Appl. Mater. Interfaces*, 2017, **9**, 20613–20619.
214 M. Alves Melo Júnior, A. Morais and A. F. Nogueira, *Microporous Mesoporous Mater.*, 2016, **234**, 1–11.
215 V. Jeyalakshmi, R. Mahalakshmy, K. R. Krishnamurthy and B. Viswanathan, *Catal. Today*, 2016, **266**, 160–167.
216 L. F. Garay-Rodríguez and L. M. Torres-Martínez, *J. Mater. Sci.: Mater. Electron.*, 2020, **31**, 19248–19265.
217 S. Jeong, W. D. Kim, S. Lee, K. Lee, S. Lee, D. Lee and D. C. Lee, *ChemCatChem*, 2016, **8**, 1641–1645.
218 Z.-Y. Wang, H.-C. Chou, J. C. S. Wu, D. P. Tsai and G. Mul, *Appl. Catal., A*, 2010, **380**, 172–177.
219 D.-S. Lee, H.-J. Chen and Y.-W. Chen, *J. Phys. Chem. Solids*, 2012, **73**, 661–669.
220 X. Shao, X. Yin and J. Wang, *J. Colloid Interface Sci.*, 2018, **512**, 466–473.
221 D.-S. Lee and Y.-W. Chen, *J. CO2 Util.*, 2015, **10**, 1–6.
222 C.-W. Tsai, H. M. Chen, R.-S. Liu, K. Asakura and T.-S. Chan, *J. Phys. Chem. C*, 2011, **115**, 10180–10186.
223 F. Wang, Y. Zhou, P. Li, L. Kuai and Z. Zou, *Chin. J. Catal.*, 2016, **37**, 863–868.
224 J. A. Torres, A. E. Nogueira, G. T. S. T. da Silva, O. F. Lopes, Y. Wang, T. He and C. Ribeiro, *J. CO2 Util.*, 2020, **35**, 106–114.
225 S. W. Jo, B. S. Kwak, K. M. Kim, J. Y. Do, N.-K. Park, S. O. Ryu, H.-J. Ryu, J.-I. Baek and M. Kang, *Appl. Surf. Sci.*, 2015, **355**, 891–901.
226 X. Xue, R. Chen, C. Yan, Y. Hu, W. Zhang, S. Yang, L. Ma, G. Zhu and Z. Jin, *Nanoscale*, 2019, **11**, 10439–10445.
227 B. Sun, Z. Liang, Y. Qian, X. Xu, Y. Han and J. Tian, *ACS Appl. Mater. Interfaces*, 2020, **12**, 7257–7269.
228 X. Hui, L. Li, Q. Xia, S. Hong, L. Hao, A. W. Robertson and Z. Sun, *Chem. Eng. J.*, 2022, **438**, 135485.
229 H. Mou, J. Wang, D. Zhang, D. Yu, W. Chen, D. Wang and T. Mu, *J. Mater. Chem. A*, 2019, **7**, 5719–5725.
230 L. Yan, Q. Zhang, W. Deng, Q. Zhang and Y. Wang, *Catalytic Valorization of Biomass and Bioplatforms to Chemicals through Deoxygenation*, Elsevier Inc., 1st edn, 2020, vol. 66.
231 H. H. B. T.-S, in *Transition Metal Oxides*,ed. S. S. and C. Kung, Elsevier, 1989, vol. 45, pp. 121–135.
232 M. Naguib, M. Kurtoglu, V. Presser, J. Lu, J. Niu, M. Heon, L. Hultman, Y. Gogotsi and M. W. Barsoum, *Adv. Mater.*, 2011, **23**, 4248.
233 M. Khazaei, M. Arai, T. Sasaki, A. Ranjbar, Y. Liang and S. Yunoki, *Phys. Rev. B: Condens. Matter Mater. Phys.*, 2015, **92**, 75411.
234 C. Peng, X. Yang, Y. Li, H. Yu, H. Wang and F. Peng, *ACS Appl. Mater. Interfaces*, 2016, **8**, 6051–6060.
235 C. Peng, H. Wang, H. Yu and F. Peng, *Mater. Res. Bull.*, 2017, **89**, 16–25.
236 Y. Liu, H. Xiao and W. A. Goddard, *J. Am. Chem. Soc.*, 2016, **138**, 15853–15856.
237 C. Peng, P. Wei, X. Li, Y. Liu, Y. Cao, H. Wang, H. Yu, F. Peng, L. Zhang, B. Zhang and K. Lv, *Nano Energy*, 2018, **53**, 97–107.
238 J. K. Nørskov, T. Bligaard, J. Rossmeisl and C. H. Christensen, *Nat. Chem.*, 2009, **1**, 37–46.
239 B. Hinnemann, P. G. Moses, J. Bonde, K. P. Jørgensen, J. H. Nielsen, S. Horch, I. Chorkendorff and J. K. Nørskov, *J. Am. Chem. Soc.*, 2005, **127**, 5308–5309.
240 J. Bonde, P. G. Moses, T. F. Jaramillo, J. K. Nørskov and I. Chorkendorff, *Faraday Discuss.*, 2009, **140**, 219–231.
241 Y. H. Li, C. Peng, S. Yang, H. F. Wang and H. G. Yang, *J. Catal.*, 2015, **330**, 120–128.
242 B. Weng, M.-Y. Qi, C. Han, Z.-R. Tang and Y.-J. Xu, *ACS Catal.*, 2019, **9**, 4642–4687.
243 T. Cai, L. Wang, Y. Liu, S. Zhang, W. Dong, H. Chen, X. Yi, J. Yuan, X. Xia, C. Liu and S. Luo, *Appl. Catal., B*, 2018, **239**, 545–554.
244 X. Xie, N. Zhang, Z.-R. Tang, M. Anpo and Y.-J. Xu, *Appl. Catal., B*, 2018, **237**, 43–49.

